

The Pennsylvania State University

The Graduate School

**GROWTH AND TEM INVESTIGATION OF TWO DIMENSIONAL TRANSITION
METAL DICHALCOGENIDES AND THEIR HETEROSTRUCTURES**

A Thesis in

Materials Science and Engineering

by

Fu Zhang

© 2017 Fu Zhang

Submitted in Partial Fulfillment
of the Requirements
for the Degree of

Master of Science

August 2017

The thesis of Fu Zhang was reviewed and approved* by the following:

Nasim Alem
Assistant Professor of Materials Science and Engineering
Thesis Advisor

Joan A. Redwing
Professor of Materials Science and Engineering

Mauricio Terrones
Professor of Physics, Chemistry and Materials Science & Engineering

Suzanne Mohny
Professor of Materials Science and Engineering and Electrical Engineering
Chair of Graduate Program

*Signatures are on file in the Graduate School

ABSTRACT

In this thesis, a systematic study on the synthesis, transfer and TEM characterization of 2D TMDs is done to provide an understanding for growth approaches aiming to obtain high quality TMDs film and defect-engineering, which can greatly facilitate the exploration of fundamental phenomena and novel applications in these fascinating 2D systems. Using a combined experimental and numerical approach, we studied the key parameters for the planar and vertical growth of 2D materials and demonstrated the possibility for engineering their morphology by controlling the concentration and flow profiles. This provides a new mechanism for controllable growth of 2D MoS_2 with different orientations and morphologies for applications in energy, catalysis, electronic devices and ultrathin integrated circuits. Epitaxial MoS_2/hBN vdW heterostructure is synthesized via powder vapor transport (PVT) process, scanning/transmission electron microscopy S/TEM imaging and spectroscopy are used to study the atomic structure and chemical composition of the as-grown heterostructure, we also experimentally verify the crucial role of substrate defects on the nucleation and growth of MoS_2/hBN heterostructure. A universal and etching-free transfer technique is developed which enables transfer of the TMDs films and flakes onto arbitrary substrates with high fidelity. We demonstrate a systematic investigation of morphology and intrinsic defects in the metal organic chemical vapor deposition-(MOCVD) grown WSe_2 film, including point defects, dislocations and grain boundaries using aberration-corrected (S)TEM imaging. The orientation and stacking of as-grown WSe_2 film is explored and the presence of interlayer strain is also revealed via dark field imaging. A new type of vacancy defect is also observed along the grain boundaries of WSe_2 with reconstructed mirror symmetry, showing great possibilities in tunable devices.

TABLE OF CONTENTS

List of Figures	v
Acknowledgements.....	vi
Chapter 1 Introduction and Literature Review	1
1.1 Introduction of two-dimensional transition metal dichalcogenides	1
1.1.1 Crystal structure	1
1.1.2 Electronic Property.....	2
1.1.3 Optical Property	3
1.1.4 Catalytical property	4
1.2 Preparation methods of 2D TMDs	5
1.3 2D TMD-based Heterostructures	8
1.4 Transmission Electron Microscopy Study of 2D TMDs.....	10
1.5 Objectives and Organization of the Thesis	17
1.6 Reference	18
Chapter 2 Experimental procedure and Material Characterization.....	27
2.1 Synthesis of 2D MoS ₂ Crystals via Powder Vapor Transport.....	27
2.2 Sample preparation	28
2.2.1 Substrate preparation.....	28
2.3.2 Sample transfer.....	29
2.3 Material characterization methods	30
2.3.1 Optical Microscope	30
2.3.2 Raman and photoluminescence spectroscopy	30
2.3.3 Scanning electron microscopy.....	31
2.3.4 Transmission electron microscopy.....	31
2.4 References.....	32
Chapter 3 Understanding and Controlling synthesis of 2D crystals: From vertical to planar MoS ₂	33
3.1 Introduction and Motivation	33
3.2 Powder Vapor Transport Synthesis and Characterization of 2D MoS ₂ Crystals	35
3.3 Synthesis of 2D MoS ₂ crystals with various orientations and morphologies.....	35
3.3.1 Case I : Vertical Growth.....	36
3.3.2 Case II : Planar triangle growth	40
3.3.3 Case III: Thin film growth	42
3.4 Growth Mechanism of 2D MoS ₂ crystals	44
3.5 Chapter Summary	50
3.6 References.....	50

Chapter 4 Effect of Substrate Defects on the van der Waals Epitaxy of MoS ₂ /hBN heterostructure.....	54
4.1 Introduction and Motivation	54
4.2 Results and discussion	55
4.2.1 Simultaneous growth of MoS ₂ domains on hBN and Si/SiO ₂ substrate.....	55
4.2.2 TEM imaging and spectroscopy of the freestanding MoS ₂ /hBN heterostructures	57
4.2.3 Effect of plasma-induced substrate defects on the epitaxy of heterostructures	60
4.2.4 Atom-by-atom identification of defective hBN	62
4.2.5 Growth of all CVD-based MoS ₂ /hBN heterostructures	66
4.3 Chapter summary	70
4.4 References.....	70
Chapter 5 (S)TEM Study of Defects in MOCVD-grown WSe ₂ film.....	74
5.1 Introduction and Motivation	74
5.2 Metal-organic CVD of tungsten diselenide thin film.....	75
5.3 Sample transfer and identification	76
5.4 TEM investigation of grain and grain boundary structures of WSe ₂ thin film	78
5.4.1 Orientation and layer stacking of the MOCVD-grown WSe ₂ film	78
5.4.2 Dark field imaging (Strain induced contrast difference in +g vector and -g vector).....	80
5.4.3 Point defects in the MOCVD-grown WSe ₂ film	84
5.4.4 Grain boundary structures in the MOCVD-grown WSe ₂ film	86
5.5 Chapter summary and future work.....	89
5.6 Reference	90
Chapter 6 Conclusions	97

LIST OF FIGURES

Figure 1-1. Structure of monolayer TMDs (a) All the possible transition metals and chalcogen elements that can crystallized in layered structures are highlighted in the periodic table, from reference [3]; (b) Schematic representation of a typical MX_2 structure; (c) Energy dispersion (energy versus wavevector k) in bulk, quadrilayer (4L), bilayer (2L) and monolayer (1L) MoS_2 from ref. [2].....	2
Figure 1-2. (a) Schematic illustration of HfO_2 -top-gated monolayer MoS_2 FET device; (b) Transfer properties of field effect transistors (FETs) based on 10-layer MoS_2 with different metal contacts (Sc, Ti, Ni and Pt) from Ref. [16].....	3
Figure 1-3. Photoluminescence spectra from different regions of a monolayer WS_2 triangle (P1–P5) showing that the maximum intensity is obtained close to the edges from Ref [19]......	4
Figure 1-4 (a) High resolution scanning transmission electron microscopy (STEM) image of WS_2 monolayer with regions of distorted 1T; (b) The Density function theory calculations of the free energy of hydrogen adsorption with respect to the strain from Ref. [27].	5
Figure 1-5. Various popular routes for the synthesis of 2D materials beyond graphene, from Ref. [39]. (a) Thin-film conversion, where a solid film of metal or metal oxide is converted to an MX_2 structure by exposing it to chalcogen vapors; (b) chemical vapor transport, where constituent powders vaporizing on the hot side of the growth vessel and recondensing on the cold side; (c) powder vaporization and transport, where powders of the constituent M and X are vaporized in a dynamic flow system to react and grow thin films of 2D materials; and (d) chemical vapor deposition, where chemical vapor precursors are used to synthesize the 2D materials. Note: M, transition metal; X, chalcogen; TA, transport agent; P, pressure from Ref. [45].....	7
Figure 1-6. (a) Freestanding WSe_2 /graphene heterostructure growth by MOCVD; (b) SAED of the WSe_2 /graphene heterostructure indicate a strict crystallographic relationship between WSe_2 and graphene; (c) Photoluminescence of the freestanding WSe_2 /graphene heterostructure and WSe_2 growth on epitaxial graphene, from Ref. [54].	9
Figure 1-7. Schematic, optical image and Raman fingerprints of (a) vertical WS_2/MoS_2 bilayer heterostructure and (b) in-plane WS_2/MoS_2 heterostructure, from Ref. [61].	10
Figure 1-8. Diffraction imaging of crystal orientation and edge terminations. (a) Bright-field image of a single-crystal triangle with a Mo-zigzag edge orientation. (b) Diffraction pattern from a. (c) A line profile through experimentally measured diffraction spots (black) and Bloch-wave simulations (red). (d) Bright-field TEM image of two triangles with S-zigzag edge orientations. (e) Dark-field image of the grains and grain boundaries in CVD-grown MoS_2 , from Ref. [62].	11
Figure 1-9. Discrimination of Mo and W atoms. (a) An ADF image of a $\text{Mo}_{1-x}\text{W}_x\text{S}_2$ single layer with $x \sim 0.2$ (filtered). (b,c) Modelled structure and simulated ADF image (red:	

Mo, blue: W, yellow: S). (d,e) Profiles of the experimental and simulated ADF counts for lines indicated in a and c. Scale bar, 0.5 nm. (f) Quantitative analysis of atomic distributions, from Ref. [70].....	12
Figure 1-10. Layer-by-layer dopant analysis in AB stacked bilayer MoS ₂ at the single atom level. (a) Filtered ADF image of Se-doped bilayer MoS ₂ with AB stacking. (b) Schematic of the three types of sites in AB stacked bilayer MoS ₂ . (c) A zoom-in view of the AB stacked Se-doped bilayer MoS ₂ exhibiting a wide range of image contrast levels. (d) Site-separated image intensity histogram analysis of the image shown in panel a. (e, f) Structure model obtained from the histogram analysis. (g) Interlayer and inter-regional compositional variations obtained from site-separated ADF image analysis from Ref. [72].....	13
Figure 1-11. Intrinsic point defects in monolayer MoS ₂ . (A) Atomic resolution ADF images of various intrinsic point defects present in monolayer CVD MoS ₂ , including V _S , V _{S2} , MoS ₂ , V _{MoS3} , V _{MoS6} , and S _{2Mo} . (B) Fully relaxed structural models of the six types of point defects observed experimentally. (C) Formation energies of different point defects as functions of sulfur chemical potential. (D) Schematic representation of the defect levels, from Ref. [73].	14
Figure 1-12. (a) Low- and (b) high-angle grain boundary structure of the monolayer WS ₂ with its electronic structure. (c) Atomic structure model calculated from first principles for a 9° grain boundary composed of 6 8 dislocations. (d,e) The magnified regions of a 6 8 dislocation core in 12° and 22° grain boundaries, respectively. (f) Total electronic density of states (grey line) for the 9° (left) and 22° (right) grain boundaries composed of 6 8 structures, respectively, from Ref. [78].....	15
Figure 1-13. Atomic movements during 2H-1T phase transformation in single-layered MoS ₂ , from Ref. [79].	16
Figure 2-1. Geometry of the PVT synthesis system	27
Figure 2-2. Optical image of Au quantifoil TEM grid at different magnifications.	30
Figure 3-1. Experimentally measured temperature profile of the furnace.	35
Figure 3-2. Growth of vertical MoS ₂ nanofins on a Si substrate oriented normal to the flow stream. (a) Schematic illustration of PVT system setup with the substrate normal to the flow stream; (b) Geometry of the substrate; (c) SEM images of vertically grown MoS ₂ fins, showing different densities of MoS ₂ crystals at different positions along the substrate; (d) Numerical simulation showing concentration of Mo precursor, <i>c</i> , (background blue color); its gradient, $ \nabla c $, in front of the substrate (arrows); and carrier gas stream velocity, $ V $, (solid lines) indicating higher gas velocity at the top of the substrate; (e) Schematic illustration for vertical growth of MoS ₂ fins; (f) TEM image of a typical as-grown vertical MoS ₂ nanofins with selected area diffraction pattern from the green circle; High resolution TEM shows (g) interlayer spacing of vertical growth MoS ₂ on Si/SiO ₂	37

Figure 3-3. SEM images of vertically grown MoS₂ fins, showing different sizes of MoS₂ nanofins with different Mo precursor concentration (a) 2 mg ; (b) 1 mg and (c) 0.5 mg; Effect of carrier gas flow rate on the density of vertical MoS₂ nanofins, SEM images of vertically grown MoS₂ fins with different gas flow rates (d) 50 sccm ; (e) 200 sccm and (f) 400 sccm; Different orientations and sizes are observed showing the effect of the substrate nature on the orientation of vertical MoS₂ nanofins, SEM images of vertically grown MoS₂ fins synthesized on different substrates (g) Si/SiO₂, (h) mechanical exfoliated graphite flake, and (i) c-plane sapphire.38

Figure 3-4. Growth of horizontal MoS₂ triangles on Si/SiO₂ substrate oriented along the flow stream that is located on top of the crucible and facing down. (a) Schematic illustration of the PVT system, where there is a small gap to the end of crucible; (b) Schematic pattern of distribution of as-grown triangular-shaped MoS₂ on Si/SiO₂ substrate after growth, the triangles are mostly detectable at the edge of the blue parabola; (c) Top-view SEM images of monolayer MoS₂ triangles, where the inset shows that the lateral size of as grown triangles is $\sim 5\mu\text{m}$; (d) Numerical simulation shows the concentration of Mo precursor (background color), its gradient close to the substrate (arrows), and carrier gas velocity stream (solid lines); (e) Schematic illustration for horizontal growth of the MoS₂ triangles; (f) Raman spectrum of the as-grown monolayer MoS₂ triangular domain; (g) PL measurement of the as-grown monolayer MoS₂.....41

Figure 3-5. Growth of horizontal MoS₂ thin film on Si/SiO₂ substrate that is facing up downstream of the MoO₃ source. (a) Schematic illustration of the PVT system; (b) Schematic pattern of monolayer film deposition of MoS₂ on Si/SiO₂ substrate after growth; (c) Top-view SEM images of as-grown MoS₂ monolayer film; (d) Numerical simulation shows concentration of Mo precursor (background color), its gradient above the substrate (arrows), and carrier gas velocity stream (solid lines); (e) Schematic illustration for horizontal growth of MoS₂ monolayer film; (f) DF-TEM images of as-grown MoS₂ monolayer film, it clearly shows that the grain size is ~ 50 nm; (g) The selected area diffraction pattern of as-grown MoS₂ sheets from the green circle in f.43

Figure 3-6. SEM images (a) 50 sccm and (b) 200 sccm of the carrier gas showing planar growth, and (c) 400 sccm of the carrier gas showing vertical growth of MoS₂, A growth transformation from planar thin film to vertical growth with increasing carrier gas flow rate.44

Figure 3-7. Schematic images of 2D MoS₂ crystals (a) type-I (vertical) and (b) type-II (horizontal) texture; (c)-(e) Optical images of PVT-grown 2D MoS₂ crystals.45

Figure 3-8. Effect of Mo precursor concentration and its distribution in vicinity of the substrate on the growth mode. (a) Concentration gradient (background color) is plotted and direction of the gradient, i.e. is shown by the arrows, where the arrows are that are colored with the scale of $|\nabla c|$ for Case I. Large concentration gradient normal to the substrate is found, which describes the growth of vertical Mo nanofins. Concentration of Mo precursor (background color) and its gradient (arrows) are higher for Case II (b) compared to Case III (c) in the vicinity of the substrate. Although direction of gradient is along the substrate in both cases, lower concentration gradient

in Case III (c) leads to the formation of uniform monolayer multigrain films, in contrast to isolated MoS ₂ islands in Case II (b).	46
Figure 4-1. (a) Schematic of CVD system setup; (b) Geometry of the substrate (ME-hBN covered TEM grid), schematic illustration for freestanding MoS ₂ /ME-hBN heterostructure.....	55
Figure 4-2. (a) and (b) SEM image of MoS ₂ triangular grains epitaxially grown on ME-hBN and on Si/SiO ₂ substrate and orientated at 180° with respect to each other; (c) and (d) PL measurement of the as-grown monolayer MoS ₂ regions on top of hBN and on top of Si/SiO ₂ substrate, respectively; (e) and (f) Raman spectrum of the as-grown monolayer MoS ₂ triangular domain and hBN flake, respectively.....	56
Figure 4-3. (a) TEM image of triangular-shaped MoS ₂ grown on a freestanding ME-hBN flake, (b) SAED pattern from the red-circled MoS ₂ /hBN, yellow shows hBN pattern, blue shows MoS ₂ pattern, there is an exact 0 degree orientation relationship between the interface of epitaxial MoS ₂ and underlying ME-hBN templates; (c) ADF-STEM image of triangular-shaped MoS ₂ grown on a freestanding ME-hBN flake, sequent layers of MoS ₂ can be visualized by different contrast; (d) ADF-STEM image of triangular-shaped MoS ₂ grown on the hBN flake step edges.....	58
Figure 4-4. (a) Core loss EEL spectrum of the MoS ₂ /hBN heterostructures, the boron edge and nitrogen edge are indexed; (b-e) EDS mapping of the MoS ₂ /hBN heterostructures, elemental nitrogen, sulfur and molybdenum mapping, respectively.....	59
Figure 4-5. Effect of different reactive ion etching time (0 seconds, 10 seconds and 30 seconds, respectively) on the resulting epitaxy, domain size and substrate coverage of the as-grown heterostructure. (a-c) ADF-STEM images of as-grown heterostructure, the resulting epitaxy is also been examined by diffraction analyses in (d-f); (g-i) Histogram of misorientation angle of MoS ₂ triangles with respect to hBN substrate, indicating the degree of epitaxy.	60
Figure 4-6. Statistical analysis of (a) Resulting epitaxy; (b) Domain size and (c) Substrate coverage of the as-grown heterostructure.	62
Figure 4-7. Atomic resolution TEM images of hBN surface with different reactive ion etching time (0 seconds, 10 seconds and 30 seconds, respectively). (a, d) 0 seconds plasma etching (<i>ie.</i> no plasma treatment) hBN few layer area with an excellent surface quality free of defects and dangling bonds; (b, e) 10 seconds oxygen plasma treatment on few layer hBN area with dispersed single vacancies and oriented triangle-shaped surface defects; (c, f) 30 seconds oxygen plasma treatment on few layer hBN area with severe surface defects, trapped contaminations and particles.	63
Figure 4-8. Edge structure of hBN flake. HRTEM image of (a) zig-zag edge and (b) armchair edge.....	66
Figure 4-9. Synthesis of MoS ₂ /CVD-hBN heterostructures (a) SEM image of hBN thin film on copper substrate growth via LP-CVD; (b) TEM images of CVD-hBN after transfer	

- to a TEM grid, inset is the corresponding SAED pattern; (c) and (d) ADF-STEM image of the freestanding MoS₂/CVD-hBN heterostructures.68
- Figure 4-10. (a) BF-TEM image of MoS₂/CVD-hBN heterostructures and (b) the corresponding SAED pattern; DF-TEM image of the freestanding MoS₂/CVD-hBN heterostructures (c) corresponds to the yellow circle in (b) to show the CVD-hBN grain boundary; and (d) corresponds to the red circle in (b) to show the as-grown MoS₂ domains in which orientation can let the electron be diffracted to the spots in red circle.69
- Figure 5-1. (a) SEM image, (b) AFM image and (c) Raman spectrum of the MOCVD-grown WSe₂ thin film.....75
- Figure 5-2. The schematic illustration of the etching-free PMMA assisted transfer method.77
- Figure 5-3. (a) Conventional TEM image of MOCVD-grown WSe₂ coalesce films. (b) Selected area electron diffraction (SAED) pattern of the yellow circled part in (a), it mainly contains two sets of hexagonal diffraction patterns which is 30° misoriented, to illustrate the epitaxy of WSe₂ growth on sapphire; (c) Sequent layers (0 layer to 3 layers) of WSe₂ are identified by the intensity profile in STEM imaging, inset is the intensity profile; (d) Atomic resolution ADF/STEM image of grain and grain boundaries in WSe₂ films, a 60° grain boundary is purple-circled, direct connection of AA' stacking and AB stacking in bilayer WSe₂ is also being observed.....78
- Figure 5-4. Dark field imaging of the WSe₂ film (a) ADF-STEM image of the WSe₂ film; (b) SAED pattern of the region shows the dispersive domain orientations, a part of the diffraction spots region is selected by objective aperture denoted as "+g" vector (yellow circle) to achieve the corresponding dark field image (c); and the dark field image (d) which is get from the reversed symmetric part of the diffraction spots as "-g" vector (yellow circle); the intensity profile (redline) in (b) indicates a slight sample tilt exists during the imaging.....81
- Figure 5-5. Two dimensional schematic illustration of the Eward's Sphere construction in reciprocal space (a) Perfect-aligned for electron beam and single layer sample on the zone axis (0001) results in the equal intensity for +g and -g diffraction spots; (b) Slight sample tilt or bending induce the asymmetric cut-through between the ES and rel-rods; (c) Sample thickness affect the height of reciprocal rel-rods lead to a larger intensity difference between the diffracted spots +g and -g which may even form a two-beam condition (the -g has no intensity); (d) The positions of rel-rods are modified by lattice strain and have an influence of the cut-through between the ES and rel-rods, which light up the non-diffracted region.....82
- Figure 5-6. Intrinsic point defects in monolayer MOCVD-grown WSe₂. Atomic resolution ADF-STEM image of various point defects including (a) Se₂W; (b) V_{Se2}; (c) V_{Se}; and (d) W_{Se2}. The marked version in the lower row display the atom identities of tungsten (blue) and selenium (yellow).84

Figure 5-7. Atomic structures of dislocations and grain boundaries. ADF-STEM images of grain boundaries (a) and (d) 60° GB; (b) and (e) large angle GB (28°); (c) and (f) small angle GB (12°). The inset FFTs of the green-squared region in (a) to (c) illustrate the relative misorientation of the two grains; various polygonal structures marked by different colors as schematically shown in (d) to (f) reveal the detailed atomic structure along the grain boundaries.86

Figure 5-8. Atomic structure of heart-shaped defects along the reconstructed mirror boundaries (a) Raw and (b) marked data with polygonal structures including yellow rhombuses and red heart-shaped defects; (c) and (d) image intensity profile along the grain boundaries to show the W vacancy and antisite defects that Se substitute on W site. (e) Schematic of heart-shaped defect indicate that a V_W interact with the mirror boundary.....88

ACKNOWLEDGEMENTS

I would firstly like to express my sincere thanks and appreciation to my thesis advisor, Dr. Nasim Alem, for providing me this fascinating research opportunity, her academic guidance and constant encouragement throughout my Master study. I would like to thank my committee members Dr. Joan A. Redwing and Dr. Mauricio Terrones for their advice, consideration, time and effort.

I would also like to thank all my lab mates. Dr. Amin Azizi, always a wonderful model for me in academia; Debangshu Mukherjee, passionate, knowledgeable and hardworking professional; Steve Juhl, my comrade in arms who shares the joys and sorrows; Parivish Moradifar, a gorgeous girl who brings so much fun at work. I am also very glad to work with smart undergrads Mohammed S Abu Al-Saud, Chad Erb and Lauren Runkle, hope all of them have bright futures.

My thanks also go to all my collaborators, especially Dr. Long-Qing Chen and Dr. Kasra Momeni; Dr. Redwing and Xiaotian Zhang; and Dr. Crespi and Dr. Yuanxi Wang, who provide great assistance and help in my thesis. I would also like to thank my friends Guang Yang, Dr. Li Tang, Yan Dong for their companionship and consideration always.

Finally, I want to extend my deepest gratitude to my father Xiuli Zhang, my mother Liping Sun for their support, understanding and infinite love for me, I believe we can go through the darkest time and cherish every minutes of our lives as long as we are together.

Chapter 1

Introduction and Literature Review

1.1 Introduction of two-dimensional (2D) transition metal dichalcogenides (TMDs)

1.1.1 Crystal structure

Layered transition metal dichalcogenides (TMDs) are considered another 2D material system with the chemical formula MX_2 consisting of metal atoms M (e.g., Mo, W) and chalcogen atoms X (S, Se) with the transition metal sandwiched in between two layers of chalcogen atoms (shown in Fig. 1-1a and b). Two main polytypes of layered TMDs are 2H and 1T phases, with the transition metal atom coordination to be trigonal prismatic in the 2H and octahedral in the 1T phase. It is appealing that most atomically thin TMDs show exotic properties with respect to their bulk counterparts^{1,2,3} benefiting from the nature of anisotropic bonding (weak interlayer van Der Waals forces and strong in-plane bonds)^{4,5}. The electronic properties of TMDs range from semiconductors (MoS_2 , WS_2 , $MoSe_2$ and WSe_2) to metallic (VS_2 , NbS_2). MoS_2 , a representative semiconducting TMD, is considered as an outstanding candidate for optoelectronic devices² due to its indirect to direct bandgap transition¹ (when thickness is reduced to monolayer, shown in Fig. 1-1c) and for field-effect transistors⁶ because of the high on/off current ratios ($>10^5$)^{7,8}. It is also reported that MoS_2 can serve as a catalyst for hydrogen evolution reaction (HER) due to its catalytically active edge sites.^{9,10} Concurrent with the developments in 2D TMDs, the flourishing family of layered TMDs is not only restricted on their intrinsic properties, but also holds promise in tunable electronic and catalytic properties.

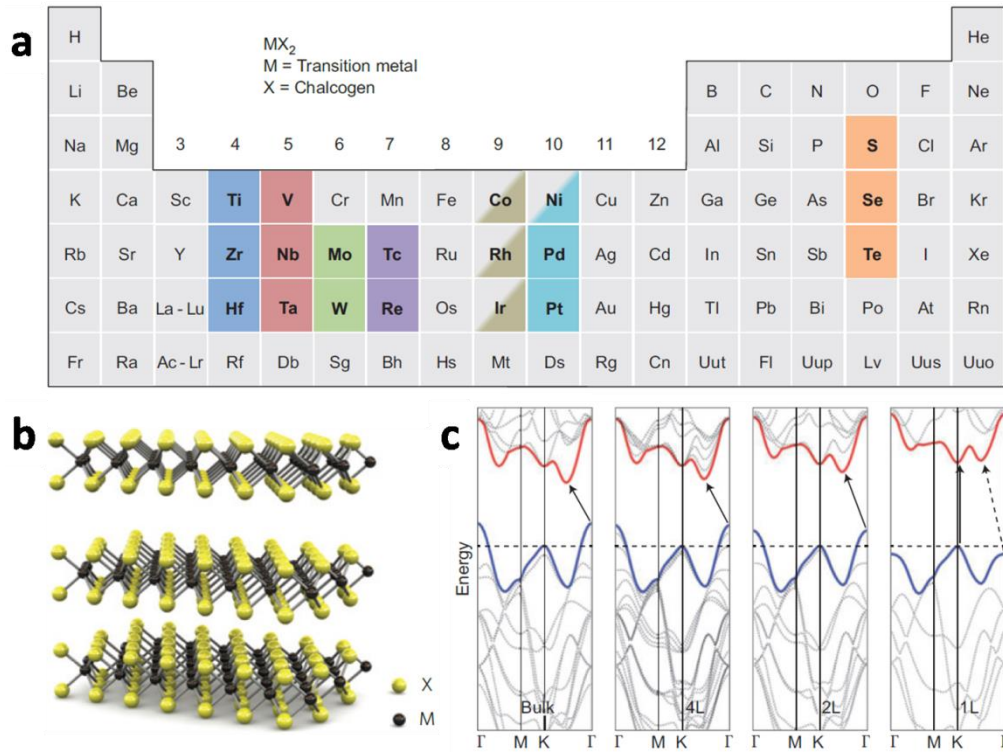


Figure 1-1. Crystal structure of monolayer TMDs (a) All the possible transition metal elements and chalcogen elements in the periodic table that can synthesized into layered structures are highlighted, from reference [3]; (b) Schematic representation of a typical MX₂ structure; (c) Electronic band structure of bulk, 4 layers (4L), 2L and monolayer MoS₂ from ref. [2].

1.1.2 Electronic Property

semiconducting 2D TMDs can be considered as unique building blocks for field effect transistors (FETs), due to the lack of dangling bonds, decent structural stability and mobility comparable to Si,¹¹. Kis and co-workers reported the first fabrication of a HfO₂-top-gated transistor based on single layer MoS₂, with an excellent on/off current ratio ($\sim 10^8$) n-type character and carrier mobility above 200 cm² V⁻¹ s⁻¹. The high-k dielectric HfO₂ gate can further improve the mobility via dielectric engineering.^{12 13} It is noted that since there lacks reliable doping techniques, one has to manipulate the metal contact to control the type of carriers. Due to the fact that metal/semiconductor contacts are inevitably Schottky barriers¹⁴, the current convection can be

dropped.¹⁵ Selective transformation of the metallic 1T phase locally on the semiconducting 2H-MoS₂ (shown in Fig. 1-2) is reported by Kappera et al. to implement near ideal ohmic contacts, which induce unprecedentedly high drive currents, high mobility and on/off ratio.¹⁶

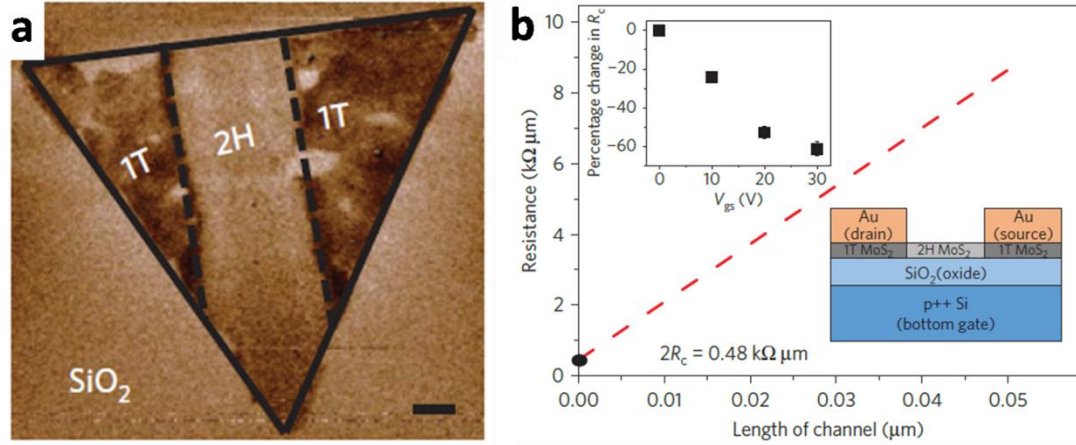


Figure 1-2. (a) 1T and 2H phase contrast differences are revealed by electrostatic force microscopy; (b) Contact resistance of 1T and 2H phase at zero gate bias, from Ref. [16].

1.1.3 Optical Property

The optical responses of 2D materials are reflecting their electronic band structures. The unique indirect to direct bandgap transition¹ (when thickness is reduced to monolayer) of TMDs makes them promising candidates for optoelectronics. The photoluminescence yielding from monolayer TMDs is 10^4 greater than that of their bulk counterparts.¹⁷ Sobhani et al. demonstrated the threefold enhancement in photocurrent and doubling of photoluminescence signals are obtained when TMDs are decorated with silica-Au nanoshell.¹⁸ Intriguing enhancement of photoluminescence intensity near the edge of TMD nanoflakes with respect to the central area (shown in Fig. 1-3) requires further understanding by theoretical and simulating investigation.¹⁹ Recent studies also reveals that tunable optical responses can be tailored through defect engineering²⁰, n- or p-type doping²¹, and controlled intercalation of alkali metal ions²².

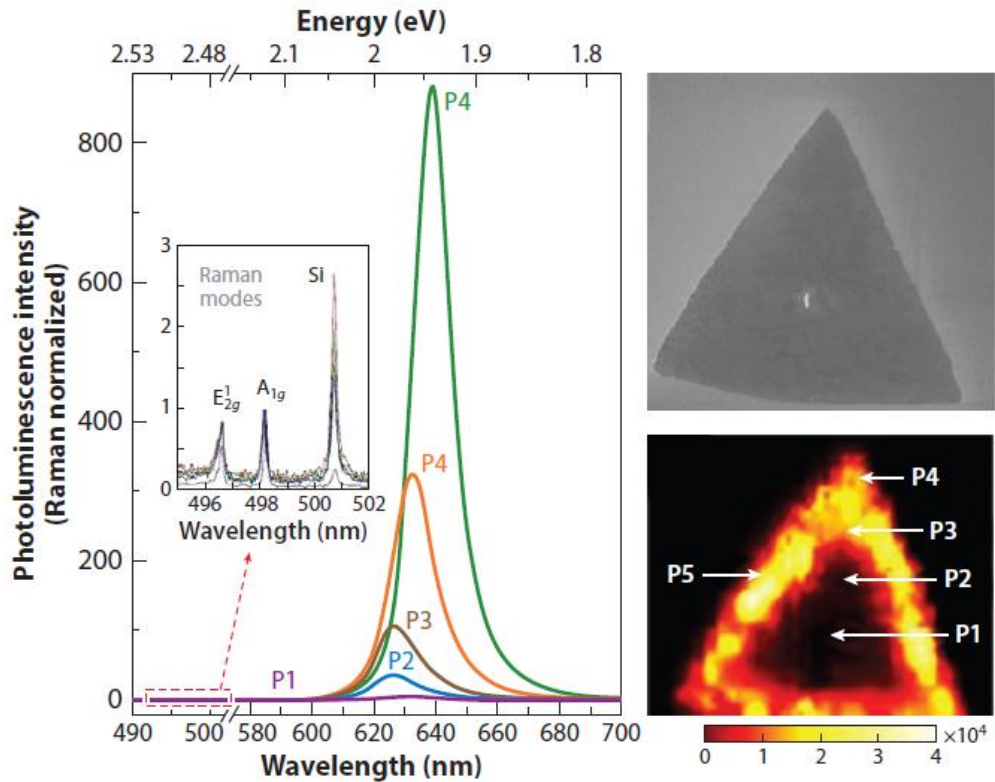


Figure 1-3. Photoluminescence yielding from specific regions of a monolayer WS_2 triangle (P1 – P5), the enhanced intensity can be observed near the edges from Ref [19].

1.1.4 Catalytic property

The development of novel and efficient catalysts for renewable hydrogen generation has brought much interest since H_2 is regarded as a superior energy source due to its large energy density and being environmental-friendly.²³ Both experimental and theoretical studies have shown that 2H- MoS_2 monolayer is catalytically active for hydrogen evolution reaction (HER) ascribed to its metallic edges, whereas its basal plane is catalytically inert.^{24,25} Structural engineering through 2H semiconducting to 1T metallic phase transformation²⁶ of MoS_2 shows a notable electrocatalytic performance, but the metastable nature of 1T phase will end up restacking in 2H semiconducting phase during the HER. It has also been demonstrated that the presence of local lattice distortion in

1T-WS₂ nanosheets have a substantial impact on the free energy of hydrogen adsorption on the surface of the samples (Fig. 1-4)²⁷, coupled with its good electrical conductivity which are beneficial for its HER catalytic activity. Vertically aligned MoS₂ nanosheets are also synthesized for catalytic applications due to having a high edge density.⁹⁻²⁸ Besides above mentioned methods, doping and alloying in TMDs²⁹⁻³⁰⁻³¹ or TMDs/carbon based nanocomposites³²⁻³³ are also widely explored to enhance the catalysis performance.

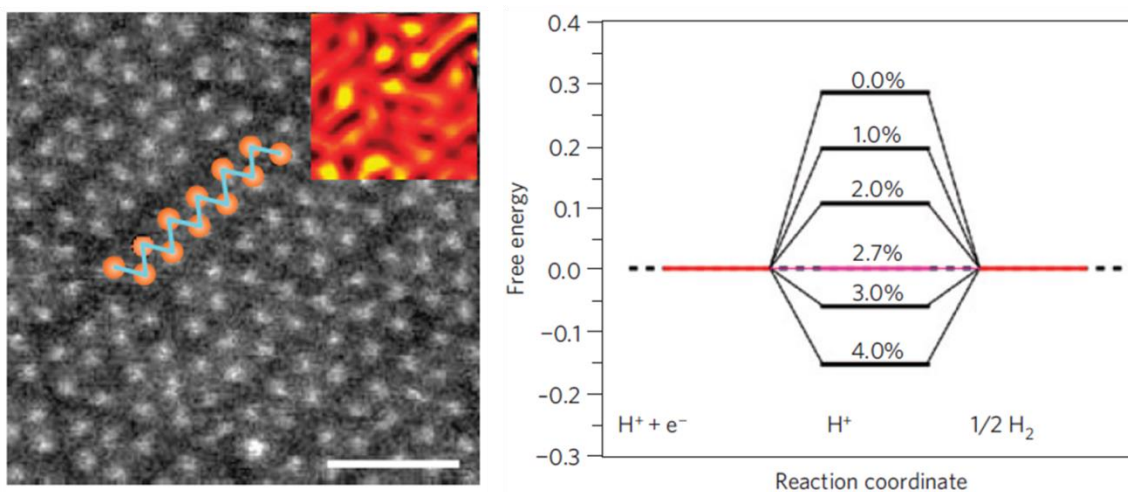


Figure 1-4 (a) Atomic resolution scanning transmission electron microscopy (STEM) image of a WS₂ monolayer with distorted 1T domain; (b) The Density functional theory calculations of the free energy of hydrogen adsorption with respect to the strain [27].

1.2 Preparation methods of 2D TMDs

TMDs are identified as van der Waals (vdW) solids with interlayer weak vdW forces and strong covalent in-plane bonds. Mechanical and chemical exfoliation processes³⁴ have been developed and widely used to separate individual 2D layers from their bulk crystals at the laboratory scale. However, it is imperative to develop synthesis methods^{35, 36} allowing uniform, scalable 2D films as well as precise control of morphology for applications. The earliest reports of obtaining 2D TMDs are mainly focused on mechanical or chemical exfoliation of naturally occurring TMDs, followed

by solution-based synthesis of 2D TMDs.³⁷ The primary route of synthesizing a uniform and scalable TMD thin films is the transition of a deposited transition metal (Mo, W, etc.) or oxide (MoO₃, WO₃, etc.) layer into MX₂ in a chalcogen (S(g), Se(g), etc.) vapor environment or solid chalcogen precursors. Recent refinement of the process has led to high quality multilayer structures³⁸ and vertically aligned sheets²⁸. This method is facile yet lacks overall uniformity to obtain a monolayer TMD. Most TMD bulk crystals for the mechanically exfoliated flakes used today are synthesized via chemical vapor transport (CVT).³⁹ Stoichiometric mixing of the transition metal and chalcogen powder along with a transport agent (I₂ or Br₂) which are sealed in a quartz ampoule is placed in a furnace with high temperature (~1000°C), where a thermal gradient along the ampoule is introduced for transportation of the precursors from the hot zone to the cool zone, depositing crystals of TMDs under near equilibrium conditions which is very time-consuming.⁴⁰ Another widely utilized synthesis process is powder vaporization. The rudimentary of the process is mainly the direct sulfurization or selenization of the transition metal oxide in a tube furnace where the two precursors are all in powder form. Upon heating, the upstream placed sulfur precursor and the hot zone placed transition metal oxide precursor are simultaneously vaporized and react with each other to coating the substrate and forming thin film.⁴¹ Numerous vapor phase growth methods, such as chemical vapor deposition (CVD) (the precursors in CVD are typically outside of the reactor tube and involve at least one gas phase precursor that thermally decomposes to deposit the film) and powder vapor transport (PVT) (no gas precursors), are successfully developed to grow horizontally stacked 2D MoS₂ monolayers^{35,42} and multilayers⁴³. Such vdW structures are ideal candidates in optoelectronic devices¹⁷ due to their indirect to direct bandgap transition as a function of thickness as well as in transistors⁶ due to their high on/off current ratios (>10⁵)^{11,8}. Vertically grown 2D TMDs, with exposed metastable edge sites and high surface energy, have also been investigated^{28,44} and show promise in catalysis and hydrogen evolution reaction^{28,9,10}.

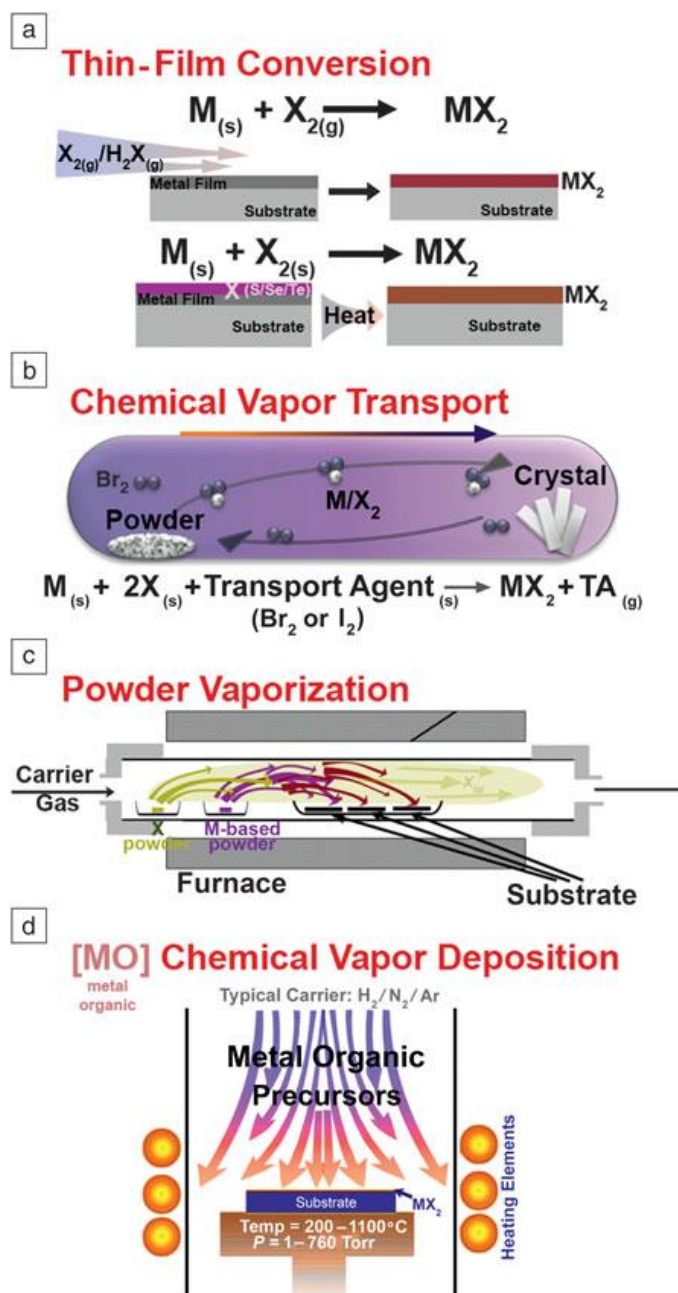


Figure 1-5. Common methods for the synthesis of 2D TMDs crystals, from Ref. [39]. (a) Thin-film conversion; (b) chemical vapor transport; (c) powder vapor transport; and (d) chemical vapor deposition.[45]

Beyond the above synthesis techniques, industrially compatible synthesis method of TMDs such as molecular beam epitaxy of monolayer TMDs allows the in-situ visualization and characterization

of the crystals during the deposition process which helps to understand the growth mechanism. metalorganic CVD (MOCVD) is another technique that can show great potential for synthesis of 2D TMDs in terms of scalability and controllability.^{46 47} This technique allows to quantitatively introduce precise ratios of metal and chalcogen precursor by switching the source gases. MOCVD technique provides not only wafer-scale reproduction but also a way of tuning the electronic and optoelectronic properties of TMDs.

1.3 2D TMD-based Heterostructures

To date, manually stacking of the mechanically exfoliated 2D material has led to many possibilities of various van der Waals heterostructures.⁴⁸ However, this direct mechanical stacking methods^{49 50} will trap contaminations and impurities at the interface of the heterostructure and further degrade the interlayer contact.^{51 52} In addition, it is not possible to control the stacking orientation of the two nanosheets. In this regard, scalable and controllable chemical vapor deposition (CVD) method is imperative to obtain vdW heterostructures with a clean interface⁵³ benefitting from elimination of post-growth handling. Efforts towards this end includes using a 2D material as a growth substrate to synthesize vertical or lateral (in-plane) heterostructures. Metallic graphene and insulating hBN are the most common substrates in literature to investigate the nucleation and growth of vertically stacked vdW heterostructures.^{53 54 55} Prior study has shown that free-standing TMD/graphene heterostructures have a significant photoluminescence quenching response compared to the corresponding monolayer TMD (Fig. 1-6), strongly suggesting effective transport of the charge carriers at the interface of the heterostructures⁵⁴.

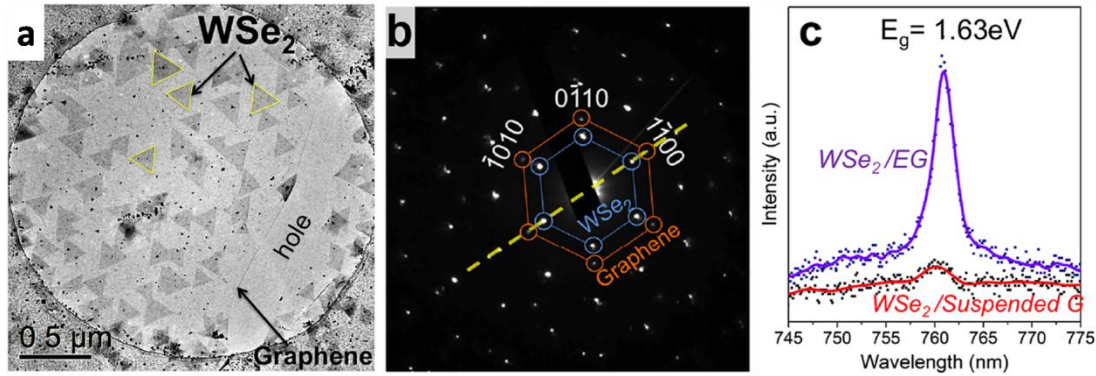


Figure 1-6. (a) Freestanding WSe_2 /graphene heterostructure growth by MOCVD; (b) SAED of the WSe_2 /graphene heterostructure indicate a perfect crystallographic relationship between WSe_2 and graphene; (c) Photoluminescence of the freestanding WSe_2 /graphene heterostructure and WSe_2 growth on epitaxial graphene [54].

The atomic structure of the defects within the interface can affect the physical, chemical and electronic properties of vdW heterostructures as well as the fabrication and functionality of devices. As a thermally conducting yet electrically insulating 2D material⁵⁶, hexagonal boron nitride (hBN) owns attractive properties such as high mechanical strength, chemical inertness, electron tunneling barrier, and high optical transparency, thus is considered as an ideal substrate to maintain the intrinsic electronic and optoelectronic properties of TMDs^{57 58} as well as an outstanding template for the growth of vdW heterostructures and fabrication of electronic devices⁵⁰.

While monolayer graphene and boron nitride can serve as the heterostructure platforms, different TMDs can also stack on top of each other to form vertical heterostructures which provide unprecedented opportunities for tailoring the electronic⁵⁹ and optoelectronic^{60 61} properties of 2D-based nanodevices. Gong et al. demonstrated a one-step fabrication method for the growth of in-plane WS_2/MoS_2 heterostructure and vertical WS_2/MoS_2 bilayer heterostructure (Fig. 1-7).⁶¹ It is reported that the vertical stacking is preferred at higher synthesis temperature, where a strong interlayer excitonic transition can be generated. While the formation of in-plane WS_2/MoS_2

heterostructure happens at lower temperatures, photoluminescence and formation of an intrinsic p-n junctions is enhanced.

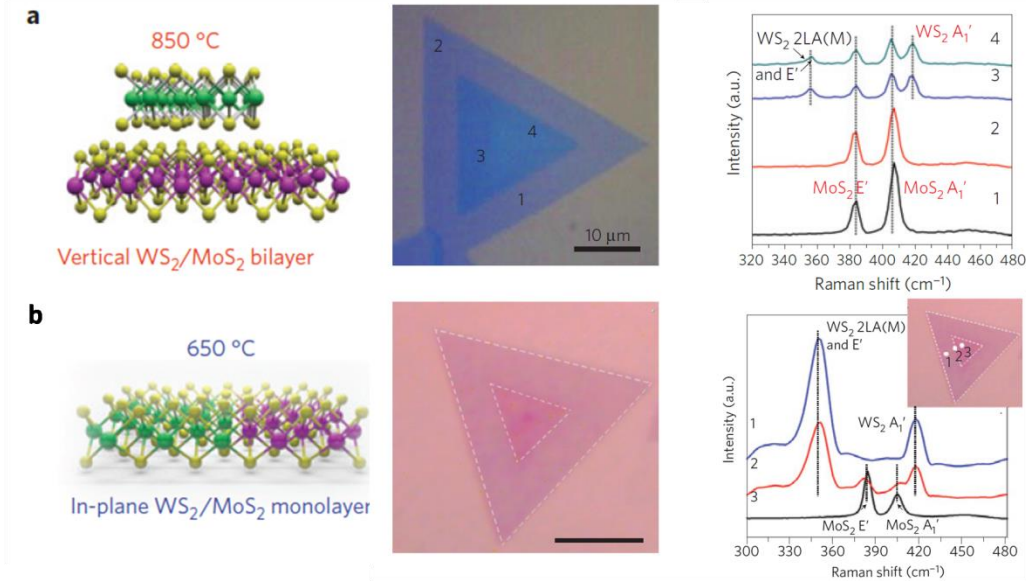


Figure 1-7. Schematic, optical image and Raman fingerprints of (a) vertical WS_2/MoS_2 bilayer heterostructure and (b) in-plane WS_2/MoS_2 heterostructure, from Ref. [61].

1.4 Transmission Electron Microscopy Study of 2D TMDs

Transmission Electron Microscopy (TEM) is a very powerful tool for the microstructure analysis of 2D materials. The firsthand information obtained from conventional TEM imaging and diffraction are the morphology of the 2D materials, the crystallinity, and lattice orientations. The crystal structure and orientation of CVD-grown MoS_2 is explored by van der Zande et al.⁶² using selected-area electron diffraction (SAED) and dark field (DF) TEM imaging (Fig. 1-8). The diffraction pattern of single crystal MoS_2 can be divided into Mo and S sublattice, which has a three-fold symmetry due to its hexagonal lattice. Therefore, the K_a spots are higher in intensity and reflect the Mo sublattice. The dominate morphology of as-grown MoS_2 are Mo-zigzag and S-zigzag edges. While the Mo-zigzag edges have a more distinct triangular morphology comparing to S-

zigzag edges, dark field images indicate the MoS₂ domains merging together with sharp grain boundaries on the atomic scale, in contrast to homoelemental graphene grain boundary structure.

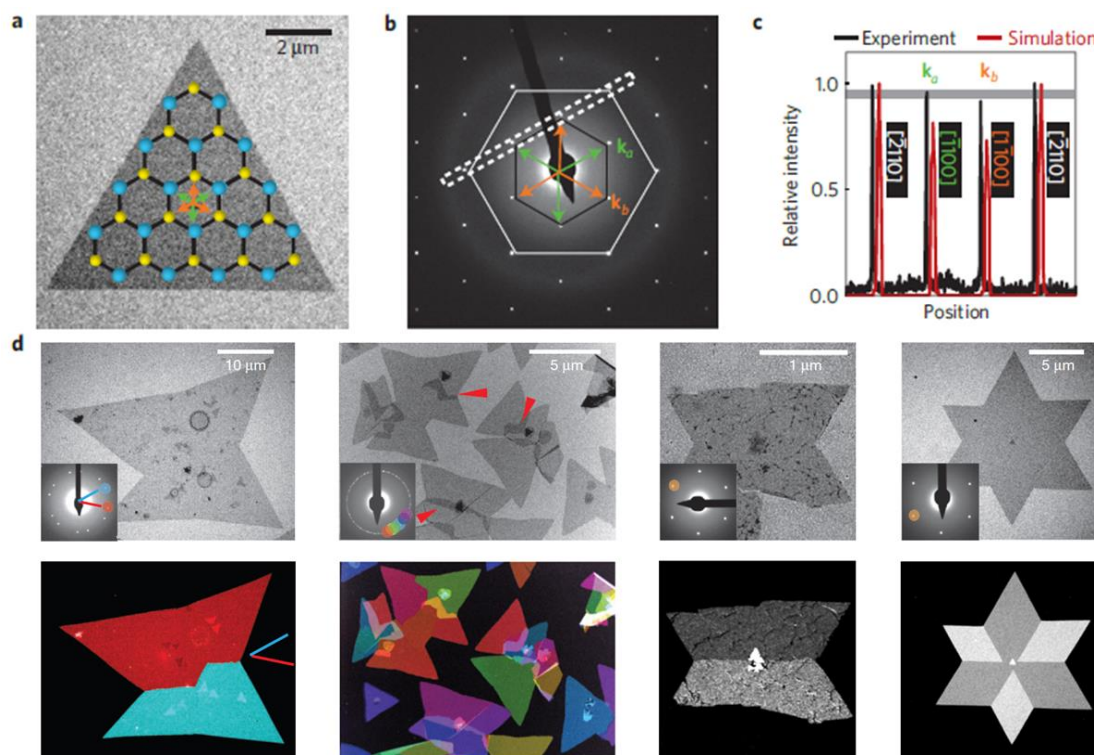


Figure 1-8. TEM imaging of CVD-MoS₂. (a) Bright-field (BF-) TEM image of a triangular single-crystal with Mo-zigzag edge terminations. (b) SAED from domain in (a). (c) Intensity profiles in obtained SAED (black) and Bloch-wave simulations (red). (d) DF-TEM images of the grains and grain boundaries in the CVD-grown MoS₂, from Ref. [62].

It has been realized by Feynman that the Transmission Electron Microscopy (TEM) in principle has the capability to directly image the atomic and chemical structure in a material.⁶³ in particular aberration-corrected electron microscopes have significantly improved the resolution to values well below 1 Angstrom.^{64 65 66 67}

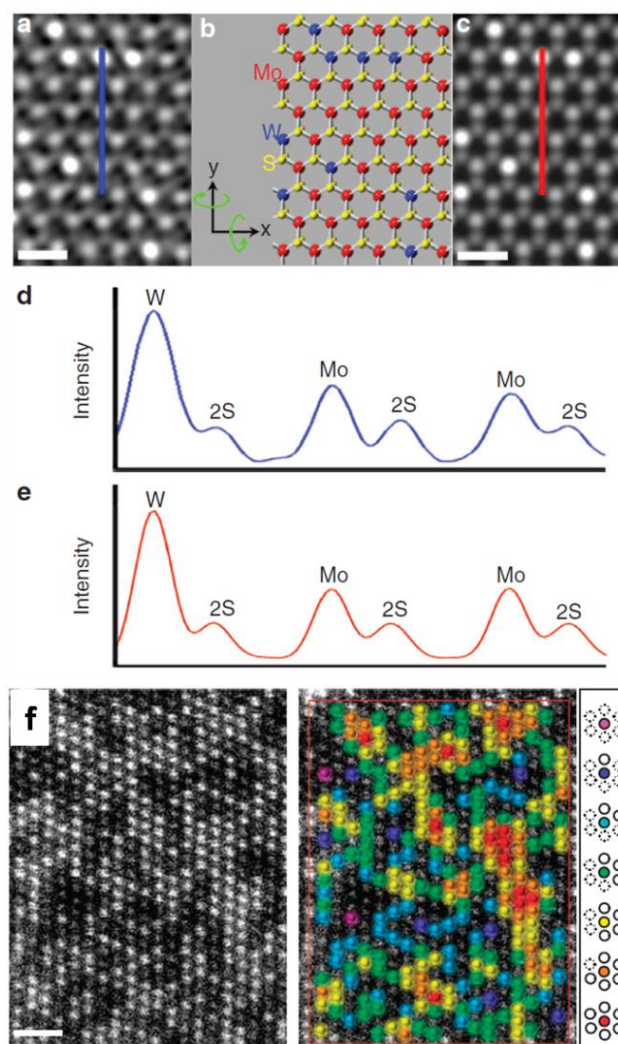


Figure 1-9. Identification of Mo and W atoms in monolayer $\text{Mo}_{1-x}\text{W}_x\text{S}_2$. (a) Atomic resolution ADF-STEM image of a monolayer $\text{Mo}_{1-x}\text{W}_x\text{S}_2$ with $x \sim 0.2$; (b) Model crystal structure and (c) simulated ADF-STEM image (red: Mo, blue: W, yellow: S); (d,e) Line profiles of the experimental and simulated image from (a) and (c); (f) Quantitative analysis of atomic distributions at the transition metal neighboring region, from Ref. [70].

Direct identification of atoms in graphene,⁶⁸ hBN⁶⁹ and TMDs^{70 71} are realized by aberration-corrected ADF-STEM imaging. Dumcenco et al. reports the quantification of W and Mo atoms in a monolayer $\text{Mo}_{1-x}\text{W}_x\text{S}_2$ alloy (shown in Fig. 1-9).⁷⁰ The neighbouring atoms of W and Mo can be counted to show the priority of homoatomic or heteroatomic nature of the constituent species. Annular dark field scanning transmission electron microscopy ADF-STEM image line profile and

quantitative simulation of the ADF profile show a perfect match with each other to distinguish the Mo and W atoms in a monolayer $\text{Mo}_{1-x}\text{W}_x\text{S}_2$ alloy. Quantitative study of the distribution of the W and Mo atoms shows that there is no preference in the neighboring sites indicating a random mixing of metal atoms in the as-synthesized alloy.

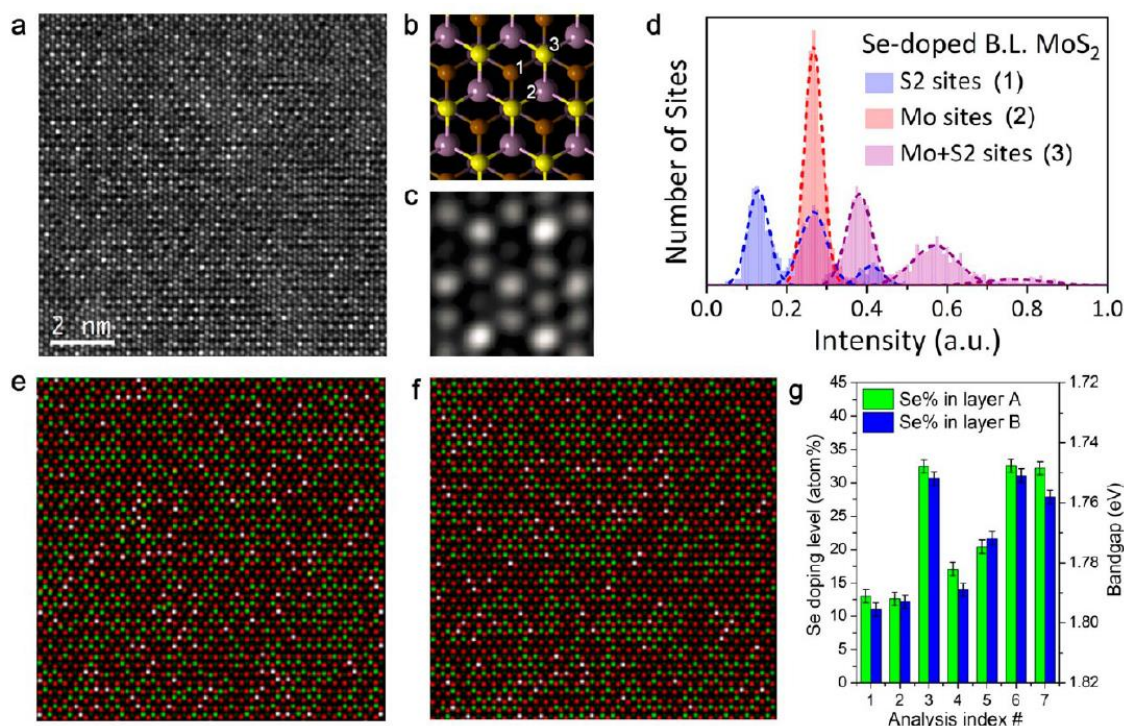


Figure 1-10. Dopant identifications in a AB-stacked bilayer MoS_2 . (a) Filtered ADF-STEM image of Se-doped AB stacked bilayer MoS_2 . (b) Model structures of the three types of sites in AB stacked bilayer MoS_2 . (c) ADF-STEM image of the AB stacked Se-doped bilayer MoS_2 , clearly shows different image contrast at different positions. (d) Intensity histogram analysis of the image shown in panel (a). (e, f and g) Structure model of the sequent layer in the bilayer MoS_2 systems, from Ref. [72].

The dopant (or alloying) atom distribution can also be identified layer-by-layer in a bilayer MoS_2 via the chemical mapping in STEM. It is demonstrated by Gong et al. that the second layer in the bilayer MoS_2 systems (AB stacking in this case) contains similar randomly-distributed Se atom concentrations (Fig. 1-10), can use a guide for understanding the growth mechanism and alloying behavior in TMDs.⁷²

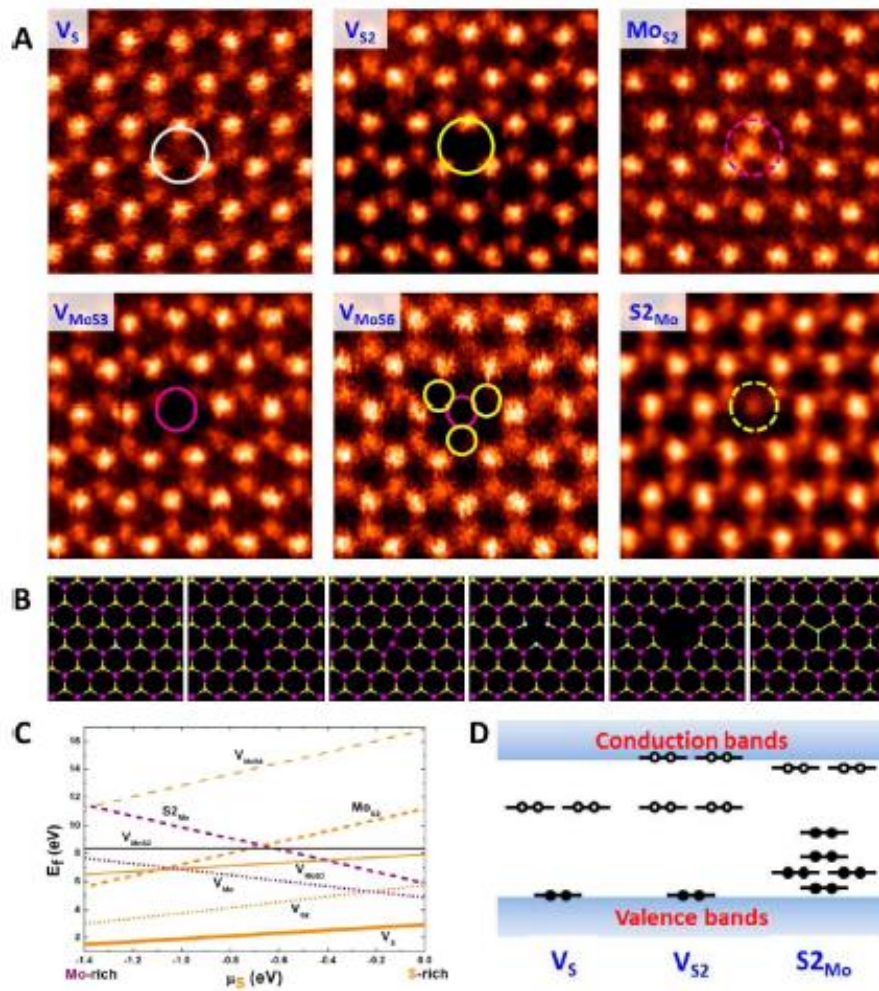


Figure 1-11. Several point defects in monolayer MoS₂. (A) Atomic resolution ADF images of vacancy and antisites point defects locate in monolayer CVD MoS₂, including V_S , V_{S2} , Mo_{S2} , V_{MoS3} , V_{MoS6} , and $S2_{Mo}$. (B) Structural models of the vacancy and antisites point defects observed experimentally. (C) Formation energies of different point defects in terms of sulfur chemical potential. (D) Schematics of the band structures with the additional defect levels, from Ref. [73].

The atomic structure of the intrinsic defects can strongly impact the physical, chemical and electronic properties of 2D materials as well as the fabrication and functionalities of the devices.

Density functional theory (DFT) calculations also show that the defects and the grain boundaries in monolayer MoS₂ can change the local density of states by introducing states in the band gap.^{73 74}

As a result, one way to tune the material properties of 2D TMDs is through defect engineering.

Zhou et al. systematically studied the intrinsic defects in a CVD-grown single layer MoS_2 , including point defects, dislocation cores at grain boundaries, and edge structures (Fig. 1-11).⁷³ Figure shows the commonly observed point defects in a CVD-grown monolayer MoS_2 , while density functional theory (DFT) calculations demonstrate the formation energy of the point defects and the induced extra local electronic states.

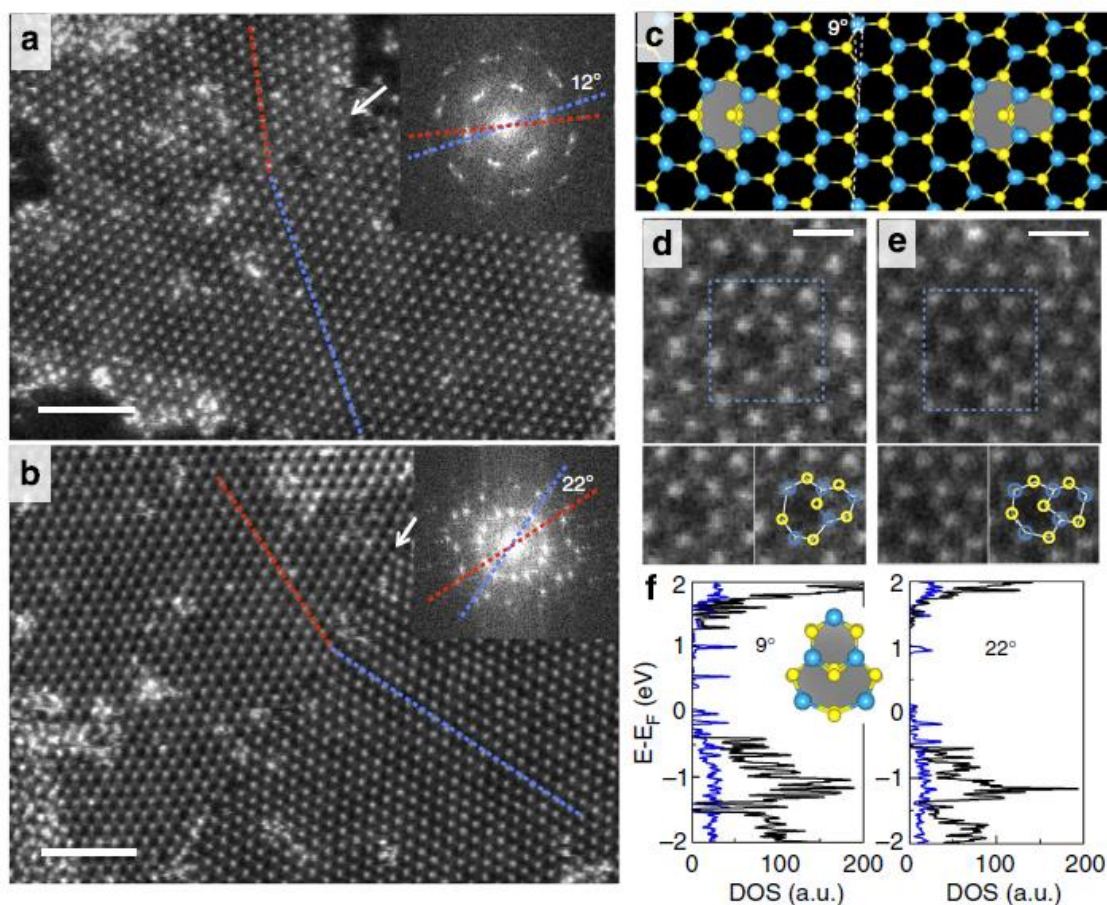


Figure 1-12. Atomic resolution ADF-STEM images of (a) Low- (12°) and (b) high-angle (22°) grain boundary structures in the single layer WS_2 ; (c) First principal simulations of a 9° grain boundary reconstructed by 6|8 dislocations; (d,e) The zoomed-in ADF-STEM images of the 6|8 structures at low- and high-angle grain boundaries, respectively; (f) DFT calculations of electronic density of states (grey line) for the 9° and 22° grain boundaries reconstructed by 6|8 dislocation cores, respectively, from Ref. [78].

Dislocation cores and grain boundaries has been extensively observed and studied in 2D graphene and hBN,^{75 76 77} which play very important roles in the electronic and mechanical properties of 2D materials. Azizi et al.⁷⁸ studied the grain boundary structures and dislocation migration in CVD-grown monolayer WS₂ consisting of 6|8 and 5|7 dislocation cores, which are predicted to introduce deep level local states acting as sinks for carrier charges. In addition, high levels of strain are measured along the grain boundaries. Further experimental observations coupled with DFT calculations indicate migration of the dislocations in WS₂ with a striking low energy barrier, unlike graphene (Fig. 1-12).

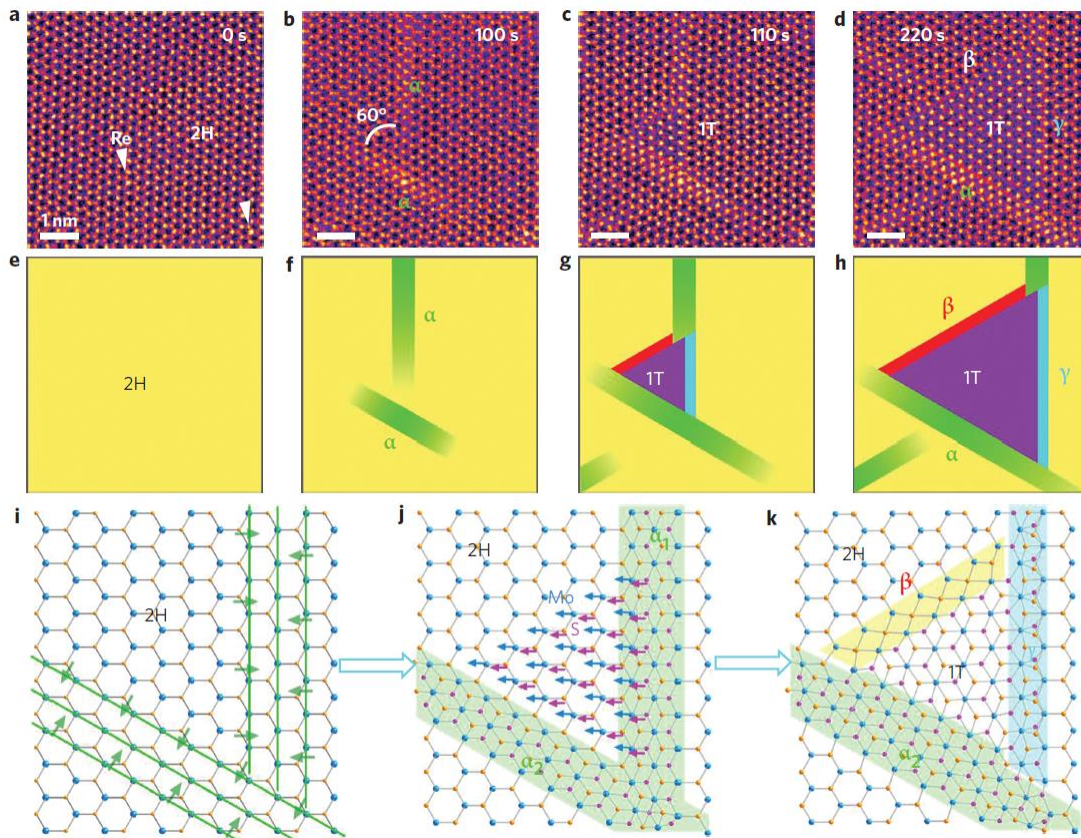


Figure 1-13. Atomic movements during 2H-1T phase transformation in single-layered MoS₂, from Ref. [79].

Phase transitions in TMDs can also be detected by STEM using in situ imaging. Lin et al. observed the crystal structure transformation from semiconducting 2H phase to metallic 1T phase in a monolayer MoS₂ involving the introduction of the intermediate α -phase as a precursor followed by the gliding of atom planes (Fig. 1-13).⁷⁹ The electron beam in TEM also can act as a well-controlled stimuli for the local phase transition in STEM, thus it can corroborate the reliable design of future low-dimensional devices.

Not only the atomic registry and defects of materials can be visualized via HR-S/TEM and aberration corrected ADF-STEM imaging, but the chemical bonding and elemental information can also be extracted from Energy Dispersive Spectroscopy (EDS) and Electron Energy Loss Spectroscopy (EELS). EDS prefers heavy elemental mapping⁵⁴ and EELS is a perfect tool for light element tracing and bonding identification⁸⁰.

1.5 Objectives and Organization of the Thesis

Chapter 1 reviews the current literature and research status of the 2D materials area including the growth and applications of pristine TMDs and TMD-based heterostructures. This thesis is also mainly focusing on the TEM investigation of 2D materials. Chapter 2 summarizes the experimental procedures such as sample preparation, transfer and characterization. Chapter 3 discusses the growth of 2D TMDs crystals from the planar to the vertical direction via powder vaporization. A systematic understanding on the growth mechanism and key parameters dominating the process is studied using a combined experimental and numerical approach.

In Chapter 4 we discuss the epitaxial growth of TMD-based heterostructures (MoS₂/hBN) using powder vaporization technique. The effects of substrate defects on the resulting epitaxy and morphology of the heterostructures are investigated using S/TEM to further help implementation

and functionality of devices in nanoscale. Chapter 5 presents a universal and etchant-free transfer technique to enable transfer of the TMDs films and flakes onto arbitrary substrates with high fidelity. A comprehensive TEM exploration of morphology and intrinsic defects in the MOCVD-grown WSe₂ film, including point defects, dislocations and grain boundaries is conducted using aberration-corrected (S)TEM imaging. Finally, chapter 5 presents the scientific conclusions and future work of this thesis.

1.6 Reference

1. Mak, K. F.; Lee, C.; Hone, J.; Shan, J.; Heinz, T. F., Atomically thin MoS₂: a new direct-gap semiconductor. *Physical Review Letters* **2010**, *105* (13), 136805.
2. Wang, Q. H.; Kalantar-Zadeh, K.; Kis, A.; Coleman, J. N.; Strano, M. S., Electronics and optoelectronics of two-dimensional transition metal dichalcogenides. *Nature nanotechnology* **2012**, *7* (11), 699-712.
3. Chhowalla, M.; Shin, H. S.; Eda, G.; Li, L.-J.; Loh, K. P.; Zhang, H., The chemistry of two-dimensional layered transition metal dichalcogenide nanosheets. *Nature chemistry* **2013**, *5* (4), 263-275.
4. Verble, J.; Wietling, T.; Reed, P., Rigid-layer lattice vibrations and van der waals bonding in hexagonal MoS₂. *Solid State Communications* **1972**, *11* (8), 941-944.
5. Tang, H.; Morrison, S. R., Optimization of the anisotropy of composite MoS₂ films. *Thin Solid Films* **1993**, *227* (1), 90-94.
6. Kim, S.; Konar, A.; Hwang, W.-S.; Lee, J. H.; Lee, J.; Yang, J.; Jung, C.; Kim, H.; Yoo, J.-B.; Choi, J.-Y., High-mobility and low-power thin-film transistors based on multilayer MoS₂ crystals. *Nature communications* **2012**, *3*, 1011.
7. Radisavljevic, B.; Radenovic, A.; Brivio, J.; Giacometti, i. V.; Kis, A., Single-layer MoS₂

transistors. *Nature nanotechnology* **2011**, 6 (3), 147-150.

8. Podzorov, V.; Gershenson, M.; Kloc, C.; Zeis, R.; Bucher, E., High-mobility field-effect transistors based on transition metal dichalcogenides. *Applied Physics Letters* **2004**, 84 (17), 3301-3303.

9. Wang, H.; Lu, Z.; Xu, S.; Kong, D.; Cha, J. J.; Zheng, G.; Hsu, P.-C.; Yan, K.; Bradshaw, D.; Prinz, F. B., Electrochemical tuning of vertically aligned MoS₂ nanofilms and its application in improving hydrogen evolution reaction. *Proceedings of the National Academy of Sciences* **2013**, 110 (49), 19701-19706.

10. Yu, Y.; Huang, S.-Y.; Li, Y.; Steinmann, S. N.; Yang, W.; Cao, L., Layer-dependent electrocatalysis of MoS₂ for hydrogen evolution. *Nano letters* **2014**, 14 (2), 553-558.

11. Radisavljevic, B.; Radenovic, A.; Brivio, J.; Giacometti, V.; Kis, A., Single-layer MoS₂ transistors. *Nature nanotechnology* **2011**, 6 (3), 147-150.

12. Jena, D.; Konar, A., Enhancement of carrier mobility in semiconductor nanostructures by dielectric engineering. *Physical review letters* **2007**, 98 (13), 136805.

13. Konar, A.; Fang, T.; Jena, D., Effect of high- κ gate dielectrics on charge transport in graphene-based field effect transistors. *Physical Review B* **2010**, 82 (11), 115452.

14. Das, S.; Chen, H.-Y.; Penumatcha, A. V.; Appenzeller, J., High performance multilayer MoS₂ transistors with scandium contacts. *Nano letters* **2012**, 13 (1), 100-105.

15. Sik Hwang, W.; Remskar, M.; Yan, R.; Protasenko, V.; Tahy, K.; Doo Chae, S.; Zhao, P.; Konar, A.; Xing, H.; Seabaugh, A., Transistors with chemically synthesized layered semiconductor WS₂ exhibiting 105 room temperature modulation and ambipolar behavior. *Applied Physics Letters* **2012**, 101 (1), 013107.

16. Kappera, R.; Voiry, D.; Yalcin, S. E.; Branch, B.; Gupta, G.; Mohite, A. D.; Chhowalla, M., Phase-engineered low-resistance contacts for ultrathin MoS₂ transistors. *Nature materials* **2014**, 13 (12), 1128-1134.

17. Yin, Z.; Li, H.; Li, H.; Jiang, L.; Shi, Y.; Sun, Y.; Lu, G.; Zhang, Q.; Chen, X.; Zhang, H., Single-layer MoS₂ phototransistors. *ACS nano* **2011**, *6* (1), 74-80.
18. Sobhani, A.; Lauchner, A.; Najmaei, S.; Ayala-Orozco, C.; Wen, F.; Lou, J.; Halas, N. J., Enhancing the photocurrent and photoluminescence of single crystal monolayer MoS₂ with resonant plasmonic nanoshells. *Applied Physics Letters* **2014**, *104* (3), 031112.
19. Gutiérrez, H. R.; Perea-López, N.; Elías, A. L.; Berkdemir, A.; Wang, B.; Lv, R.; López-Urías, F.; Crespi, V. H.; Terrones, H.; Terrones, M., Extraordinary room-temperature photoluminescence in triangular WS₂ monolayers. *Nano letters* **2012**, *13* (8), 3447-3454.
20. Nan, H.; Wang, Z.; Wang, W.; Liang, Z.; Lu, Y.; Chen, Q.; He, D.; Tan, P.; Miao, F.; Wang, X., Strong photoluminescence enhancement of MoS₂ through defect engineering and oxygen bonding. *ACS nano* **2014**, *8* (6), 5738-5745.
21. Mouri, S.; Miyauchi, Y.; Matsuda, K., Tunable photoluminescence of monolayer MoS₂ via chemical doping. *Nano letters* **2013**, *13* (12), 5944-5948.
22. Wang, Y.; Ou, J. Z.; Balendhran, S.; Chrimes, A. F.; Mortazavi, M.; Yao, D. D.; Field, M. R.; Latham, K.; Bansal, V.; Friend, J. R., Electrochemical control of photoluminescence in two-dimensional MoS₂ nanoflakes. *Acs Nano* **2013**, *7* (11), 10083-10093.
23. Dresselhaus, M.; Thomas, I., Alternative energy technologies. *Nature* **2001**, *414* (6861), 332-337.
24. Hinnemann, B.; Moses, P. G.; Bonde, J.; Jørgensen, K. P.; Nielsen, J. H.; Horch, S.; Chorkendorff, I.; Nørskov, J. K., Biomimetic hydrogen evolution: MoS₂ nanoparticles as catalyst for hydrogen evolution. *Journal of the American Chemical Society* **2005**, *127* (15), 5308-5309.
25. Jaramillo, T. F.; Jørgensen, K. P.; Bonde, J.; Nielsen, J. H.; Horch, S.; Chorkendorff, I., Identification of active edge sites for electrochemical H₂ evolution from MoS₂ nanocatalysts. *science* **2007**, *317* (5834), 100-102.
26. Voiry, D.; Salehi, M.; Silva, R.; Fujita, T.; Chen, M.; Asefa, T.; Shenoy, V. B.; Eda, G.;

Chhowalla, M., Conducting MoS₂ nanosheets as catalysts for hydrogen evolution reaction. *Nano letters* **2013**, *13* (12), 6222-6227.

27. Voiry, D.; Yamaguchi, H.; Li, J.; Silva, R.; Alves, D. C.; Fujita, T.; Chen, M.; Asefa, T.; Shenoy, V. B.; Eda, G., Enhanced catalytic activity in strained chemically exfoliated WS₂ nanosheets for hydrogen evolution. *Nature materials* **2013**, *12* (9), 850-855.

28. Kong, D.; Wang, H.; Cha, J. J.; Pasta, M.; Koski, K. J.; Yao, J.; Cui, Y., Synthesis of MoS₂ and MoSe₂ films with vertically aligned layers. *Nano letters* **2013**, *13* (3), 1341-1347.

29. Kiran, V.; Mukherjee, D.; Jenjeti, R. N.; Sampath, S., Active guests in the MoS₂/MoSe₂ host lattice: efficient hydrogen evolution using few-layer alloys of MoS_{2(1-x)}Se_{2x}. *Nanoscale* **2014**, *6* (21), 12856-12863.

30. Xu, K.; Wang, F.; Wang, Z.; Zhan, X.; Wang, Q.; Cheng, Z.; Safdar, M.; He, J., Component-Controllable WS_{2(1-x)}Se_{2x} Nanotubes for Efficient Hydrogen Evolution Reaction. *ACS nano* **2014**, *8* (8), 8468-8476.

31. Yang, L.; Fu, Q.; Wang, W.; Huang, J.; Huang, J.; Zhang, J.; Xiang, B., Large-area synthesis of monolayered MoS_{2(1-x)}Se_{2x} with a tunable band gap and its enhanced electrochemical catalytic activity. *Nanoscale* **2015**, *7* (23), 10490-10497.

32. Yan, Y.; Xia, B.; Li, N.; Xu, Z.; Fisher, A.; Wang, X., Vertically oriented MoS₂ and WS₂ nanosheets directly grown on carbon cloth as efficient and stable 3-dimensional hydrogen-evolving cathodes. *Journal of Materials Chemistry A* **2015**, *3* (1), 131-135.

33. Li, Y.; Wang, H.; Xie, L.; Liang, Y.; Hong, G.; Dai, H., MoS₂ nanoparticles grown on graphene: an advanced catalyst for the hydrogen evolution reaction. *Journal of the American Chemical Society* **2011**, *133* (19), 7296-7299.

34. Lukowski, M. A.; Daniel, A. S.; Meng, F.; Forticaux, A.; Li, L.; Jin, S., Enhanced hydrogen evolution catalysis from chemically exfoliated metallic MoS₂ nanosheets. *Journal of the American Chemical Society* **2013**, *135* (28), 10274-10277.

35. Liu, K.-K.; Zhang, W.; Lee, Y.-H.; Lin, Y.-C.; Chang, M.-T.; Su, C.-Y.; Chang, C.-S.; Li, H.; Shi, Y.; Zhang, H., Growth of large-area and highly crystalline MoS₂ thin layers on insulating substrates. *Nano letters* **2012**, *12* (3), 1538-1544.
36. Zhan, Y.; Liu, Z.; Najmaei, S.; Ajayan, P. M.; Lou, J., Large-area vapor-phase growth and characterization of MoS₂ atomic layers on a SiO₂ substrate. *Small* **2012**, *8* (7), 966-971.
37. Arutyunyan, L.; Khurshudyan, E. K., Synthesis of molybdenum disulfide from sulfomolybdate solutions at high temperatures. *Geochem. Int* **1966**, *3*, 479-485.
38. Tarasov, A.; Campbell, P. M.; Tsai, M. Y.; Hesabi, Z. R.; Feirer, J.; Graham, S.; Ready, W. J.; Vogel, E. M., Highly Uniform Trilayer Molybdenum Disulfide for Wafer-Scale Device Fabrication. *Advanced Functional Materials* **2014**, *24* (40), 6389-6400.
39. Mercier, J., Recent developments in chemical vapor transport in closed tubes. *Journal of Crystal Growth* **1982**, *56* (2), 235-244.
40. Al-Hilli, A.; Evans, B., The preparation and properties of transition metal dichalcogenide single crystals. *Journal of Crystal Growth* **1972**, *15* (2), 93-101.
41. Lin, Y.-C.; Zhang, W.; Huang, J.-K.; Liu, K.-K.; Lee, Y.-H.; Liang, C.-T.; Chu, C.-W.; Li, L.-J., Wafer-scale MoS₂ thin layers prepared by MoO₃ sulfurization. *Nanoscale* **2012**, *4* (20), 6637-6641.
42. Lee, Y. H.; Zhang, X. Q.; Zhang, W.; Chang, M. T.; Lin, C. T.; Chang, K. D.; Yu, Y. C.; Wang, J. T. W.; Chang, C. S.; Li, L. J., Synthesis of Large-Area MoS₂ Atomic Layers with Chemical Vapor Deposition. *Advanced Materials* **2012**, *24* (17), 2320-2325.
43. Bosi, M., Growth and synthesis of mono and few-layers transition metal dichalcogenides by vapour techniques: a review. *RSC Advances* **2015**, *5* (92), 75500-75518.
44. Li, H.; Wu, H.; Yuan, S.; Qian, H., Synthesis and characterization of vertically standing MoS₂ nanosheets. *Scientific reports* **2016**, *6*.
45. Vogel, E. M.; Robinson, J. A., Two-dimensional layered transition-metal dichalcogenides

for versatile properties and applications. *MRS Bulletin* **2015**, 40 (07), 558-563.

46. Kang, K.; Xie, S.; Huang, L.; Han, Y.; Huang, P. Y.; Mak, K. F.; Kim, C.-J.; Muller, D.; Park, J., High-mobility three-atom-thick semiconducting films with wafer-scale homogeneity. *Nature* **2015**, 520 (7549), 656-660.

47. Zhang, X.; Al Balushi, Z. Y.; Zhang, F.; Choudhury, T. H.; Eichfeld, S. M.; Alem, N.; Jackson, T. N.; Robinson, J. A.; Redwing, J. M., Influence of Carbon in Metalorganic Chemical Vapor Deposition of Few-Layer WSe₂ Thin Films. *Journal of Electronic Materials* **2016**, 45 (12), 6273-6279.

48. Roy, T.; Tosun, M.; Kang, J. S.; Sachid, A. B.; Desai, S. B.; Hettick, M.; Hu, C. C.; Javey, A., Field-effect transistors built from all two-dimensional material components. *Acs Nano* **2014**, 8 (6), 6259-6264.

49. Lee, G.-H.; Yu, Y.-J.; Cui, X.; Petrone, N.; Lee, C.-H.; Choi, M. S.; Lee, D.-Y.; Lee, C.; Yoo, W. J.; Watanabe, K., Flexible and transparent MoS₂ field-effect transistors on hexagonal boron nitride-graphene heterostructures. *ACS nano* **2013**, 7 (9), 7931-7936.

50. Cui, X.; Lee, G.-H.; Kim, Y. D.; Arefe, G.; Huang, P. Y.; Lee, C.-H.; Chenet, D. A.; Zhang, X.; Wang, L.; Ye, F., Multi-terminal transport measurements of MoS₂ using a van der Waals heterostructure device platform. *Nature nanotechnology* **2015**, 10 (6), 534-540.

51. Britnell, L.; Gorbachev, R.; Jalil, R.; Belle, B.; Schedin, F.; Mishchenko, A.; Georgiou, T.; Katsnelson, M.; Eaves, L.; Morozov, S., Field-effect tunneling transistor based on vertical graphene heterostructures. *Science* **2012**, 335 (6071), 947-950.

52. Haigh, S.; Gholinia, A.; Jalil, R.; Romani, S.; Britnell, L.; Elias, D.; Novoselov, K.; Ponomarenko, L.; Geim, A.; Gorbachev, R., Cross-sectional imaging of individual layers and buried interfaces of graphene-based heterostructures and superlattices. *Nature materials* **2012**, 11 (9), 764-767.

53. Lin, Y.-C.; Lu, N.; Perea-Lopez, N.; Li, J.; Lin, Z.; Peng, X.; Lee, C. H.; Sun, C.; Calderin,

- L.; Browning, P. N., Direct synthesis of van der Waals solids. *ACS nano* **2014**, *8* (4), 3715-3723.
54. Azizi, A.; Eichfeld, S.; Geschwind, G.; Zhang, K.; Jiang, B.; Mukherjee, D.; Hossain, L.; Piasecki, A. F.; Kabius, B.; Robinson, J. A., Freestanding van der waals heterostructures of graphene and transition metal dichalcogenides. *ACS nano* **2015**, *9* (5), 4882-4890.
55. Wang, S.; Wang, X.; Warner, J. H., All Chemical Vapor Deposition Growth of MoS₂: h-BN Vertical van der Waals Heterostructures. *ACS nano* **2015**, *9* (5), 5246-5254.
56. Gibb, A.; Alem, N.; Zettl, A., Low pressure chemical vapor deposition synthesis of hexagonal boron nitride on polycrystalline metal foils. *physica status solidi (b)* **2013**, *250* (12), 2727-2731.
57. Dean, C.; Young, A.; Cadden-Zimansky, P.; Wang, L.; Ren, H.; Watanabe, K.; Taniguchi, T.; Kim, P.; Hone, J.; Shepard, K., Multicomponent fractional quantum Hall effect in graphene. *Nature Physics* **2011**, *7* (9), 693-696.
58. Dean, C. R.; Young, A. F.; Meric, I.; Lee, C.; Wang, L.; Sorgenfrei, S.; Watanabe, K.; Taniguchi, T.; Kim, P.; Shepard, K., Boron nitride substrates for high-quality graphene electronics. *Nature nanotechnology* **2010**, *5* (10), 722-726.
59. Li, X.; Lin, M.-W.; Lin, J.; Huang, B.; Piretzky, A. A.; Ma, C.; Wang, K.; Zhou, W.; Pantelides, S. T.; Chi, M., Two-dimensional GaSe/MoSe₂ misfit bilayer heterojunctions by van der Waals epitaxy. *Science advances* **2016**, *2* (4), e1501882.
60. Zhang, X.; Meng, F.; Christianson, J. R.; Arroyo-Torres, C.; Lukowski, M. A.; Liang, D.; Schmidt, J. R.; Jin, S., Vertical heterostructures of layered metal chalcogenides by van der Waals epitaxy. *Nano letters* **2014**, *14* (6), 3047-3054.
61. Gong, Y.; Lin, J.; Wang, X.; Shi, G.; Lei, S.; Lin, Z.; Zou, X.; Ye, G.; Vajtai, R.; Yakobson, B. I., Vertical and in-plane heterostructures from WS₂/MoS₂ monolayers. *Nature materials* **2014**, *13* (12), 1135-1142.
62. Van Der Zande, A. M.; Huang, P. Y.; Chenet, D. A.; Berkelbach, T. C.; You, Y.; Lee, G.-H.;

Heinz, T. F.; Reichman, D. R.; Muller, D. A.; Hone, J. C., Grains and grain boundaries in highly crystalline monolayer molybdenum disulphide. *Nature materials* **2013**, *12* (6), 554-561.

63. Hey, A. J., *Feynman and computation: exploring the limits of computers*. Perseus Books: 1999.

64. Haider, M.; Uhlemann, S.; Schwan, E.; Rose, H.; Kabius, B.; Urban, K., Electron microscopy image enhanced. *Nature* **1998**, *392* (6678), 768.

65. Batson, P.; Dellby, N.; Krivanek, O., Sub-ångstrom resolution using aberration corrected electron optics. *Nature* **2002**, *418* (6898), 617-620.

66. Muller, D.; Kourkoutis, L. F.; Murfitt, M.; Song, J.; Hwang, H.; Silcox, J.; Dellby, N.; Krivanek, O., Atomic-scale chemical imaging of composition and bonding by aberration-corrected microscopy. *Science* **2008**, *319* (5866), 1073-1076.

67. Williams, D. B.; Carter, C. B., *Transmission electron microscopy: a textbook for materials science*. Springer, New York London: 2009.

68. Suenaga, K.; Koshino, M., Atom-by-atom spectroscopy at graphene edge. *Nature* **2010**, *468* (7327), 1088-1090.

69. Alem, N.; Erni, R.; Kisielowski, C.; Rossell, M. D.; Gannett, W.; Zettl, A., Atomically thin hexagonal boron nitride probed by ultrahigh-resolution transmission electron microscopy. *Physical Review B* **2009**, *80* (15), 155425.

70. Dumcenco, D. O.; Kobayashi, H.; Liu, Z.; Huang, Y.-S.; Suenaga, K., Visualization and quantification of transition metal atomic mixing in $\text{Mo}_{1-x}\text{W}_x\text{S}_2$ single layers. *Nature communications* **2013**, *4*, 1351.

71. Liu, Z.; Suenaga, K.; Wang, Z.; Shi, Z.; Okunishi, E.; Iijima, S., Identification of active atomic defects in a monolayered tungsten disulphide nanoribbon. *Nature communications* **2011**, *2*, 213.

72. Gong, Y.; Liu, Z.; Lupini, A. R.; Shi, G.; Lin, J.; Najmaei, S.; Lin, Z.; Elías, A. L.;

Berkdemir, A.; You, G., Band gap engineering and layer-by-layer mapping of selenium-doped molybdenum disulfide. *Nano letters* **2013**, *14* (2), 442-449.

73. Zhou, W.; Zou, X.; Najmaei, S.; Liu, Z.; Shi, Y.; Kong, J.; Lou, J.; Ajayan, P. M.; Yakobson, B. I.; Idrobo, J.-C., Intrinsic structural defects in monolayer molybdenum disulfide. *Nano letters* **2013**, *13* (6), 2615-2622.

74. Zou, X.; Liu, Y.; Yakobson, B. I., Predicting dislocations and grain boundaries in two-dimensional metal-disulfides from the first principles. *Nano letters* **2012**, *13* (1), 253-258.

75. Lehtinen, O.; Kurasch, S.; Krashennnikov, A.; Kaiser, U., Atomic scale study of the life cycle of a dislocation in graphene from birth to annihilation. *Nature communications* **2013**, *4*.

76. Butz, B.; Dolle, C.; Niekkel, F.; Weber, K.; Waldmann, D.; Weber, H. B.; Meyer, B.; Spiecker, E., Dislocations in bilayer graphene. *Nature* **2014**, *505* (7484), 533-537.

77. Gibb, A. L.; Alem, N.; Chen, J.-H.; Erickson, K. J.; Ciston, J.; Gautam, A.; Linck, M.; Zettl, A., Atomic resolution imaging of grain boundary defects in monolayer chemical vapor deposition-grown hexagonal boron nitride. *Journal of the American Chemical Society* **2013**, *135* (18), 6758-6761.

78. Azizi, A.; Zou, X.; Ercius, P.; Zhang, Z.; Elías, A. L.; Perea-López, N.; Stone, G.; Terrones, M.; Yakobson, B. I.; Alem, N., Dislocation motion and grain boundary migration in two-dimensional tungsten disulphide. *Nature communications* **2014**, *5*.

79. Lin, Y.-C.; Dumcenco, D. O.; Huang, Y.-S.; Suenaga, K., Atomic mechanism of the semiconducting-to-metallic phase transition in single-layered MoS₂. *Nature nanotechnology* **2014**, *9* (5), 391-396.

80. Alem, N.; Yazyev, O. V.; Kisielowski, C.; Denes, P.; Dahmen, U.; Hartel, P.; Haider, M.; Bischoff, M.; Jiang, B.; Louie, S. G., Probing the out-of-plane distortion of single point defects in atomically thin hexagonal boron nitride at the picometer scale. *Physical review letters* **2011**, *106* (12), 126102.

Chapter 2

Experimental procedure and Material Characterization

2.1 Synthesis of 2D MoS₂ Crystals via Powder Vapor Transport (PVT)

Molybdenum disulfide (MoS₂) is synthesized via oxide powder vaporization by three configurations (Fig. 2-1, detailed configurations in Chapter 3). In all cases, ~1mg MoO₃ (99.99% Sigma Aldrich) is placed in the crucible in the hot zone of the furnace (~ 700°C). Sulfur powder (~150mg, 99.5% Alfa Aesar) is put in another crucible, which is placed 15 cm upstream away from the center crucible, the temperature for sulfur is ~230 °C. High purity nitrogen is introduced into the furnace as carrier gas for the whole process.

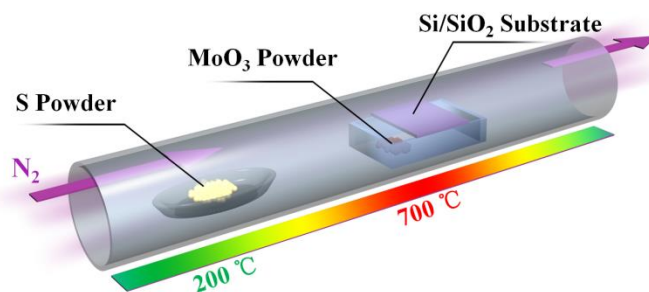


Figure 2-1. Geometry of the PVT synthesis system

The PVT growth is conducted at atmospheric pressure in a 15 mm (diameter) horizontal tube furnace (Mini-mite). The quartz tube is initially pumped down to 1×10^{-4} mbar and purged with nitrogen gas repeatedly to remove air contamination. The growth conditions are as follows: (1) pre-heating for 20 min at 150 °C to remove water contamination; (2) Ramp the temperature up to 400 °C in 15 min and hold at 400 °C for 10 min; (3) Ramp the temperature up to 700 °C in 30 min; (4)

Hold the temperature at 700 °C for 10 min and cool down to 560 °C; (5) Open furnace for rapid cooling. The whole process is at a flow rate of 200 sccm high purity nitrogen.

2.2 Sample preparation

2.2.1 Substrate preparation

Silicon substrates with 300nm of SiO₂ were used as growth substrates for 2D MoS₂ crystals (in chapter 3). These substrates were cleaned as follow: they were first sonicated in acetone and isopropyl alcohol for 10 minutes each and then cleaned with deionized water, followed by immersion in Piranha solution (3:1 mixture of H₂SO₄ and H₂O₂) for 30 min. Afterwards they were sonicated and rinsed with deionized water again and dried with pure nitrogen.

Both freestanding mechanically exfoliated (ME)-hBN on the TEM grid and ME-hBN on Si/SiO₂ (300nm SiO₂ thickness) substrate are used as templates to fabricate MoS₂/hBN heterostructure. hBN was first mechanically exfoliated using the scotch tape and placed onto the Si/SiO₂ substrate. PMMA transfer method was further utilized to transfer ME-hBN (CVD-hBN) onto Au quantifoil TEM grid. The TEM grid is placed on the Si/SiO₂ substrate downstream in the hot-zone crucible.

In order to explore the effect of substrate quality on the nucleation and growth of the heterostructure, we explored the effect of defects generated on the hBN substrate through surface plasma treatment. For plasma treatment, the hBN flakes are placed on top of the Si/SiO₂ substrate. Reactive ion etching treatment was conducted by the Tepla M4L Plasma Etch system. 50 Sccm oxygen gas is introduced to system under 200 mTorr. The radio frequency (13.56 Megahertz) power is set to 50W to generate plasma, the plasma treatment is from 0 seconds to 30 seconds.

After the plasma treatment, we use PMMA-assisted transfer method to obtain freestanding hBN templates for the growth of MoS₂/hBN heterostructures.

2.3.2 Sample transfer

The as-synthesized 2D flakes or films are transferred onto TEM grid for further TEM investigation by the following methods. Graphene or hexagonal boron nitride is transferred to TEM grid as a growth template prior to the heterostructure fabrication. The detailed transfer process is being described in the reported literature.¹ PMMA-assisted transfer method of 2D materials are widely used for transfer of 2D flakes and films which includes PMMA spin-coating and wet-etching of the substrate.² Here in this thesis, we improved the PMMA-assisted transfer method without wet-etching process to avoid the damage and contaminations (details are in Chapter 5). Another transfer technique is also used to effectively transfer 2D material flakes by assistance of polyimide. Compared to PMMA, polyimide leaves less hydrocarbon contaminations on the transferred sample after it is removed. The detailed transfer process is described in the literature.³

Vertical growth of MoS₂ was transferred onto the TEM grid from the substrate by mechanical scratching, and sonication in IPA. A drop of the solution was further placed on the TEM grid for analysis. Monolayer MoS₂ film was transferred to the TEM grid by PMMA method. WSe₂ thin films was transferred to the TEM grid by a modified PMMA-assisted method (details in Chapter 5).

2.3 Material characterization methods

2.3.1 Optical Microscope

The optical microscope uses the visible light and a set of lenses to magnify images of small specimens, the magnification can be ranged from 5X to 100X.

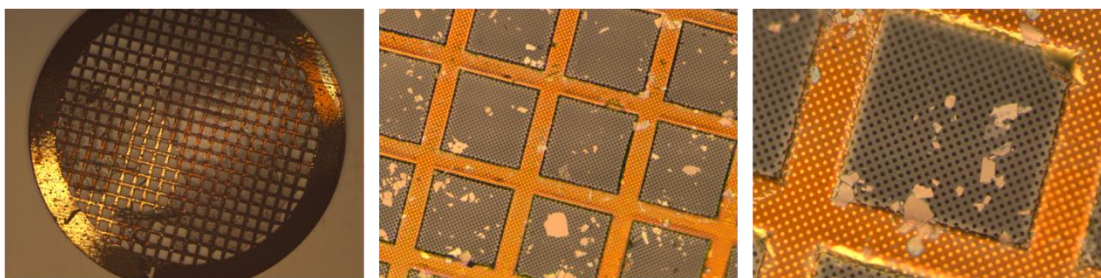


Figure 2-2. Optical image of Au quantifoil TEM grid at different magnifications.

The optical images of Au quantifoil TEM grid is shown in Fig. 2-2. The TEM grid has a standard size of 3 mm in diameter and is made of gold in this grid. The use of gold instead of cheaper copper grid is mainly due to two concerns: (1) The substrate for large area CVD growth of graphene and hBN films are mainly annealed copper. In contrast, the gold TEM grids that are used during the sample transfer are resistant to etching and remain intact. In addition, Au is also sulfur-resistant when the TEM grid is directly used for the substrate to grow the MoS₂ via powder vaporization. As a result the TEM grid with the Graphene or BN substrate on it can be placed in the furnace with no unwanted chemical reaction.

2.3.2 Raman and photoluminescence spectroscopy

Raman spectroscopy is a light scattering analytical technique. The information from Raman spectroscopy can be used to identify chemistry, molecular structure, effects of bonding,

stress/strain. The scale at which information can be obtained also varies from tens of nanometers to a few millimeters. Photoluminescence (PL) spectroscopy is used to probe the electronic structure of materials. A Witec confocal Raman system with 532 nm laser was utilized for Raman/PL characterization with an operation power ~ 1 mW, at Penn State Material Characterization Lab (MCL). A silicon chip was used to calibrate the spectrometer prior to data collection. The objective lens used was 100X. The laser spot size is ~ 100 nm with an exposure time of 60s.

2.3.3 Scanning electron microscopy

A focused electron beam is used to scan specimen in Scanning electron microscopy (SEM) from the optical to nanoscale range. Secondary electron backscattered electrons, generated from the specimen due to electron-specimen interaction, are collected by a detector to map out the local morphology and compositional information of the specimen, respectively. SEM was carried out by Leo 1530 and Zeiss Merlin FESEM, at Penn State nanofabrication Lab.

2.3.4 Transmission electron microscopy

Transmission electron microscopy (TEM), FEI Tecnai G², Talos S/TEM, and Titan³ (60-300) at 80 kV at Penn State University was used to examine and study the atomic structure and chemistry of the TMDs and TMD-based heterostructures. FEI Tecnai G² owns a thermionic gun source and is equipped with a GIF Quantum spectrometer at 80kV which is suitable to do conventional TEM imaging and EEL spectroscopy. FEI Talos is equipped with a field emission gun source which is suitable for HRTEM and STEM imaging, EDS mapping is also available on Talos. FEI Titan³ (60-300) is equipped with both image corrector and probe corrector with a gun monochromator providing sub-Angstrom resolution in both HREM and STEM imaging modes.

2.4 References

1. Regan, W.; Alem, N.; Alemán, B.; Geng, B.; Girit, Ç.; Maserati, L.; Wang, F.; Crommie, M.; Zettl, A., A direct transfer of layer-area graphene. *Applied Physics Letters* 2010, 96 (11), 113102.
2. Elias, A. L.; Perea-López, N.; Castro-Beltrán, A.; Berkdemir, A.; Lv, R.; Feng, S.; Long, A. D.; Hayashi, T.; Kim, Y. A.; Endo, M., Controlled synthesis and transfer of large-area WS₂ sheets: from single layer to few layers. *Acs Nano* 2013, 7 (6), 5235-5242.
3. Meyer, J. C.; Chuvilin, A.; Algara-Siller, G.; Biskupek, J.; Kaiser, U., Selective sputtering and atomic resolution imaging of atomically thin boron nitride membranes. *Nano letters* 2009, 9 (7), 2683-2689.

Chapter 3

Understanding and Controlling synthesis of 2D crystals: From vertical to planar MoS₂

3.1 Introduction and Motivation

The TMDs are structures with an atomic layer of transition metal in between two layers of chalcogen atoms. They are identified as van der Waals (vdW) solids with interlayer weak vdW forces and strong covalent in-plane bonds. Mechanical and chemical exfoliation processes¹ have been developed and widely used to separate individual 2D layers from their bulk crystals at the lab scale. However, it is imperative to develop synthesis methods^{2, 3} allowing uniform, scalable 2D films as well as precise control of morphology for applications. Numerous vapor phase growth methods, such as CVD (the precursors in CVD are typically outside of the reactor tube and at least involving one gas phase precursors, and thermally decompose to deposit the film) and PVT (no gas precursors), are successfully developed to grow horizontally stacked 2D MoS₂ monolayers^{2,4} and multilayers⁵. Such vdW structures are ideal candidates in optoelectronic devices⁶ due to their indirect to direct bandgap transition as a function of thickness as well as in transistors⁷ due to their high on/off current ratios ($>10^5$)^{8,9}. Vertically grown 2D TMDs, with exposed metastable edge sites and high surface energy, have also been investigated^{10,11} and show promise in catalysis and hydrogen evolution reaction^{10,12,13}.

Although significant progress has been made in the synthesis of 2D crystals, little progress has been done to fundamentally address the underlying nucleation and growth mechanisms that control the morphology resulting from synthesis. This understanding is important since material properties are

strong functions of crystallographic orientation and morphology. Despite the extensive study of these structures, the key controlling mechanisms behind the resulting morphology in these crystals are yet to be understood.

As an example, in the family of 2D crystal TMDs, atoms on the basal plane of 2D TMDs do not have dangling bonds and thus are not chemically reactive, while atoms at the edges of the basal plane have higher free energy as preferred nucleation sites. Thus, during the synthesis, sheets tend to grow laterally into monolayer structures.¹⁰ It is also reported that holding a constant low Mo precursor partial pressure (P_{Mo}) is beneficial to grow uniform monolayer thin film over a large area^{14,15}. There are also cases showing that quick sulfurization of metal-seeded substrates will lead to growth of vertically standing MoS₂ nanosheets,^{10,16} which is driven by reduction in the elastic strain energy that forms during the horizontal growth of MoS₂ nanosheets on the substrate. None of those studies point out the critical parameters dictating the horizontal-to-vertical orientation transition during MoS₂ growth. This understanding is necessary before we can design new growth mechanisms to facilitate the development of new functionalized devices with novel applications.

This chapter shows a combination of experimental research with theoretical and computational simulations to better understand the underlying physics and chemistry that governs nucleation and growth mechanisms in 2D vdW structures. Here, 2D MoS₂ nanostructures are directly grown on Si substrates by transporting and sulfurizing the metal oxide powder. A shift is observed from vertical to horizontal growth as a result of altering the concentration and concentration gradient of Mo precursor through altering the flow of carrier gas and placing the substrate at different locations with different orientations in the furnace. This fundamental understanding can lead to a controllable growth of 2D TMD crystals with various morphologies suitable for a wide range of applications such as energy harvesting and nanoelectronics¹⁴.

3.2 Powder Vapor Transport Synthesis and Characterization of 2D MoS₂ Crystals

Silicon substrates with 300nm of SiO₂ were used as growth substrates. Molybdenum disulfide (MoS₂) is synthesized via oxide powder vaporization by three configurations. The setup of vertical MoS₂ growth is shown in Fig. 3-2a. Temperature profile of the APCVD furnace along the downstream direction obtained from experimental measurements is shown in Fig. 3-1. Temperature of sulfur source is ~230°C and for Mo source and substrate, placing at the hot-zone area, the temperature is 700°C and constant during the growth.

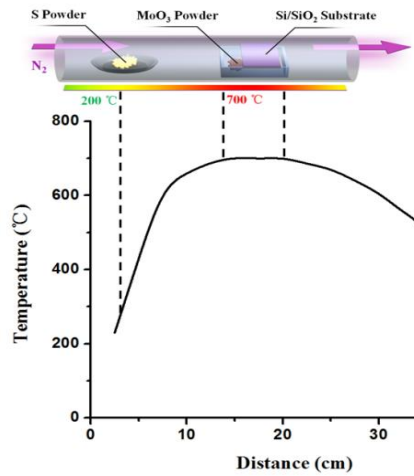


Figure 3-1. Experimentally measured temperature profile of the furnace.

3.3 Synthesis of 2D MoS₂ crystals with various orientations and morphologies

We used a conventional atmosphere pressure powder vapor transport technique with varied substrate positions to investigate the critical parameters controlling the growth morphology of 2D MoS₂. The 2D numerical model was developed using the commercial finite element software package COMSOL,¹⁷ the finite element method was employed to solve the coupled heat transfer, fluid flow, and diffusion problems involved in the powder vaporization process. Three different cases were considered: (i) substrate surface oriented normal to the flow stream in the hot-zone

MoO₃ precursor crucible (Fig. 3-2a), (ii) substrate surface oriented parallel to the flow stream and located on top of the crucible and facing down (Fig. 3-4a), and (iii) substrate surface parallel to the flow stream positioned in downstream flow and facing up (Fig. 3-5a).

3.3.1 Case I : Vertical Growth

Facing toward the upstream (Fig. 3-2a-b), the vertically placed substrate shows a color change with a gradient darker on the top. The SEM images of the vertically-standing MoS₂ nanosheets grown on an Si/SiO₂ substrate are shown in Fig. 1c, indicating higher density of MoS₂ nanofins at the top area (marked as 1). The numerical simulation results for concentration of Mo precursor and flow in the PVT environment around the substrate are shown in Fig. 3-2d, which indicates a change in Mo concentration along the substrate and a Mo concentration gradient normal to it. Simulation results indicate significant reduction in the carrier gas velocity at the bottom of the substrate. This will reduce the mass flow of precursor, resulting in smaller number of nuclei and subsequently lower density of as grown nanofins. A lower concentration gradient is also observed near the bottom part of the substrate indicating a smaller thermodynamic driving force for the growth of nanofins, which can also reduce the density of vertical nanosheets. Figure 3-2e illustrates where the basal plane of MoS₂ is normal to the substrate with the growth orientation within the (002) plane that corresponds to TEM results. A typical as-synthesized MoS₂ nanofin with a lateral size of $\sim 1 \mu\text{m}$ is shown in Fig. 3-2f, the edge of the nanosheet with five MoS₂ layers (Fig. 3-2g) with an interlayer spacing of $\sim 0.61 \pm 0.01 \text{ nm}$ indicating synthesis of thick nanosheets vertically standing on the substrate.¹⁰ These results further demonstrate that the as-grown vertically standing nanosheets are single crystal multi-layer MoS₂.

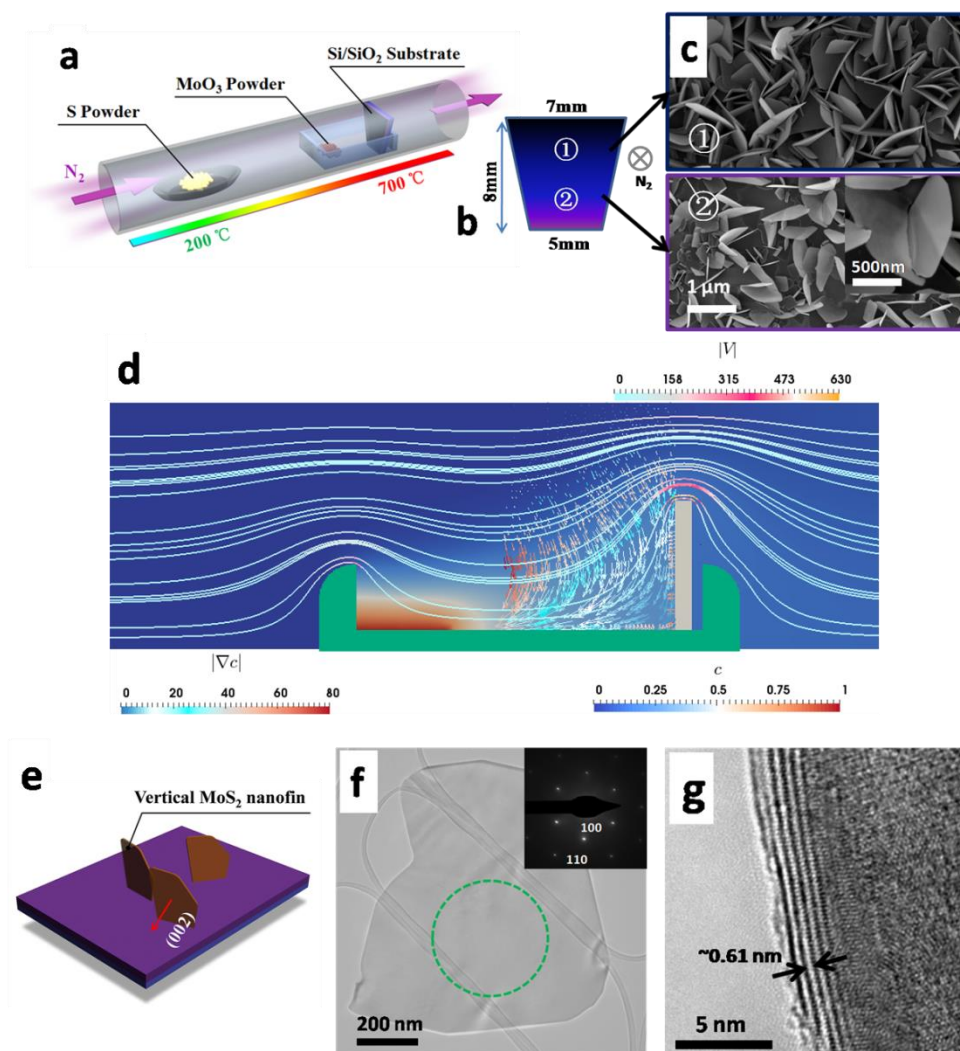


Figure 3-2. Growth of vertical MoS_2 nanofins on a Si substrate oriented normal to the flow stream. (a) Schematic illustration of PVT system setup with the substrate normal to the flow stream; (b) Geometry of the substrate; (c) SEM images of vertically grown MoS_2 fins, showing different densities of MoS_2 crystals at different positions along the substrate; (d) Numerical simulation showing concentration of Mo precursor, c , (background blue color); its gradient, $|\nabla c|$, in front of the substrate (arrows); and carrier gas stream velocity, $|V|$, (solid lines) indicating higher gas velocity at the top of the substrate; (e) Schematic illustration for vertical growth of MoS_2 fins; (f) TEM image of a typical as-grown vertical MoS_2 nanofins with selected area diffraction pattern from the green circle; High resolution TEM shows (g) interlayer spacing of vertical growth MoS_2 on Si/SiO₂.

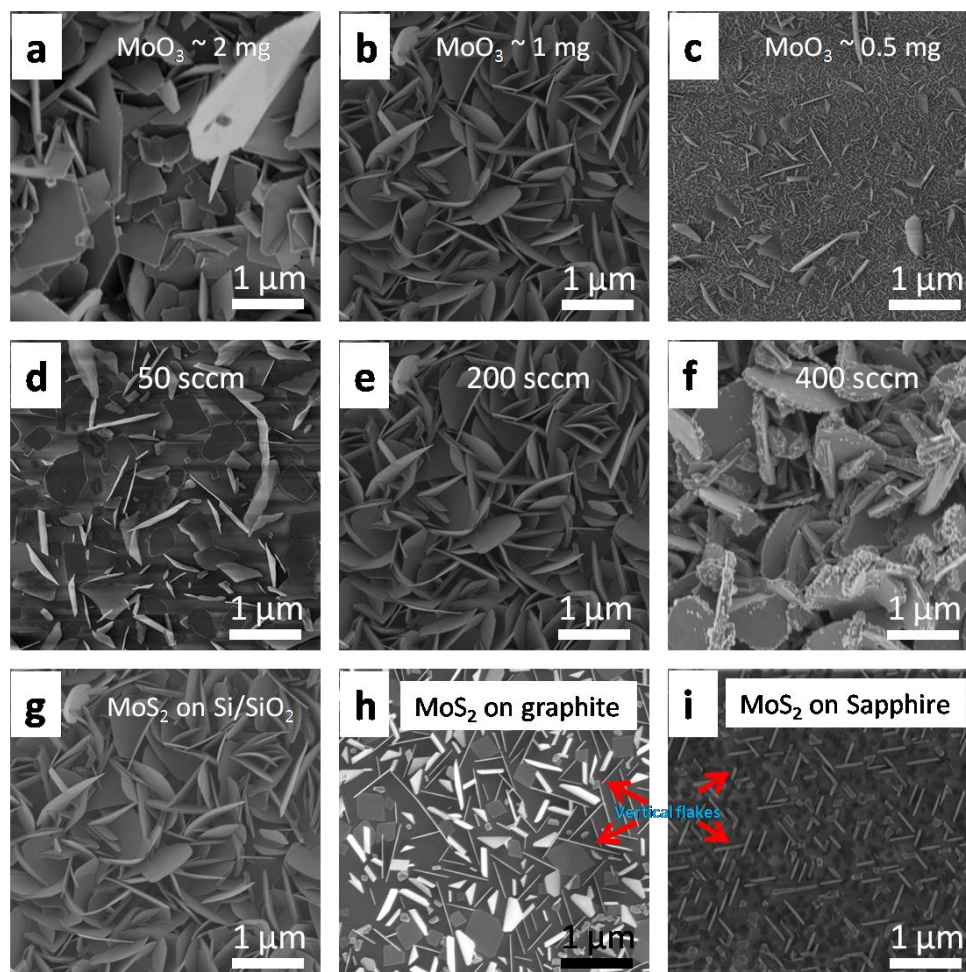


Figure 3-3. SEM images of vertically grown MoS_2 fins, showing different sizes of MoS_2 nanofins with different Mo precursor concentration (a) 2 mg ; (b) 1 mg and (c) 0.5 mg; Effect of carrier gas flow rate on the density of vertical MoS_2 nanofins, SEM images of vertically grown MoS_2 fins with different gas flow rates (d) 50 sccm ; (e) 200 sccm and (f) 400 sccm; Different orientations and sizes are observed showing the effect of the substrate nature on the orientation of vertical MoS_2 nanofins, SEM images of vertically grown MoS_2 fins synthesized on different substrates (g) Si/SiO₂, (h) mechanical exfoliated graphite flake, and (i) c-plane sapphire.

The size of vertical MoS_2 structures can also be tuned by adjusting the concentration gradient as it determines the magnitude of thermodynamic driving force for the growth via the Mullins-Sekerka instability and the growth mechanism, which affects both the nucleation and growth rate. To demonstrate the feasibility of controlling the size of the vertical nanofins by concentration gradient, a set of experiments for the same configuration are performed with concentration of precursor

changing by a factor of 2 (Fig. 3-3a-c) with other parameter fixed. Given that numerical simulations are performed for a normalized concentration, the results can be extended to this case (with only a different scaling factor). The vertical MoS₂ nanostructures are still considered as the dominant structures as we reduced the concentration of precursor, however they are smaller in size due to the smaller amount of precursor and concentration gradient in this case (from Fig. 3-3a to 3-3c). Large number of tiny nanostructures can be detected in between the large nanofins (Fig. 3-3c), indicating a dense packing of nuclei similar to the case with higher precursor concentration (Fig. 3-2c). However, only a limited number of these nuclei are grown to a fraction of height of the ones grown in Fig. 3-2c, indicating the lack of sufficient concentration of precursors for the growth of these vertical nanostructures to a significant size.

The density of the nanofins is also dependent on the change of the precursor flow rate. A set of experiments are performed as shown in Case I, with the flow rate of carrier gas (Nitrogen) varying from 50sccm to 400sccm with other factor fixed. The SEM images in Fig. 3-3d-f indicate that, as the flow rate increases, more precursor will be delivered onto the surface of the substrate. Therefore, the density of as-synthesized vertical nanofins increases and the flakes become thicker. It is noted that we have not seen obvious changes on the direction of the vertical MoS₂ nanosheets with respect to growth parameters in this case. The nanofins are observed as vertically grown with slight vertical angle misorientations and no particular epitaxy with respect to the substrate. We believe this is because of the poor crystallinity and roughness of the SiO₂ substrate surface which leads to randomly oriented nuclei leading to randomly oriented vertical nanofins. A set of experiments (Fig. 3-3g-i) of MoS₂ growth on different substrate surface is explored to show the effect of the substrate nature on the nucleation and growth. Mechanically exfoliated graphite surface owns a perfect crystallinity and atomically flat surface, from the SEM image of MoS₂ grow on graphite (Fig. 3-3h), several perfectly vertical nanosheets are observed on the substrate besides few randomly

oriented MoS₂ islands which suggests the role of the substrate surface on the nucleation and growth. Also graphite and SiO₂ have different chemistries which can significantly affect the nucleation of MoS₂ on the substrate. As a comparison, c-plane sapphire with (0001) direction is also used as the growth substrate for vertical MoS₂ nanosheets. These experiments indicate perfectly vertical nanosheets on the substrate as the growth on graphite. In addition, we observed a certain epitaxial growth of the vertical nanofins on the substrate with all the nanofins following a specific orientation with respect to the substrate. This clearly demonstrate the substrate chemical and atomic structure nature play a crucial role on the nucleation, growth and orientation of vertical MoS₂ nanofins.

3.3.2 Case II : Planar triangle growth

Planar triangular-shaped MoS₂ was synthesized by placing the substrate facing down on top of the crucible and leaving a small gap at the end of the crucible (Fig. 3-4a) to ensure the transport of carrier gas. Deposition on the substrate after growth is shown in Fig. 2b, where the concentration of the Mo precursor in the central area of the substrate is too high to achieve 2D crystals because the substrate is very close to the MoO₃ source. However, the pressure of Mo reaches proper values to form 2D MoS₂ equilateral triangles along a parabolic curve on the substrate (Fig 3-4b). Isolated MoS₂ islands with a side length of ~5 μm are observed along the parabolic curve (Fig. 3-4c and schematic image in Fig. 3-4e). Two regions can be detected in the area where the SEM images were collected (Fig. 3-4c): (i) the area closer to the precursor source with many small MoS₂ triangles, and (ii) the area with larger yet fewer MoS₂ triangles. A large number of tiny MoS₂ nuclei are also observed in this area.

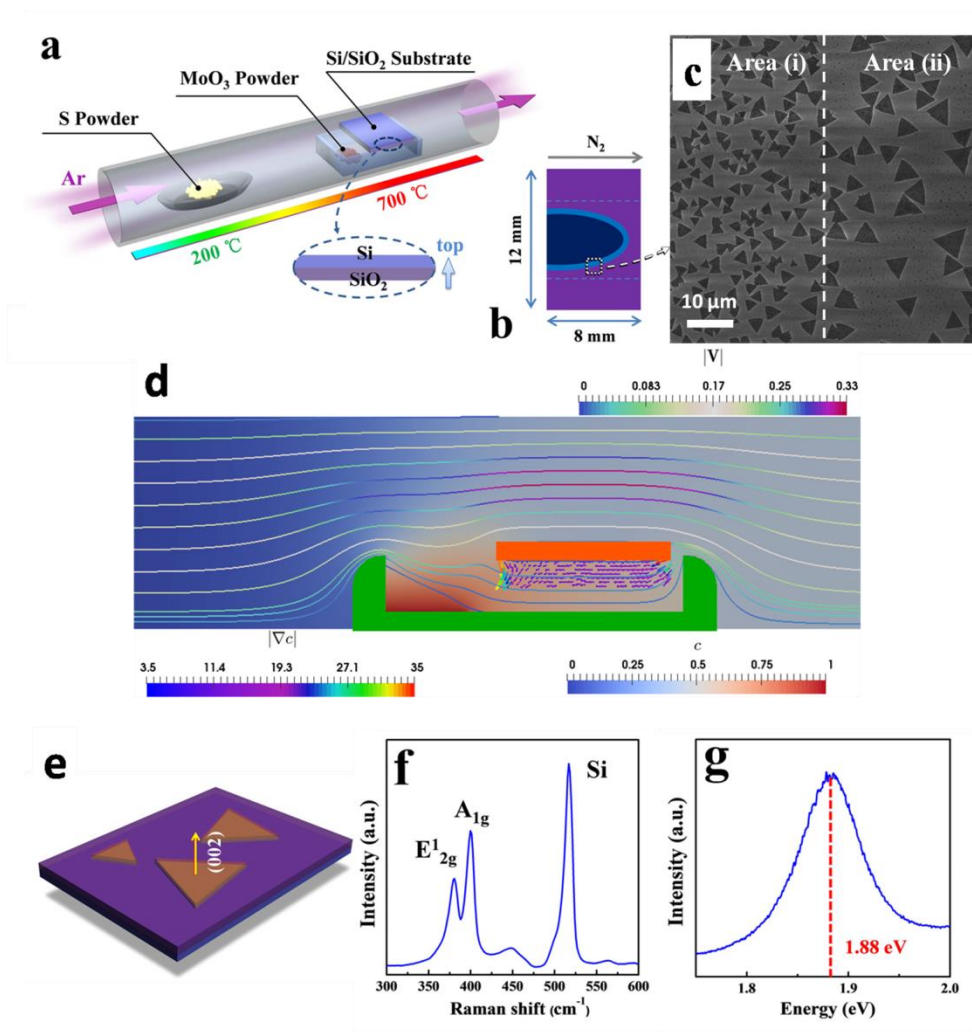


Figure 3-4. Growth of horizontal MoS₂ triangles on Si/SiO₂ substrate oriented along the flow stream that is located on top of the crucible and facing down. (a) Schematic illustration of the PVT system, where there is a small gap to the end of crucible; (b) Schematic pattern of distribution of as-grown triangular-shaped MoS₂ on Si/SiO₂ substrate after growth, the triangles are mostly detectable at the edge of the blue parabola; (c) Top-view SEM images of monolayer MoS₂ triangles, where the inset shows that the lateral size of as grown triangles is $\sim 5\mu\text{m}$; (d) Numerical simulation shows the concentration of Mo precursor (background color), its gradient close to the substrate (arrows), and carrier gas velocity stream (solid lines); (e) Schematic illustration for horizontal growth of the MoS₂ triangles; (f) Raman spectrum of the as-grown monolayer MoS₂ triangular domain; (g) PL measurement of the as-grown monolayer MoS₂

The numerical simulations (Fig. 3-4d) show the concentration and flow of MoO₃ around the substrate in this setup. These simulations show a small change in the Mo concentration along the substrate and almost no concentration gradient normal to the substrate. Raman spectrum (Fig. 3-

4f) shows two characteristic peaks corresponding to two vibrational modes in MoS₂, the E_{2g} mode and A_{1g} mode related to the in- and out-of-plane vibrations of molybdenum and sulfur atoms, respectively. The frequency difference between these two modes $\Delta k \sim 19 \text{ cm}^{-1}$, indicating the number of MoS₂ layers matching well with reported CVD-synthesized monolayer MoS₂¹⁸. The as-grown monolayer MoS₂ triangles show a strong photoluminescence (PL) peak (Fig. 3-4g) at 1.88 eV, which is close to the direct band gap of freestanding exfoliated single layer MoS₂ (1.90 eV).¹⁹ The full width at half-maximum (FWHM) of the PL peak is $\sim 65 \text{ meV}$, which is also close to freestanding exfoliated MoS₂ (50-60 meV)²⁰. These results indicate the high quality of as synthesized MoS₂ monolayer triangles.

3.3.3 Case III: Thin film growth

The substrate is placed facing up next to the MoO₃ source. After deposition, we can observe a uniform color change on the whole substrate (Fig. 3-5b), indicating a uniform planar thin film growth (Fig. 3-5c and schematic image in Fig. 3-5e) on the substrate. The numerical simulations (Fig. 3-5d) for concentration of Mo precursor and flow around the substrate indicates smaller concentration along the substrate compared to the setup for growth of planar triangular MoS₂ (Fig. 3-4) and almost no concentration gradient normal to substrate. The dark-field TEM (DF-TEM) image in Fig. 3-5f shows that the average grain size is $\sim 50 \text{ nm}$. There are small portions of MoS₂ monolayer grains merging with each other which can be observed in the fringes in DF-TEM image. It illustrates the spatial homogeneity and continuity of the as-synthesized MoS₂ film. Figure 3-5g shows the selected area diffraction pattern of as-grown MoS₂ monolayer film with [002] zone axis. The polycrystalline nature of the film is clearly identified by the diffraction rings and the corresponding d spacing is associated with the (100), (110) and (200) planes.²

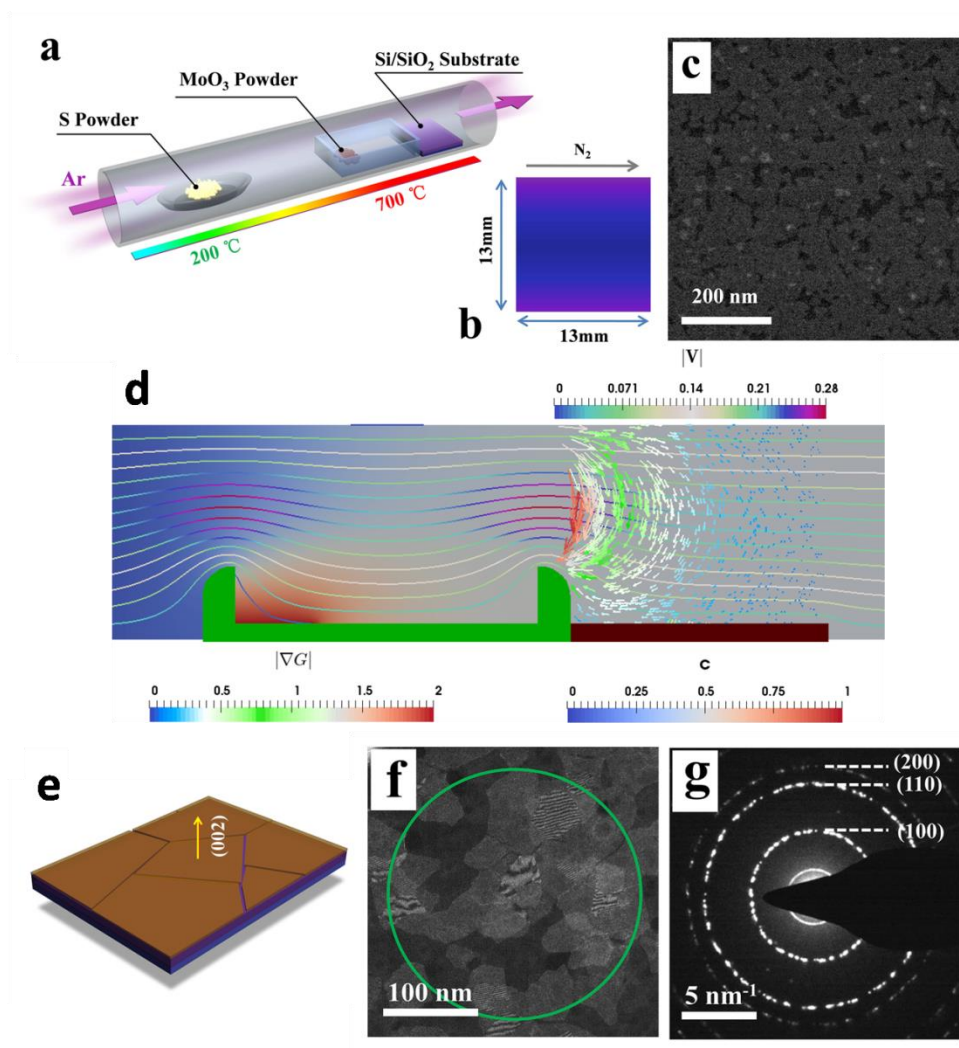


Figure 3-5. Growth of horizontal MoS_2 thin film on Si/SiO_2 substrate that is facing up downstream of the MoO_3 source. (a) Schematic illustration of the PVT system; (b) Schematic pattern of monolayer film deposition of MoS_2 on Si/SiO_2 substrate after growth; (c) Top-view SEM images of as-grown MoS_2 monolayer film; (d) Numerical simulation shows concentration of Mo precursor (background color), its gradient above the substrate (arrows), and carrier gas velocity stream (solid lines); (e) Schematic illustration for horizontal growth of MoS_2 monolayer film; (f) DF-TEM images of as-grown MoS_2 monolayer film, it clearly shows that the grain size is ~ 50 nm; (g) The selected area diffraction pattern of as-grown MoS_2 sheets from the green circle in f.

The formation of MoS_2 planar thin film is also dependent on the change of the precursor flow rate, a set of experiments for the same configuration is performed as shown in Case III with the flow rate of carrier gas (Nitrogen) changing from 50sccm, 200 sccm to 400sccm. When the flow rate is

low (the SEM image in Fig. 3-6a), the lateral growth of the TMD nuclei will be limited since the precursor supply is not sufficient. As the flow rate increases, it can increase the precursor supply. When the flow rate increases, the first layer is fully formed by Frank-van der Merve growth mechanism (Fig. 3-6b), and further growth is followed by a layer-by-layer growth mode. By further increase in the flow rate, we believe the growth mechanism transforms from planar thin film to vertical growth is by Stranski-Krastanov growth mode with MoS_2 small islands on top of the underlying films tend to vertical growth (Fig. 3-6c) This transformation is believed to be due to the changes in the interfacial energy between the film and vapor during growth by strain.

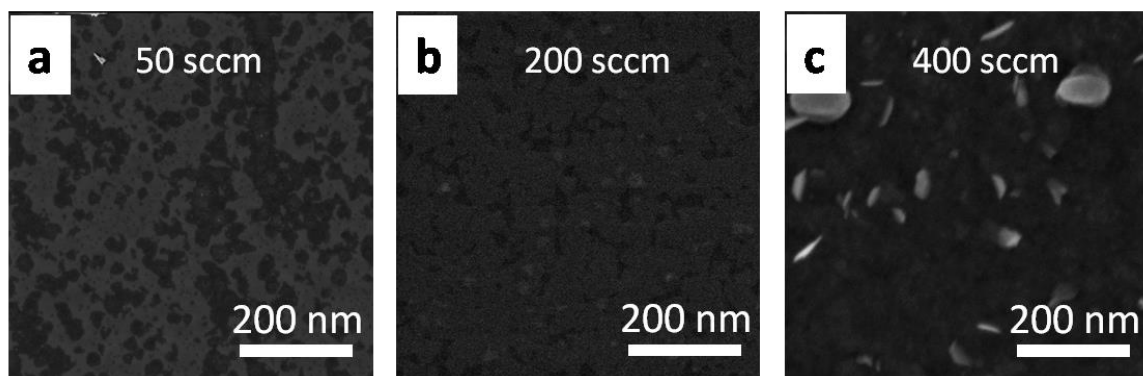


Figure 3-6. SEM images (a) 50 sccm and (b) 200 sccm of the carrier gas showing planar growth, and (c) 400 sccm of the carrier gas showing vertical growth of MoS_2 . A growth transformation from planar thin film to vertical growth with increasing carrier gas flow rate.

3.4 Growth Mechanism of 2D MoS_2 crystals

The 2D MoS_2 can grow either in type-I (vertical, Fig. 3-7a) and type-II (horizontal, Fig. 3-7b) texture,²¹ considering its crystallographic nature. Vertically grown MoS_2 fins are standing upright on the substrate by exposing their edge sites, while horizontal growth of MoS_2 displays their basal planes parallel to the substrate and may either form isolated islands or polycrystalline thin films. Our theoretical and experimental observations indicate a kinetically-driven growth mechanism,

where the growth mode (vertical vs horizontal) is determined by the concentration gradient of the precursor at the substrate, while the density of as-grown 2D TMDs is controlled by local flow rate.

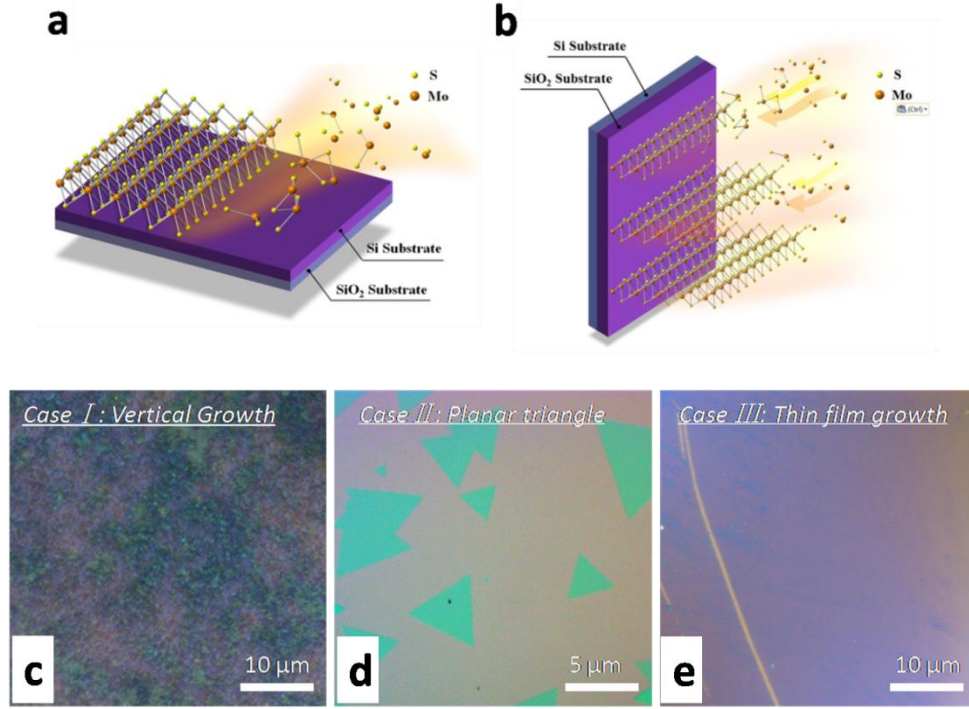


Figure 3-7. Schematic images of 2D MoS₂ crystals (a) type-I (vertical) and (b) type-II (horizontal) texture; (c)-(e) Optical images of PVT-grown 2D MoS₂ crystals.

During our experiments we changed the position of substrate (Figs. 3-2, 3-4 and 3-5), while keeping the same other growth conditions, temperature, concentration of precursors, flow rate, and growth time. The temperatures of the sulfur source, substrate, and MoO₃ source are controlled and kept constant. The temperature of the sulfur source was ~230°C, while in the hot-zone area Mo precursor and substrate was maintained at a temperature of 700°C. The temperature profile of the furnace obtained from experimental measurements (Fig. 3-1) indicates that the temperature gradient over the substrate is negligible, which also matches with the numerical simulations. Proper partial pressure ratio Mo to S (P_{Mo}/P_S) is crucial to create a desirable sulfurizing environment considering the phase diagram of the Mo–O–S system²². P_{Mo}/P_S can affect the edge energy of as-synthesized

MoS_2 and also dictates the conversion of MoO_3 to suboxides,^{23,24} which leads to the inhibition of MoS_2 growth or formation of sp^3 -bonded clusters. Because of the long distance between the S source and substrate, as well as a small flow pressure gradient across the quartz tube, the sulfur vapor gradient on the substrate is negligible. In contrast, positioning the substrate in close vicinity of the MoO_3 source crucible, implies a large gradient in the P_{Mo} (equivalent to ∇c) which is in accordance with numerical simulations in Fig. 3-8.

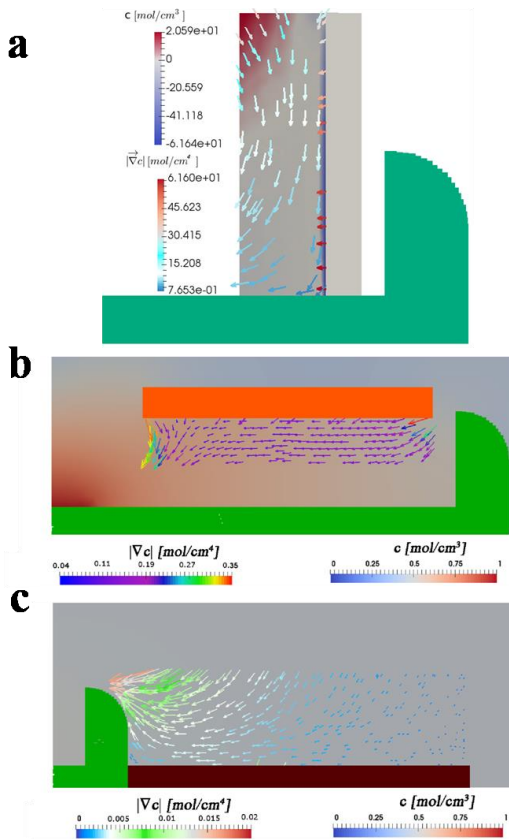


Figure 3-8. Effect of Mo precursor concentration and its distribution in vicinity of the substrate on the growth mode. (a) Concentration gradient (background color) is plotted and direction of the gradient, i.e. is shown by the arrows, where the arrows are that are colored with the scale of $|\nabla c|$ for Case I. Large concentration gradient normal to the substrate is found, which describes the growth of vertical Mo nanofins. Concentration of Mo precursor (background color) and its gradient (arrows) are higher for Case II (b) compared to Case III (c) in the vicinity of the substrate. Although direction of gradient is along the substrate in both cases, lower concentration gradient in Case III (c) leads to the formation of uniform monolayer multigrain films, in contrast to isolated MoS_2 islands in Case II (b).

Experimental observation of vertical growth of 2D MoS₂, Case I, is shown in Fig. 1. Numerical simulations of CVD growth (Fig. 3-2d and Fig. 3-8a) reveal an obvious concentration gradient of the Mo precursor normal to the substrate. It is worth noting that the arrows are pointing to the direction along which concentration of precursor increases that is opposite to the direction of diffusive flux. At the beginning of the growth, nucleus of an MoS₂ flake is formed on the substrate resulting in a concentration gradient between the top and bottom of the nucleus. A higher concentration on the top of the nucleus results in a self-amplifying concentration gradient that provides a driving force for the growth of MoS₂ normal to the substrate, ie. the Mullins-Sekerka instability and growth¹¹ (similar to the concentration gradient leading to dendrite growth).

Changes in the interface energy also plays a crucial role during the growth of 2D nanomaterials. Here the substrate/vapor interface will be substituted by substrate/MoS₂ interface and vapor/MoS₂ interface, which itself is a function of precursor concentration. For vertical growth of MoS₂ fins, more vapor/MoS₂ interface and edge sites are created rather than the substrate/vapor interface, which means the change in interface energy should be positive (Volmer-Weber growth mechanism). Besides the main effect introduced by precursor concentration and its gradient, carrier gas flow rate also has a non-trivial effect on the final morphology. For each case, we fixed the N₂ flow rate at 200 sccm for Mass Flow Controller. Numerical simulations demonstrate the flow rate at different sections of the PVT furnace (specified by density of stream lines and their coloring in the Figs. 3-2, 3-4 and 3-5). For the standing substrate, as illustrated in Fig. 3-2d and Fig. 3-8a, there is an increase in the local flow rate where the substrate is located. This increase can be seen in the background color of the schematic showing a decrease in the concentration as we move from the top to the bottom of the substrate surface. The role of kinetics will be enhanced under high flow rates, where higher mass transfer leads to a faster crystal growth rate.¹¹ This describes our

experimental observations in Fig. 3-2b-c, with the top side of the vertical substrate with higher flow rate showing denser vertical MoS₂ fins as opposed to the bottom.

For planar monolayer triangle growth in Case II, numerical simulations (Fig. 3-4d and Fig. 3-8b) display negligible concentration gradient normal to the substrate. As we mentioned above, the change in the interface energy is a function of precursor concentration (P_{Mo} and P_S) which is not positive considering the monolayer structure of the as grown triangles (Frank-van der Merve growth mechanism). If the change in interface energy was positive, we would have seen multilayers instead of a monolayer MoS₂ (Volmer–Weber growth mechanism). Thus the flakes tend to spread laterally, forming planar single layer triangles with a crystallography direction of (002) to minimize the overall surface energy. The traditional sulfurization of metal or metal compounds during the CVD process for an upside down substrate setup only leads to the formation of triangular-shaped MoS₂²³ that is similar to Case II. The numerical simulation of the growth process for Case II (Fig. 3-4d and Fig. 3-8b) indicate that moving from area (i) to area (ii) on the substrate, concentration of the precursor, c , and magnitude of its gradient, $|\vec{\nabla}c|$, reduce. The lesser concentration, c , results in fewer nucleation sites and the smaller $|\vec{\nabla}c|$, results in lower thermodynamic driving force, which subsequently is in effect of fewer supercritical nuclei. In area (i) the many supercritical MoS₂ triangles formed, start to grow, depleting the MoS₂ concentration in the surrounding gas phase, which further limits the growth of MoS₂ triangles. In contrast, there are fewer supercritical MoS₂ triangles in the area (ii) and thus depletion of MoS₂ in the gas phase is not a limiting factor. This justifies the fewer yet larger MoS₂ triangles that are forming in the area (ii) compared to the area (i).

For the configuration where the substrate is laying down next to the crucible (Case III), the concentration of the Mo precursor is lower than Case II and only a small gradient exists along the substrate (Fig. 3-5d and Fig. 3-8c). Comparing to Case II, it is obvious that P_{Mo} is lowered and thus the P_{Mo}/P_S is relatively small. Comparing Fig. 3-4c and 3-5c, the size of the triangular-shaped MoS₂ monolayers grown in Case II are in the order of a few microns while the size of individual grains in the monolayer thin film grown in Case III is of a few tens of nanometers. This indicates a smaller number of nucleation sites in Case II compared to Case III, which may be interpreted by the higher energy of the critical nucleus at the growth conditions of Case II compared to Case III. In this case, more detailed analysis needs to be performed using *ab initio* calculations to find the energy change during the formation of MoS₂ nuclei as a function of P_{Mo}/P_S .²⁵ Simulation results presented for Case III (Fig. 3-5d and 3-8c) indicate the velocity of carrier gas flow over the substrate is larger in Case III compared to Case II, which is in effect of greater mass flow toward the substrate and higher nucleation rate in Case III. However, a smaller concentration of precursor and its gradient, c and $|\vec{\nabla}c|$, in the vicinity of the substrate is revealed in Case III compared to Case II, which lower the thermodynamic driving force for the nucleation and growth of layered MoS₂ nanostructures. Thus, in the Case III, although there are larger number of nuclei, the thermodynamic driving force for their growth is smaller compared to Case II. This results in a larger number of small monolayer MoS₂ grains that are grown to cover surface of the substrate, forming an atomic thin multi-grain film of MoS₂ (Fig. 3-5f), where the size of each individual grain is smaller than the size of individual MoS₂ triangles shown in Fig. 3-4c for Case II. Different grain shapes are observed in Case III due to the complex nature of interactions between different grains and the kinetics of growth. The setup presented in Case III is preferred to maximize the overall coverage of the monolayer by facilitating the lateral expansion of the flakes. It is thus critical to

maintain a low and constant P_{Mo} , as well as the proper carrier gas flow rate over the substrate to obtain a uniform monolayer thin film.

3.5 Chapter Summary

Using a combined experimental and numerical approach, we studied the key parameters for the planar and vertical growth of 2D materials and demonstrated the possibility for engineering their morphology by controlling the concentration and flow profiles. The results presented here revealed a new controlling factor, concentration gradient, which can shift the growth of 2D TMDs from the planar to the vertical direction. This study further demonstrates that the density of as-grown nanostructures can also be controlled by the precursor flow rate during synthesis. This provides anew mechanism for controllable growth of 2D MoS₂ with different orientations and morphologies for applications in energy, catalysis, electronic devices and ultrathin integrated circuits.

3.6 References

1. Lukowski, M. A.; Daniel, A. S.; Meng, F.; Forticaux, A.; Li, L.; Jin, S., Enhanced hydrogen evolution catalysis from chemically exfoliated metallic MoS₂ nanosheets. *Journal of the American Chemical Society* **2013**, *135* (28), 10274-10277.
2. Liu, K.-K.; Zhang, W.; Lee, Y.-H.; Lin, Y.-C.; Chang, M.-T.; Su, C.-Y.; Chang, C.-S.; Li, H.; Shi, Y.; Zhang, H., Growth of large-area and highly crystalline MoS₂ thin layers on insulating substrates. *Nano letters* **2012**, *12* (3), 1538-1544.
3. Zhan, Y.; Liu, Z.; Najmaei, S.; Ajayan, P. M.; Lou, J., Large-area vapor-phase growth and characterization of MoS₂ atomic layers on a SiO₂ substrate. *Small* **2012**, *8* (7), 966-971.
4. Lee, Y. H.; Zhang, X. Q.; Zhang, W.; Chang, M. T.; Lin, C. T.; Chang, K. D.; Yu, Y. C.;

Wang, J. T. W.; Chang, C. S.; Li, L. J., Synthesis of Large-Area MoS₂ Atomic Layers with Chemical Vapor Deposition. *Advanced Materials* **2012**, *24* (17), 2320-2325.

5. Bosi, M., Growth and synthesis of mono and few-layers transition metal dichalcogenides by vapour techniques: a review. *RSC Advances* **2015**, *5* (92), 75500-75518.

6. Yin, Z.; Li, H.; Li, H.; Jiang, L.; Shi, Y.; Sun, Y.; Lu, G.; Zhang, Q.; Chen, X.; Zhang, H., Single-layer MoS₂ phototransistors. *ACS nano* **2011**, *6* (1), 74-80.

7. Kim, S.; Konar, A.; Hwang, W.-S.; Lee, J. H.; Lee, J.; Yang, J.; Jung, C.; Kim, H.; Yoo, J.-B.; Choi, J.-Y., High-mobility and low-power thin-film transistors based on multilayer MoS₂ crystals. *Nature communications* **2012**, *3*, 1011.

8. Radisavljevic, B.; Radenovic, A.; Brivio, J.; Giacometti, V.; Kis, A., Single-layer MoS₂ transistors. *Nature nanotechnology* **2011**, *6* (3), 147-150.

9. Podzorov, V.; Gershenson, M.; Kloc, C.; Zeis, R.; Bucher, E., High-mobility field-effect transistors based on transition metal dichalcogenides. *Applied Physics Letters* **2004**, *84* (17), 3301-3303.

10. Kong, D.; Wang, H.; Cha, J. J.; Pasta, M.; Koski, K. J.; Yao, J.; Cui, Y., Synthesis of MoS₂ and MoSe₂ films with vertically aligned layers. *Nano letters* **2013**, *13* (3), 1341-1347.

11. Li, H.; Wu, H.; Yuan, S.; Qian, H., Synthesis and characterization of vertically standing MoS₂ nanosheets. *Scientific reports* **2016**, *6*.

12. Wang, H.; Lu, Z.; Xu, S.; Kong, D.; Cha, J. J.; Zheng, G.; Hsu, P.-C.; Yan, K.; Bradshaw, D.; Prinz, F. B., Electrochemical tuning of vertically aligned MoS₂ nanofilms and its application in improving hydrogen evolution reaction. *Proceedings of the National Academy of Sciences* **2013**, *110* (49), 19701-19706.

13. Yu, Y.; Huang, S.-Y.; Li, Y.; Steinmann, S. N.; Yang, W.; Cao, L., Layer-dependent electrocatalysis of MoS₂ for hydrogen evolution. *Nano letters* **2014**, *14* (2), 553-558.

14. Kang, K.; Xie, S.; Huang, L.; Han, Y.; Huang, P. Y.; Mak, K. F.; Kim, C.-J.; Muller, D.;

Park, J., High-mobility three-atom-thick semiconducting films with wafer-scale homogeneity. *Nature* **2015**, 520 (7549), 656-660.

15. Lin, Y.-C.; Zhang, W.; Huang, J.-K.; Liu, K.-K.; Lee, Y.-H.; Liang, C.-T.; Chu, C.-W.; Li, L.-J., Wafer-scale MoS₂ thin layers prepared by MoO₃ sulfurization. *Nanoscale* **2012**, 4 (20), 6637-6641.

16. Jung, Y.; Shen, J.; Liu, Y.; Woods, J. M.; Sun, Y.; Cha, J. J., Metal seed layer thickness-induced transition from vertical to horizontal growth of MoS₂ and WS₂. *Nano letters* **2014**, 14 (12), 6842-6849.

17. Comsol, *COMSOL Multiphysics: Version 3.3*. Comsol: 2006.

18. Lee, C.; Yan, H.; Brus, L. E.; Heinz, T. F.; Hone, J.; Ryu, S., Anomalous lattice vibrations of single-and few-layer MoS₂. *ACS nano* **2010**, 4 (5), 2695-2700.

19. Splendiani, A.; Sun, L.; Zhang, Y.; Li, T.; Kim, J.; Chim, C.-Y.; Galli, G.; Wang, F., Emerging photoluminescence in monolayer MoS₂. *Nano letters* **2010**, 10 (4), 1271-1275.

20. Mak, K. F.; Lee, C.; Hone, J.; Shan, J.; Heinz, T. F., Atomically thin MoS₂: a new direct-gap semiconductor. *Physical Review Letters* **2010**, 105 (13), 136805.

21. Galun, E.; Cohen, H.; Margulis, L.; Vilan, A.; Tsirlina, T.; Hodes, G.; Tenne, R.; Hershfinkel, M.; Jaegermann, W.; Ellmer, K., Crystallization of layered metal-dichalcogenides films on amorphous substrates. *Applied physics letters* **1995**, 67 (23), 3474-3476.

22. Feldman, Y.; Wasserman, E.; Srolovitz, D.; Tenne, R., High-rate, gas-phase growth of MoS₂ nested inorganic fullerenes and nanotubes. *Science* **1995**, 267 (5195), 222-225.

23. Wang, S.; Rong, Y.; Fan, Y.; Pacios, M.; Bhaskaran, H.; He, K.; Warner, J. H., Shape evolution of monolayer MoS₂ crystals grown by chemical vapor deposition. *Chemistry of Materials* **2014**, 26 (22), 6371-6379.

24. Shang, S.-L.; Lindwall, G.; Wang, Y.; Redwing, J. M.; Anderson, T.; Liu, Z.-K., Lateral Versus Vertical Growth of Two-Dimensional Layered Transition-Metal Dichalcogenides:

Thermodynamic Insight into MoS₂. *Nano Letters* **2016**.

25. Cao, D.; Shen, T.; Liang, P.; Chen, X.; Shu, H., Role of Chemical Potential in Flake Shape and Edge Properties of Monolayer MoS₂. *The Journal of Physical Chemistry C* **2015**, *119* (8), 4294-4301.

Chapter 4

Effect of Substrate Defects on the van der Waals Epitaxy of MoS₂/hBN heterostructure

4.1 Introduction and Motivation

Layered transitional-metal dichalcogenide (TMD)-based vertically stacked van der Waals (vdW) heterostructures are intriguing candidates for electronic^{1 2 3 4}, optoelectronic⁵ and photonic devices^{6 7}, opening up pathways to generate novel functionalities of materials via a bottom-up approach^{8 9}. Previous works^{10 11 12 13 14} have reported TMD/hBN heterostructures synthesized by CVD process, but little is known about the interfacial structure and the nucleation and growth mechanism of the heterostructure. Therefore a clear and straightforward understanding of the nucleation and growth of vdW heterostructure, and the role of substrate defects at the interface is necessary to modify the interfacial structure and further tune its macroscale properties.

Here in this chapter, both mechanical exfoliated hBN (ME-hBN) and CVD-hBN is used as a template to fabricate MoS₂/hBN vdW heterostructures using the powder vapor transport (PVT) process. Atomic resolution aberration-corrected (AC-) S/TEM imaging and spectroscopy techniques are used to investigate the atomic, chemical, and electronic structure of the TMDs/hBN heterostructures. in this study we further determine the nucleation and growth of epitaxial MoS₂/hBN vdW heterostructures as a function of hBN substrate defects. Probing hBN substrate defects by ultra-high resolution TEM further uncovers the crucial effect of surface defects on the nucleation of TMDs, the resulting epitaxy, the domain size and orientation, and the layer thickness of TMDs/hBN heterostructure.

4.2 Results and discussion

4.2.1 Simultaneous growth of MoS₂ domains on hBN and Si/SiO₂ substrate

Fabrication process of MoS₂/hBN vdW heterostructures, both freestanding and on Si/SiO₂ substrate, is schematically displayed in Fig. 4-1a via PVT. The substrates for growing MoS₂ nanosheets are mechanical exfoliated (ME-) hBN (hBN powder with grade PT 110 by Momenive Performance Materials) on top of Si/SiO₂ substrate and Au quantifoil TEM grid. Freestanding ME-hBN template is transferred onto TEM grid by PMMA method to serve as the growth template. Combination of mechanical exfoliation and transfer methods for achieving freestanding hBN films enable the good quality of hBN surface before any treatments, hBN surface can also survive at high temperature (700 °C) annealing in the reaction furnace in terms of superior thermal stability. After the growth in CVD furnace, epitaxial MoS₂ triangles on suspended ME-hBN is schematically illustrated in Fig. 4-1b.

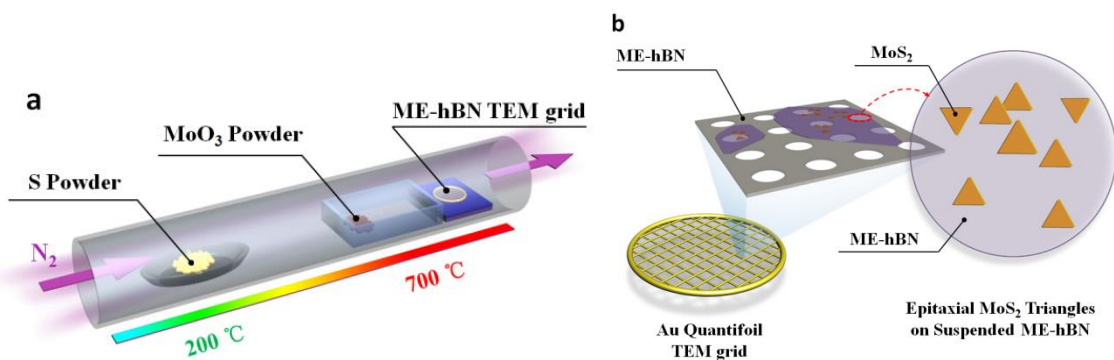


Figure 4-1. (a) Schematic of CVD system setup; (b) Geometry of the substrate (ME-hBN covered TEM grid), schematic illustration for freestanding MoS₂/ME-hBN heterostructure

Figure 4-2a and b presents the SEM image of MoS₂/hBN vdW heterostructures on Si/SiO₂ substrate. It is obvious that the as-grown MoS₂ domains (dark contrast) are single crystal triangular flakes with sharp-edges. Also a strict crystallographic relationship is observed between MoS₂

triangles (with the size $\sim 300\text{nm}$) and the underlying hBN flakes. In addition, outside of the hBN flake, MoS₂ domains are observed to have directly grown on Si/SiO₂, with more disorder due to the poor crystallinity of underlying SiO₂ substrate.

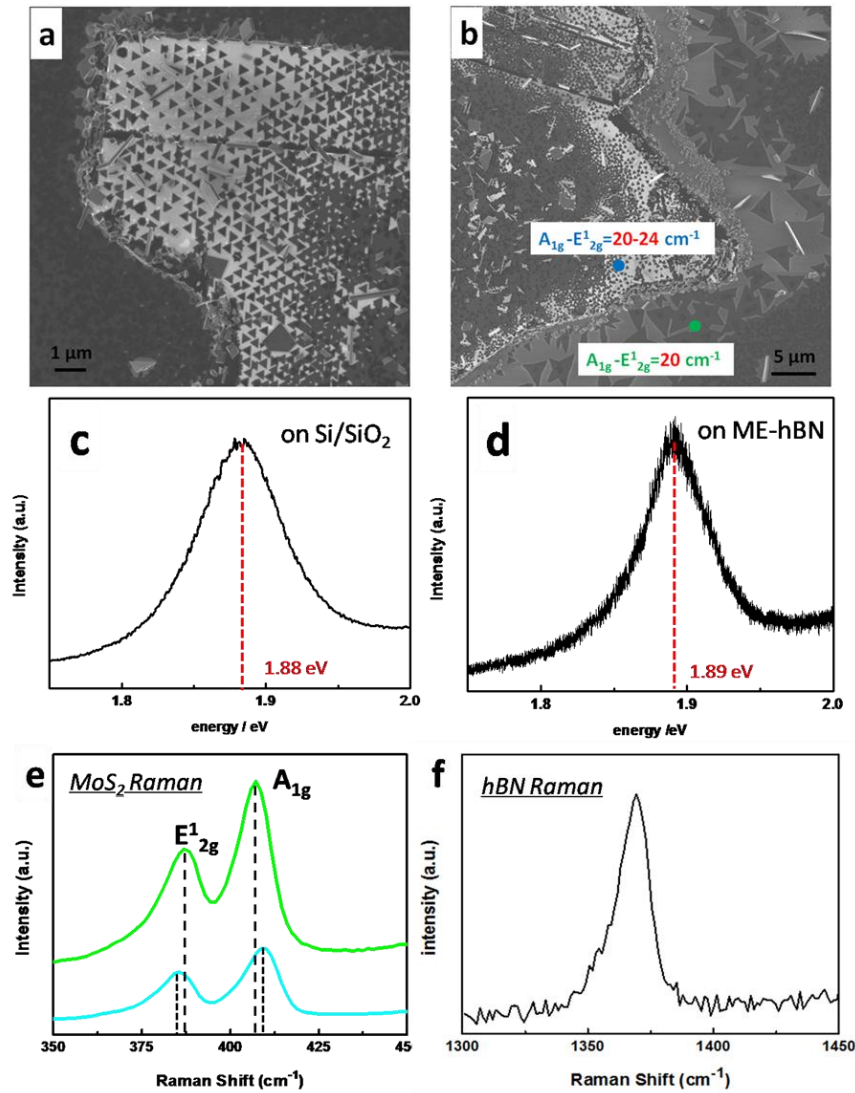


Figure 4-2. (a) and (b) SEM image of MoS₂ triangular grains epitaxially grown on ME-hBN and on Si/SiO₂ substrate and orientated at 180° with respect to each other; (c) and (d) PL measurement of the as-grown monolayer MoS₂ regions on top of hBN and on top of Si/SiO₂ substrate, respectively; (e) and (f) Raman spectrum of the as-grown monolayer MoS₂ triangular domain and hBN flake, respectively

Raman spectra shown in Fig. 4-2e and f index two characteristic peaks (E_{2g}^1 mode and A_{1g} mode) correlated to the in- and out-of-plane vibrations of molybdenum and sulfur atoms, respectively. A Raman shift near 1370 cm^{-1} is being identified as the fingerprint of hBN. The frequency difference Δk between A_{1g} and E_{2g}^1 varies from 19 to 24 cm^{-1} throughout the MoS_2/hBN heterostructure, indicating that the as-grown MoS_2 grains belong to monolayer to few layers as previously reported for the CVD-synthesized MoS_2 crystals.¹⁵ It also can be observed from the image contrast in SEM image Fig. 4-2a that there are some secondary layers on top of MoS_2 triangular grains. For the MoS_2 domains directly grown on Si/SiO_2 , the difference of Raman shifts are consistently 19 cm^{-1} throughout the substrate (previously discussed in Chapter 3 for this film growth). The as-grown monolayer MoS_2 regions on top of hBN show an intensive photoluminescence (PL) peak (Fig. 4-2d) at 1.89 eV , which is close to the direct band gap of freestanding exfoliated monolayer MoS_2 (1.90 eV).¹⁶ The full width at half-maximum (FWHM) of the PL peak is $\sim 50\text{ meV}$ similar to freestanding exfoliated MoS_2 ($50\text{--}60\text{ meV}$)¹⁷, while for MoS_2 directly grown on Si/SiO_2 , the PL peak is indexed at 1.88 eV and the FWHM is $\sim 70\text{ meV}$. These results indicate the high crystallinity of as-synthesized MoS_2 grains with strong interfacial contact and improved optical response when MoS_2 is placed on top of hBN. This observation indicates that hBN as a substrate can perfectly mimic the characteristics of freestanding TMDs and is an excellent substrate for 2D semiconductors when determining their intrinsic properties.

4.2.2 TEM imaging and spectroscopy of the freestanding MoS_2/hBN heterostructures

TEM imaging and spectroscopy are used to examine the atomic structure and chemistry of the freestanding MoS_2/hBN heterostructures. The as-grown MoS_2 triangles on hBN can be seen as dark triangles due to diffraction contrast mechanism in TEM imaging in Fig. 4-3a, in accordance to the morphology shown in SEM image (Fig. 4-2a). Selected area electron diffraction (SAED) pattern

shown in Fig. 4-3b corresponds to the red circled area in Fig. 4-3a, these two sets of aligned hexagonal patterns with no misorientation strongly confirm that there exists a strict crystallographic relationship between MoS₂ triangles and suspended hBN flakes. This epitaxial relationship arises from the weak vdWs interaction between hBN and MoS₂ with no dangling bonds at the interface.

^{18 19} The annular dark field (ADF)-STEM image in Fig. 4-3c indicates that the as-grown MoS₂ triangles on hBN are monolayer to few layers in thickness with a lateral size of around 200 nm, and opposite arrangement (180°) with respect to each other grown on top of ME-hBN. Most of the MoS₂ domains are multilayers but at the edge of the triangular domains, subsequent layers are observed also epitaxially oriented. It is worth noting that at the step edge of the hBN surface, where more dangling bonds are expected, the locally as-grown MoS₂ domains have random orientations (Fig. 4-3d).

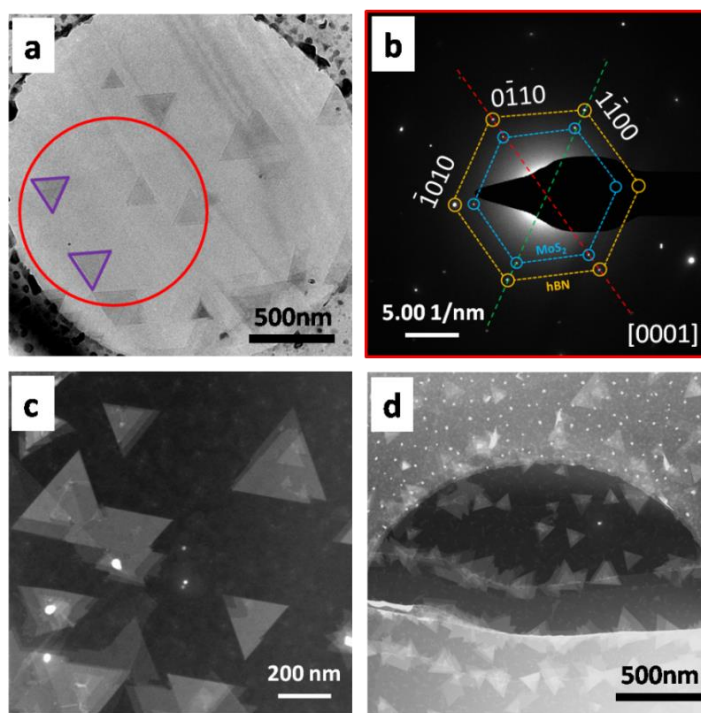


Figure 4-3. (a) TEM image of triangular-shaped MoS₂ grown on a freestanding ME-hBN flake, (b) SAED pattern from the red-circled MoS₂/hBN, yellow shows hBN pattern, blue shows MoS₂ pattern, there is an exact 0 degree orientation relationship between the interface of epitaxial MoS₂ and underlying ME-hBN templates; (c) ADF-STEM image of triangular-shaped MoS₂ grown on a

freestanding ME-hBN flake, sequent layers of MoS₂ can be visualized by different contrast; (d) ADF-STEM image of triangular-shaped MoS₂ grown on the hBN flake step edges.

Electron energy loss spectroscopy (EELS) is performed on hBN surface indexing the boron edge and nitrogen edge (shown in Fig. 4-4a), there are two characteristic peaks both shown in boron edge and nitrogen edge which correlate with in-plane σ^* sp² bonds and interlayer π^* vdW bonds. This clarifies that the underlying hBN is hexagonal honeycomb crystal structure. STEM Energy-dispersive X-ray spectroscopy (EDS) mapping (shown in Fig. 4-4 b-e) identify the chemical fingerprint of the as-grown heterostructure. Figure 4-4c-e shows EDS elemental maps for nitrogen, sulfur and molybdenum respectively, indicating a uniform coverage of N in the hBN template, S and Mo distributed evenly within the triangular domain.

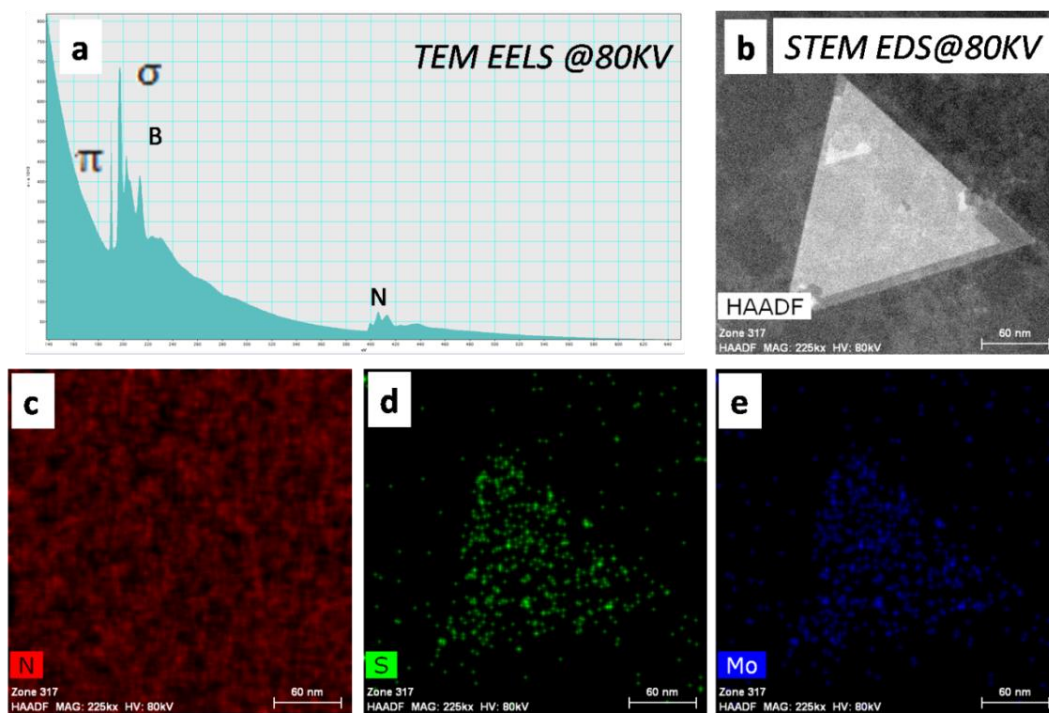


Figure 4-4. (a) Core loss EEL spectrum of the MoS₂/hBN heterostructures, the boron edge and nitrogen edge are indexed; (b-e) EDS mapping of the MoS₂/hBN heterostructures, elemental nitrogen, sulfur and molybdenum mapping, respectively

4.2.3 Effect of plasma-induced substrate defects on the epitaxy of heterostructures

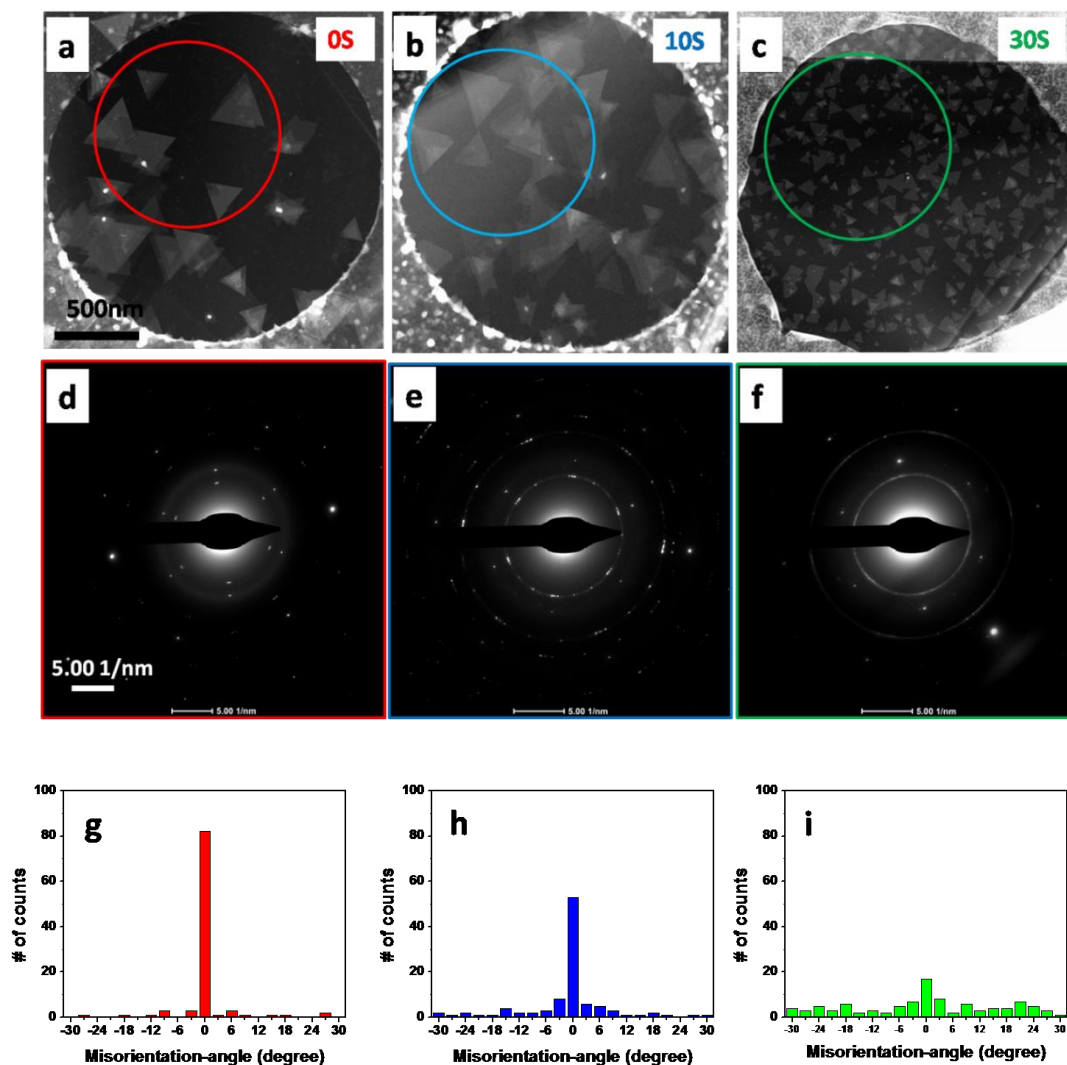


Figure 4-5. Effect of different reactive ion etching time (0 seconds, 10 seconds and 30 seconds, respectively) on the resulting epitaxy, domain size and substrate coverage of the as-grown heterostructure. (a-c) ADF-STEM images of as-grown heterostructure, the resulting epitaxy is also been examined by diffraction analyses in (d-f); (g-i) Quantitative analysis of misorientation angle between MoS₂ triangles and the underlying hBN substrate, indicating the degree of epitaxy.

Surface defects, dangling bonds at grain boundaries and step edges, are more reactive, thus favor nucleation of MoS₂ to a higher density²⁰. Here, we use reactive ion etching as an approach to intentionally induce surface defects on hBN, which significantly affects the nucleation and growth

of heterostructure. Different reactive ion etching times (0 seconds, 10 seconds and 30 seconds, respectively) are applied on suspended hBN surfaces while fixing other plasma generation parameters (50 sccm oxygen gas is introduced in chamber, total flow rate is 200 mTorr, RF power is 50 Watts). During the bombardment by reactive oxygen ions, atoms on the surface of hBN sputter away the surface atoms and leave localized vacancy defects, resulting in extensive surface defects. Three hBN templates with different plasma etching times are used as the substrates to grow MoS₂/hBN heterostructures at the exact same conditions. ADF-STEM images (Fig. 4-5a-c)) indicate that as the etching time increases, MoS₂ triangular domains are more randomly dispersed on hBN surface and loss of epitaxy is observed. The resulting epitaxy is quantitatively assessed by diffraction analysis displayed in Fig. 4-5d-f. Orientation analyses are performed on 100 MoS₂ triangles on the three heterostructures to statistically determine the misoriented angles between the MoS₂ and hBN lattices (Fig. 4-5g-i). The degree of epitaxy tends to decrease as the etching time increases (curve in Fig. 4-6a). Also the average sizes of monocrystalline triangular MoS₂ domains and hBN substrate coverages are calculated respectively as the etching time increases (Fig. 4-6c and d). The size of as-synthesized triangular MoS₂ domain decreases while the hBN substrate coverage increases accordingly. These observed results clearly illustrate that as the reactive etching time increases, more surface defects and dangling bonds are generated as active nucleation sites for the growth of MoS₂ domains. This observation strongly suggests the role of defects and dangling bonds on the resulting epitaxy, domain size and layer thickness of the as-grown heterostructures. Interestingly, there is also a transition from few layer to monolayer MoS₂ domains on hBN with increasing the plasma treatment time (Fig. 4-5a-c). Synthesis of monolayer MoS₂ domains through surface defects can be considered a way to create uniform monolayer MoS₂ film. It is well known that bulk MoS₂ crystal is an indirect-band gap semiconductor (~ 1.3 eV), while monolayer MoS₂ shows a direct-bandgap of ~ 1.9 eV. An expected dramatic optical response would attribute to this indirect-to-direct band transition since the monolayer MoS₂ exhibit a higher luminescence quantum

efficiency compared to its bulk counterpart.¹⁷ This approach opens a new door to nano-engineering the electronic and optical properties of vdW heterostructures by means of interface defects modification.

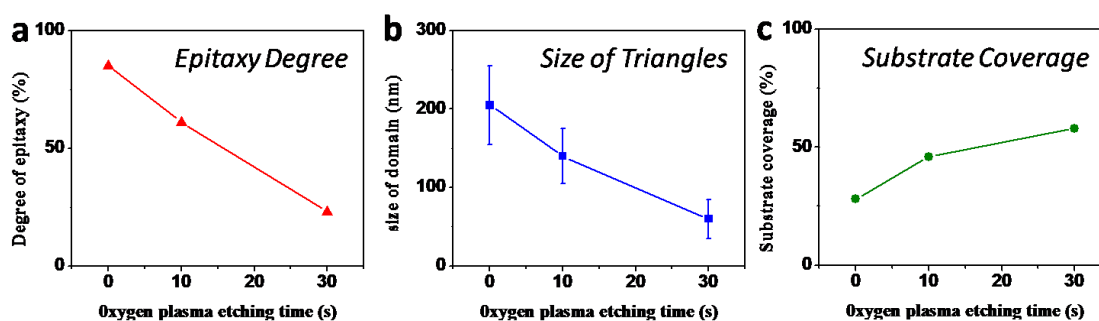


Figure 4-6. Statistical analysis of (a) Resulting epitaxy; (b) Domain size and (c) Substrate coverage of the as-grown heterostructure.

4.2.4 Atom-by-atom identification of defective hBN

To further understand the loss of epitaxy with increasing surface plasma treatment time, we further examine the surface of hBN at the atomic size scale using ultra-high resolution TEM with a low yet sufficient electron dose that can minimize the structural damage during imaging. AC-HREM imaging was realized by FEI Titan 60-300 microscope at 80kV beam energy with a monochromated beam and spherical aberration correction, providing sub-angstrom spatial resolution. Using a negative Cs value, the imaging condition is tuned to provide bright atom contrast with a slight overfocus. We imaged the three different hBN substrates on the flakes where MoS₂ was grown with a reduced dose imaging condition. Since the imaged hBN structure was near the MoS₂ triangles, it is expected that the same defect configuration is responsible for the nucleation and growth of MoS₂.

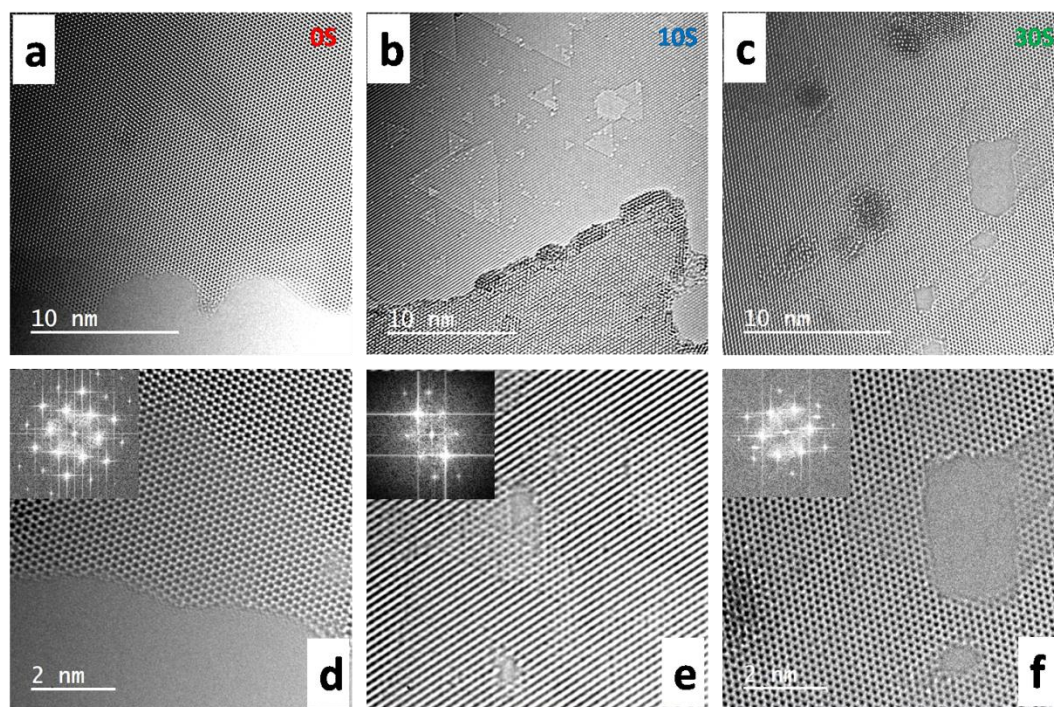


Figure 4-7. Atomic resolution TEM images of hBN surface with different reactive ion etching time (0 seconds, 10 seconds and 30 seconds, respectively). (a, d) 0 seconds plasma etching (*i.e.* no plasma treatment) hBN few layer area with an excellent surface quality free of defects and dangling bonds; (b, e) 10 seconds oxygen plasma treatment on few layer hBN area with dispersed single vacancies and oriented triangle-shaped surface defects; (c, f) 30 seconds oxygen plasma treatment on few layer hBN area with severe surface defects, trapped contaminations and particles.

Fig. 4-7a and d shows the primary features for 0 seconds plasma etching (*i.e.* no plasma treatment).

The periodic bright spots correspond to boron and nitrogen atoms (or atomic columns when more than monolayer), with an in-plane B-N bond length of 0.14 nm, in accordance with the known crystal structure of hBN.²² In this sample, no defect or vacancy is observed on the surface of hBN. However intensity variation can be observed at the step edges between different layers, indicating excellent surface qualities free of defects and dangling bonds on each terrace. This explains the phenomenon that MoS₂ triangles epitaxially grow on top of hBN surface by means of van der Waals epitaxy. Also as we have observed in ADF-STEM image shown in Fig. 4-3a, secondary MoS₂ triangular domains prefer to nucleate on top of MoS₂ triangles rather than defect-free hBN surface.

We assume the initial layer of MoS₂ nucleates at the surface defects or contamination of hBN surface which is inevitably created by sample handling process. We believe that there are three possible reasons contributing to this few layer growth: (1) The nucleation energy of MoS₂ on top of MoS₂ is smaller than that of MoS₂ on top of defect-free hBN; (2) The van der Waals forces between MoS₂ and hBN is weaker than that between MoS₂ and MoS₂. Because MoS₂ and hBN have ~28% lattice mismatch which will need relaxation through van der Waals bonding between MoS₂ and hBN; (3) Change in the interface energy also plays a crucial role during the growth of 2D nanomaterials. For MoS₂ to grow on MoS₂, the change in the interface energy is negligible since there is almost no introduction of the new interface, while the hBN/vapor interface will be substituted by hBN/MoS₂ interface and vapor/MoS₂ interface if MoS₂ grows on hBN. This means that the change in interface energy should be positive if MoS₂ grows on defect-free hBN. Positive energy formation of the growth is not energetically favorable and can result in the formation of few layer MoS₂ domains shown in Fig. 4-3a (Volmer–Weber growth mode).²³

The most striking features in Fig. 4-7b and e are related to the 10 seconds oxygen plasma treatment on few layer hBN area with single vacancies and oriented triangle-shaped surface defects. The observed single atomic vacancies are introduced into the structure by knock-on damage²⁴ through plasma etching. Prior studies report that the observed vacancies should predominately be boron vacancies because the energy threshold for knock-on damage of boron is lower than that of nitrogen (boron and nitrogen energy threshold for knock-on damage are 74 KeV and 84 KeV,²² respectively). The oriented triangle-shaped hBN surface defects are created by consistent removal of atoms next to a single vacancy with the respective layer. The resulting appearances resemble Sierpinski triangles with a minimum granularity in accordance with atomic dimensions²⁵. It is expected that dangling bonds in these defects can form bonds with the second layer and act as primary nucleation sites for MoS₂. The surface defects and dangling bonds will unavoidably

interact with the precursor and affect the resulting epitaxy of MoS₂/hBN heterostructure. Also This interaction results in smaller MoS₂ domain sizes and higher hBN surface coverage While van der Waal epitaxy has been deteriorated due to the interaction between the active dangling bonds and MoS₂ atoms. The change in interface energy should be reduced in the case of MoS₂ grow on hBN when defects and dangling bonds are involved (Frank-van der Merve growth mechanism).

As the etching time increases, hBN surface has been drastically thinned down until some holes have emerged as shown in Fig. 4-7c and f. At this point, the observed defects include single vacancies, oriented triangle-shaped surface defects, and random step edges along the hole. The edge configuration of hBN has been examined and show both armchair edges in hBN (shown in Fig. 4-8b) with alternating double-bonded B-N structures, and zig-zag edges shown in Fig. 4-8a. However zigzag edges are more frequently observed, since nitrogen-terminated zigzag edges are more stable than other edge structures in hBN due to a higher knock-on energy threshold for in plane sp²-bonded N versus B.³²

It is evident that contamination, feedstock particles and small suboxide nucleation can be easily trapped by the local holes formed by extensive surface defects. As a result, the resulting epitaxy of the as-grown MoS₂/hBN heterostructure can be severely destroyed. This interaction makes the MoS₂ domains smaller with monolayer (with a small portion 2nd layer region) features evenly dispersed on hBN template. Our experimental observations in this sample indicate that with the introduction of defects in hBN, it is preferential to form a MoS₂ domain on defective hBN surface than as-grown MoS₂ with good crystallinity.

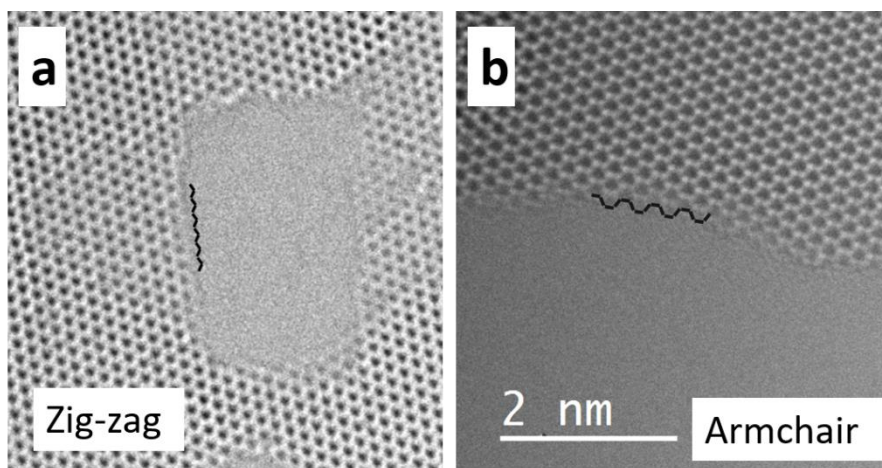


Figure 4-8. Edge structure of hBN flake. HRTEM image of (a) zig-zag edge and (b) armchair edge..

The edge configurations of hBN are examined, including the monolayer edge and holes. Compared to the armchair edges in hBN (shown in Fig. 4-8b) with alternating double-bonded B-N structures, the zig-zag edges shown in Fig. 4-8a are more frequently observed, it is proven that nitrogen-terminated zigzag edges are more stable than other form of edges in hBN monolayers due to a higher knock-on energy threshold for in plane sp^2 -bonded N versus B.³² Physical, chemical and electronic properties of hBN and other 2D materials is very sensitive to the defects configuration, the defect visualization and atom identification technique employed here provides an insightful understanding of material structure-property relationship and undoubtedly can be applied to other systems.

4.2.5 Growth of all CVD-based MoS₂/hBN heterostructures

As discussed above, TMD based heterostructures fabricated via direct mechanical transfer methods may not maintain a clean interface and lead to interfacial degradation. Controllable PVT method is utilized here to obtain MoS₂/hBN vdW heterostructure with a clean interface⁸. While the former

discussion in this chapter are all based on the fact that one crystal in the heterostructure is mechanical exfoliated (hBN) with clean and defect-free surface, this process is not scalable and reproducible. The next attempt should be the realization of the large scale chemical vapor deposition growth of MoS₂/hBN heterostructures directly applicable in large area optoelectronics such as solar cells and photodetectors. Low pressure (LP-) CVD process has been conducted in our lab as a method to synthesize thin hBN films with controlled layer thickness and morphology on copper foil. Figure 4-9a shows the SEM images of thin hBN films on Cu. The as grown hBN cannot be directly used as the growth substrates since S strongly reacts with Cu. Therefore, the film is transferred onto the TEM grid by PMMA-assisted methods (Fig 4-9b). We then utilize the same growth process as the growth of MoS₂/ME-hBN heterostructure (refer to the section here). The as-synthesized MoS₂/CVD-hBN heterostructure is able to be directly characterized by TEM. ADF-STEM images shown in Fig. 4-9c indicate non-epitaxial growth of MoS₂ domains on top of the CVD-hBN with random orientations, yet the domains are predominately monolayers and in triangular shapes. Atomic resolution ADF-STEM image in Fig. 4-9d indicates the defective nature of the as-grown MoS₂, with a non-uniform edge morphologies which indicates that the surface quality and defects of the hBN substrate can greatly tune the growth dynamics. This heterostructure morphology is similar to the MoS₂/ME-hBN heterostructure which ME-hBN is being O₂ plasma treated for 30s.

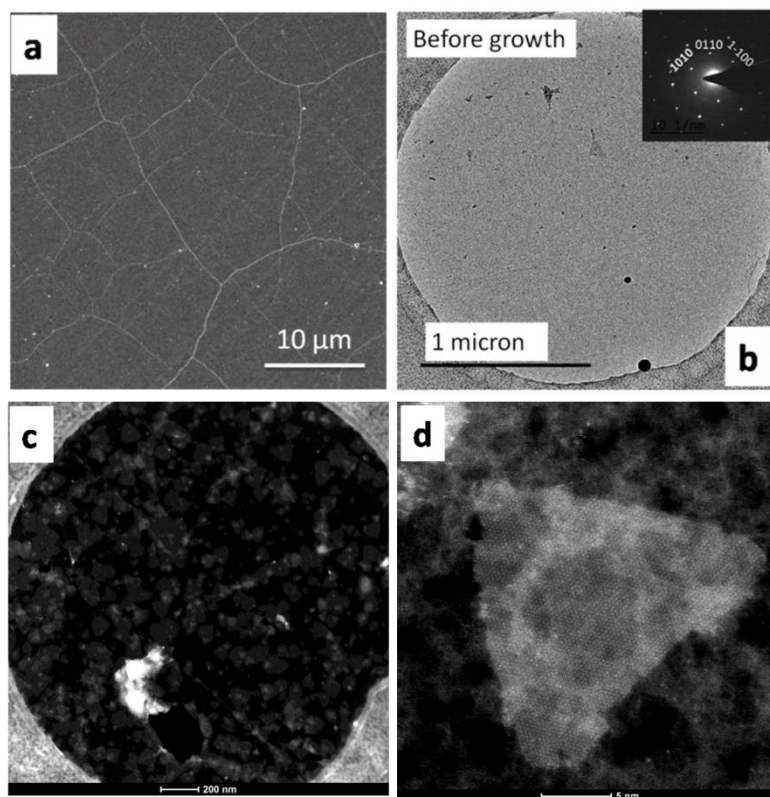


Figure 4-9. Synthesis of $\text{MoS}_2/\text{CVD-hBN}$ heterostructures (a) SEM image of hBN thin film on copper substrate growth via LP-CVD; (b) TEM images of CVD-hBN after transfer to a TEM grid, inset is the corresponding SAED pattern; (c) and (d) ADF-STEM image of the freestanding $\text{MoS}_2/\text{CVD-hBN}$ heterostructures.

Bright field (BF-) TEM image in Fig. 4-10a indicates the growth morphology of the as-grown heterostructures. SAED pattern shown in Fig. 4-10b contains a set of ring patterns which is indexed to match MoS_2 domains. In addition, a series of individual diffraction spots are seen and have been indexed to match the hBN structure. One of the hBN spots is selected by the objective aperture (the yellow spot in Fig. 4-10b), the corresponding hBN grains which give rise to the diffraction spot is lightened in the DF-TEM image in Fig. 4-10c, a grain boundary is clearly displayed by the contrast difference. DF-TEM image in Fig. 4-10d, shows the as-grown MoS_2 domains in certain orientations corresponding to the red circled spot. It is noted that MoS_2 nucleation is not preferred at the grain boundaries (or step edges) as we expected and observed previously. There are several possible

reasons for this phenomenon : (1) the hBN inevitably contains lots of surface defects due to the nature of CVD process which can introduce defects acting as nucleation sites instead of ideal defect-free vdW epitaxy; (2) PMMA-assisted transfer of hBN from copper to TEM grid also can introduce some undesired contamination and can even cover a thin layer of contamination across the grain boundaries and prohibit the growth; (3) PVT growth of MoS_2 will also contribute to the unclean interface.

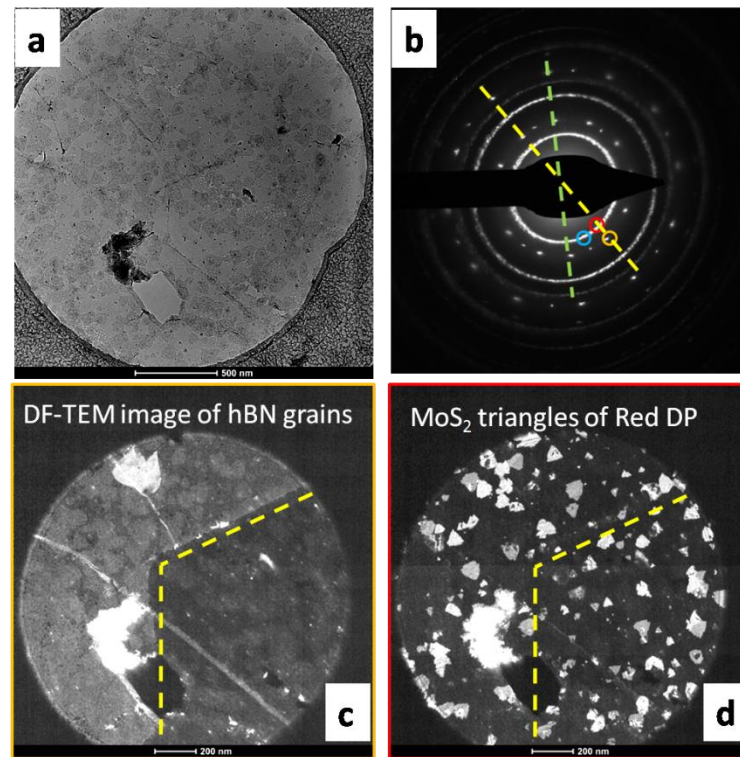


Figure 4-10. (a) BF-TEM image of MoS_2 /CVD-hBN heterostructures and (b) the corresponding SAED pattern; DF-TEM image of the freestanding MoS_2 /CVD-hBN heterostructures (c) corresponds to the yellow circle in (b) to show the CVD-hBN grain boundary; and (d) corresponds to the red circle in (b) to show the as-grown MoS_2 domains in which orientation can let the electron be diffracted to the spots in red circle.

In terms of clear interface, scalability, and controllability, the future strategies for fabrication of MoS_2 /hBN heterostructures need high quality hBN synthesis method, with minimal sample handling to eliminate the interface contamination. Some attempts has been tried via using a sulfide-

resistant metal as the template for hBN synthesis, which can realize the deposition of MoS₂ right after the growth of hBN films without sample transfer.²¹ These strategies can act as ways to synthesize TMD-based heterostructures to excite novel properties for 2D material applications.

4.3 Chapter summary

Epitaxial MoS₂/hBN vdW heterostructure is synthesized via PVT process, the well-defined and clean interface of the as-grown vdW heterostructure makes them perfect components for fabrication of high-performance electronics and optoelectronics. S/TEM imaging and spectroscopy are used to study the atomic structure and chemical composition of the as-grown heterostructure. We also experimentally verify the crucial role of substrate defects on the nucleation and growth of MoS₂/hBN heterostructure. As the hBN substrate defects increases by reactive ion etching, the resulting epitaxy is lost. Also introduction of defects decreases the MoS₂ domain size and layer thickness. This study uncovers the underlying physics by which van der Waals epitaxial growth can occur in 2D vdW heterostructure and can further serve as a powerful platform for engineering the substrate defects to tailor the implementation and functionality of devices in nanoscale.

4.4 References

1. Georgiou, T.; Jalil, R.; Belle, B. D.; Britnell, L.; Gorbachev, R. V.; Morozov, S. V.; Kim, Y.-J.; Gholinia, A.; Haigh, S. J.; Makarovskiy, O., Vertical field-effect transistor based on graphene-WS₂ heterostructures for flexible and transparent electronics. *Nature nanotechnology* 2013, 8 (2), 100-103.

2. Hunt, B.; Sanchez-Yamagishi, J.; Young, A.; Yankowitz, M.; LeRoy, B. J.; Watanabe, K.; Taniguchi, T.; Moon, P.; Koshino, M.; Jarillo-Herrero, P., Massive Dirac fermions and Hofstadter butterfly in a van der Waals heterostructure. *Science* 2013, 340 (6139), 1427-1430.
3. Lee, C.-H.; Lee, G.-H.; Van Der Zande, A. M.; Chen, W.; Li, Y.; Han, M.; Cui, X.; Arefe, G.; Nuckolls, C.; Heinz, T. F., Atomically thin p-n junctions with van der Waals heterointerfaces. *Nature nanotechnology* 2014, 9 (9), 676-681.
4. Larentis, S.; Tolsma, J. R.; Fallahazad, B.; Dillen, D. C.; Kim, K.; MacDonald, A. H.; Tutuc, E., Band offset and negative compressibility in graphene-MoS₂ heterostructures. *Nano letters* 2014, 14 (4), 2039-2045.
5. Lopez-Sanchez, O.; Alarcon Llado, E.; Koman, V.; Fontcuberta i Morral, A.; Radenovic, A.; Kis, A., Light Generation and Harvesting in a van der Waals Heterostructure. *Acs Nano* 2014, 8 (3), 3042-3048.
6. Wasala, M.; Zhang, J.; Ghosh, S.; Muchharla, B.; Malecek, R.; Mazumdar, D.; Samassekou, H.; Gaither-Ganim, M.; Morrison, A.; Lopez, N.-P., Effect of underlying boron nitride thickness on photocurrent response in molybdenum disulfide-boron nitride heterostructures. *Journal of Materials Research* 2016, 31 (07), 893-899.
7. Xu, X.; Yao, W.; Xiao, D.; Heinz, T. F., Spin and pseudospins in layered transition metal dichalcogenides. *Nature Physics* 2014, 10 (5), 343-350.
8. Lin, Y.-C.; Lu, N.; Perea-Lopez, N.; Li, J.; Lin, Z.; Peng, X.; Lee, C. H.; Sun, C.; Calderin, L.; Browning, P. N., Direct synthesis of van der Waals solids. *ACS nano* 2014, 8 (4), 3715-3723.
9. Shi, Y.; Zhou, W.; Lu, A.-Y.; Fang, W.; Lee, Y.-H.; Hsu, A. L.; Kim, S. M.; Kim, K. K.; Yang, H. Y.; Li, L.-J., van der Waals epitaxy of MoS₂ layers using graphene as growth templates. *Nano letters* 2012, 12 (6), 2784-2791.

10. Yan, A.; Velasco Jr, J.; Kahn, S.; Watanabe, K.; Taniguchi, T.; Wang, F.; Crommie, M. F.; Zettl, A., Direct growth of single-and few-layer MoS₂ on h-BN with preferred relative rotation angles. *Nano letters* 2015, 15 (10), 6324-6331.
11. Ling, X.; Lee, Y.-H.; Lin, Y.; Fang, W.; Yu, L.; Dresselhaus, M. S.; Kong, J., Role of the seeding promoter in MoS₂ growth by chemical vapor deposition. *Nano letters* 2014, 14 (2), 464-472.
12. Okada, M.; Sawazaki, T.; Watanabe, K.; Taniguchi, T.; Hibino, H.; Shinohara, H.; Kitaura, R., Direct chemical vapor deposition growth of WS₂ atomic layers on hexagonal boron nitride. *ACS nano* 2014, 8 (8), 8273-8277.
13. Wang, S.; Wang, X.; Warner, J. H., All Chemical Vapor Deposition Growth of MoS₂: h-BN Vertical van der Waals Heterostructures. *ACS nano* 2015, 9 (5), 5246-5254.
14. Fu, L.; Sun, Y.; Wu, N.; Mendes, R. G.; Chen, L.; Xu, Z.; Zhang, T.; Rummeli, M. H.; Rellinghaus, B.; Pohl, D., Direct Growth of MoS₂/h-BN Heterostructures via a Sulfide-Resistant Alloy. *ACS nano* 2016, 10 (2), 2063-2070.
15. Lee, C.; Yan, H.; Brus, L. E.; Heinz, T. F.; Hone, J.; Ryu, S., Anomalous lattice vibrations of single-and few-layer MoS₂. *ACS nano* 2010, 4 (5), 2695-2700.
16. Splendiani, A.; Sun, L.; Zhang, Y.; Li, T.; Kim, J.; Chim, C.-Y.; Galli, G.; Wang, F., Emerging photoluminescence in monolayer MoS₂. *Nano letters* 2010, 10 (4), 1271-1275.
17. Mak, K. F.; Lee, C.; Hone, J.; Shan, J.; Heinz, T. F., Atomically thin MoS₂: a new direct-gap semiconductor. *Physical Review Letters* 2010, 105 (13), 136805.
18. Alem, N.; Ramasse, Q. M.; Seabourne, C. R.; Yazyev, O. V.; Erickson, K.; Sarahan, M. C.; Kisielowski, C.; Scott, A. J.; Louie, S. G.; Zettl, A., Subangstrom edge relaxations probed by electron microscopy in hexagonal boron nitride. *Physical review letters* 2012, 109 (20), 205502.
19. Alem, N.; Yazyev, O. V.; Kisielowski, C.; Denes, P.; Dahmen, U.; Hartel, P.; Haider, M.; Bischoff, M.; Jiang, B.; Louie, S. G., Probing the out-of-plane distortion of single point defects in

atomically thin hexagonal boron nitride at the picometer scale. *Physical review letters* 2011, 106 (12), 126102.

20. Azizi, A.; Eichfeld, S.; Geschwind, G.; Zhang, K.; Jiang, B.; Mukherjee, D.; Hossain, L.; Piasecki, A. F.; Kabius, B.; Robinson, J. A., Freestanding van der waals heterostructures of graphene and transition metal dichalcogenides. *ACS nano* 2015, 9 (5), 4882-4890.

21. Alem, N.; Erni, R.; Kisielowski, C.; Rossell, M. D.; Hartel, P.; Jiang, B.; Gannett, W.; Zettl, A., Vacancy growth and migration dynamics in atomically thin hexagonal boron nitride under electron beam irradiation. *physica status solidi (RRL)-Rapid Research Letters* 2011, 5 (8), 295-297.

22. Zobelli, A.; Gloter, A.; Ewels, C.; Seifert, G.; Colliex, C., Electron knock-on cross section of carbon and boron nitride nanotubes. *Physical Review B* 2007, 75 (24), 245402.

23. Lifshits, V.; Oura, K.; Saranin, A.; Zotov, A.; Katayama, M., *Surface science: an introduction*. Berlin: Springer Verlag: 2003.

24. Alem, N.; Erni, R.; Kisielowski, C.; Rossell, M. D.; Gannett, W.; Zettl, A., Atomically thin hexagonal boron nitride probed by ultrahigh-resolution transmission electron microscopy. *Physical Review B* 2009, 80 (15), 155425.

25. Meyer, J. C.; Chuvilin, A.; Algara-Siller, G.; Biskupek, J.; Kaiser, U., Selective sputtering and atomic resolution imaging of atomically thin boron nitride membranes. *Nano letters* 2009, 9 (7), 2683-2689.

Chapter 5

(S)TEM Study of Defects in MOCVD-grown WSe₂ film

5.1 Introduction and Motivation

Tungsten diselenide (WSe₂), a representative semiconducting TMD, is considered as an outstanding candidate for optoelectronic devices due to its indirect to direct bandgap transition when thickness is reduced to monolayer. In addition, WSe₂ has a direct band gap in visible to infrared spectrum (~ 1.65 eV)¹ for field-effect transistors owing to its high carrier mobility^{2 3} and intrinsic p-type semiconducting characteristics^{4 5 6}. It has been demonstrated that transport properties of WSe₂ can be tuned to be either p-type or ambipolar behavior depending on the type of contact metals, which is a crucial component for 2D TMD-based p-n junctions.^{6 7} While significant effort has gone into scalable and controllable chemical vapor deposition (CVD) methods^{8 9 10 11 12} to obtain high-quality WSe₂, systematic atom-by-atom investigation of morphology and structural defects in metal organic (MO) CVD-grown WSe₂ film is not addressed. The atomic structure of the intrinsic defects can strongly impact their physical, chemical and electronic properties and consequently their functionalities in a devices. For example, the mechanical electronic properties of graphene can be deteriorated by certain types of grain boundaries.^{13 14} Density functional theory (DFT) calculations also show that a wide span of local density of states can be introduced near the defects and the grain boundaries in monolayer MoS₂.^{15 16} Thus it is crucial to uncover defects and determine their structures and functionality before they can be implemented into to effective use.

In this chapter, we have developed a universal and etchant-free transfer technique which enables transfer of the WSe₂ film from any substrate with high reliability. More importantly, we demonstrate a systematic investigation of the morphology and intrinsic defects in MOCVD-grown WSe₂ films, including point defects, dislocations and grain boundaries using aberration-corrected S/TEM imaging. The orientation and stacking in the as-grown WSe₂ film is determined and the presence of interlayer strain is also revealed via dark field imaging. We report the atom-by-atom visualization of various intrinsic defects including vacancies and anti-sites, possible grain boundary configurations (large angle and small angles, as well as 60° mirror boundary,). A new type of heart-shaped defect is also observed mostly along the reconstructed mirror boundary, showing great possibilities in tunable devices.

5.2 Metal-organic CVD (MOCVD) growth of tungsten diselenide (WSe₂) thin film

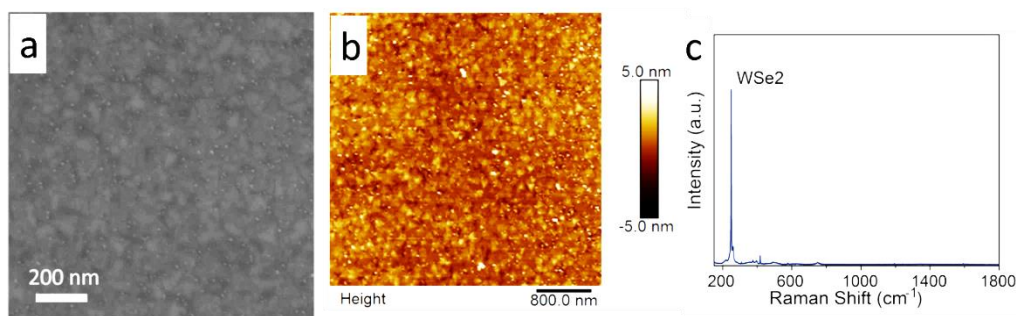


Figure 5-1. (a) SEM image, (b) AFM image and (c) Raman spectrum of the MOCVD-grown WSe₂ thin film

Thin films of WSe₂ were previously grown on (0001) sapphire substrate by MOCVD in a cold-wall reactor chamber using tungsten hexacarbonyl (W(CO)₆) and hydrogen selenide (H₂Se). Ultra-high purity hydrogen is used as the carrier gas through the bubblers and reactor.¹⁷ WSe₂ films were deposited on sapphire using the Se:W ratio of 3200 and substrate temperature of 800 °C. The SEM

and AFM images of the as-deposited thin film in Fig. 5-1a and Fig. 5-1b show that the coverage density of the WSe₂ domains are very high with a thickness of 1-4 nm. The presence of the E_{2g}¹ and A_{1g} characteristic peaks of WSe₂ in Raman spectrum are clearly observed in Fig. 5-2c.

5.3 Sample transfer and identification

It is important to transfer the synthesized WSe₂ films from sapphire onto target substrates such as plastics, silica and electrode to realize their application in flexible electronic and optoelectronic devices as well as electrocatalysis applications. It is challenging yet crucial to develop a method that can avoid damage during transfer process and can keep the film morphology intact with no tears and cracks. So far the existing transfer methods that can remove the films from various substrates may require highly concentrated chemical etchants that may be difficult to handle and may also affect the film structure and morphology. As an example, transfer of 2D crystal samples from sapphire or other commonly-use substrates involves highly concentrated acids, such as HF, for deep-etching at elevated temperatures. Here we have successfully developed a modified PMMA-assisted transfer method which enables transfer of the WSe₂ film from sapphire substrate (or any other substrate) onto other substrates. This opens up several opportunities in heterostructure stacking for device fabrication as well as fundamental research. The developed modified PMMA assisted transfer technique method does not require deep etching in hot acid/base solutions such as HF and KOH that is commonly practiced.^{18 19 20} Instead, the PMMA-covered film can be easily detached from the sapphire in water directly via the effective water penetration at the sapphire/WSe₂ film interface via capillary forces. This method eliminates the recently reported bubble generation from ultrasonication²¹ or exposure to etchant from pre-etching in NaOH solution²² and can prevent damage to the structure of the film. Due to the hydrophobic nature of the WSe₂²³ and PMMA as well as the hydrophilic character of sapphire^{24 25}, the film/PMMA

assembly is removed from sapphire substrate by dipping the sample into water with a tilted angle according to Fig. 5-2.

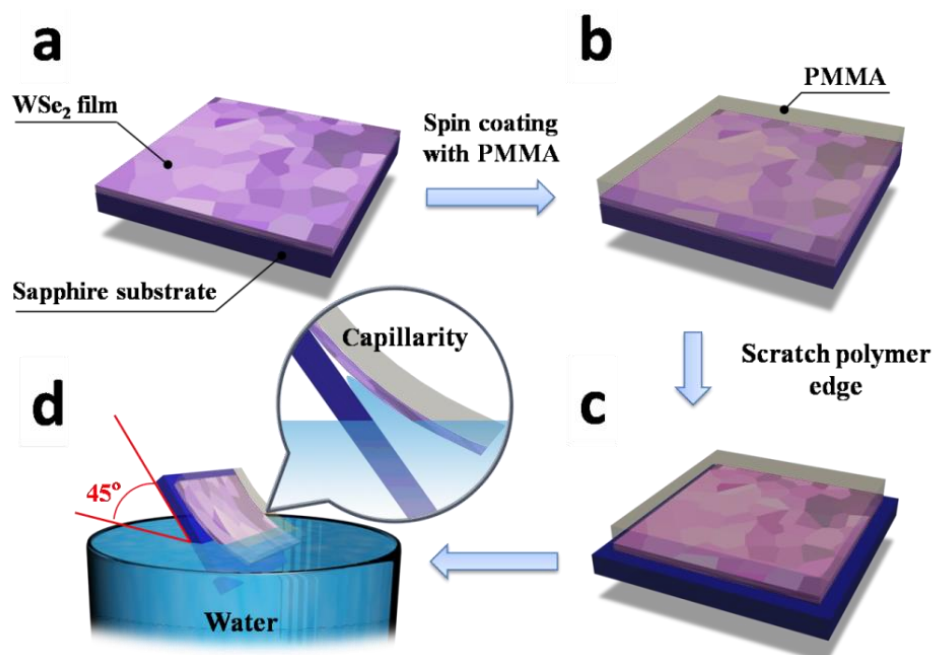


Figure 5-2. The schematic illustration of the etching-free PMMA assisted transfer method. (a) As-grown WSe₂ thin film on sapphire; (b) Spin-coating of PMMA on the as-grown WSe₂ film; (c) Scratching along the edge contour of the sapphire substrate using a blade or scalpel; (d) Immersion of the whole assembly into hot water ($\sim 80^\circ\text{C}$) for 5 to 10 minutes and then the hydrophobic PMMA/WSe₂ film will come off from sapphire substrate in water by a feeding angle $\sim 45^\circ$.

There are five main steps for the modified PMMA assisted transfer method : (1) Spin-coating of PMMA on the as-grown WSe₂ film. (PMMA 495 A6, spin coating speed 500 rpm for 15 seconds and then 4500 rpm for 45 seconds) The assembly should be kept at room temperature overnight for the PMMA to harden (Fig. 5-2b). (2) Scrape along the edge contour of the sapphire substrate using a blade or scalpel to open a sharp and small gap for water to penetrate between the film/PMMA and the substrate (Fig. 5-2c). (3) Immersion of the whole assembly into hot water ($\sim 80^\circ\text{C}$) for 5 to 10 minutes and then the hydrophobic PMMA/film will come off from sapphire substrate in water. In this step, the substrate feeding angle ($\sim 45^\circ$) and the delamination rate

(feeding rate : ~ 1 cm/s) should be kept low to minimize the stress and damage to the film (Fig. 5-2d). (4) PMMA/film can be carefully removed from the water bath with any arbitrary target substrate (in our case the substrate is Quantifoil Au TEM grid). To improve attachment of the film onto the target substrate, the PMMA/WSe₂ film coated substrate is placed on the hot plate for 10 minutes. (5) Removal of the PMMA with acetone and further cleaning of the residuals polymer with IPA/methanol, respectively. The modified PMMA-assisted transfer method developed here is facile, fast and most importantly etchant-free and thus eliminates and potential sample damage and contamination during the transfer process.

5.4 TEM investigation of grain and grain boundary structures of WSe₂ thin film

5.4.1 Orientation and layer stacking of the MOCVD-grown WSe₂ film

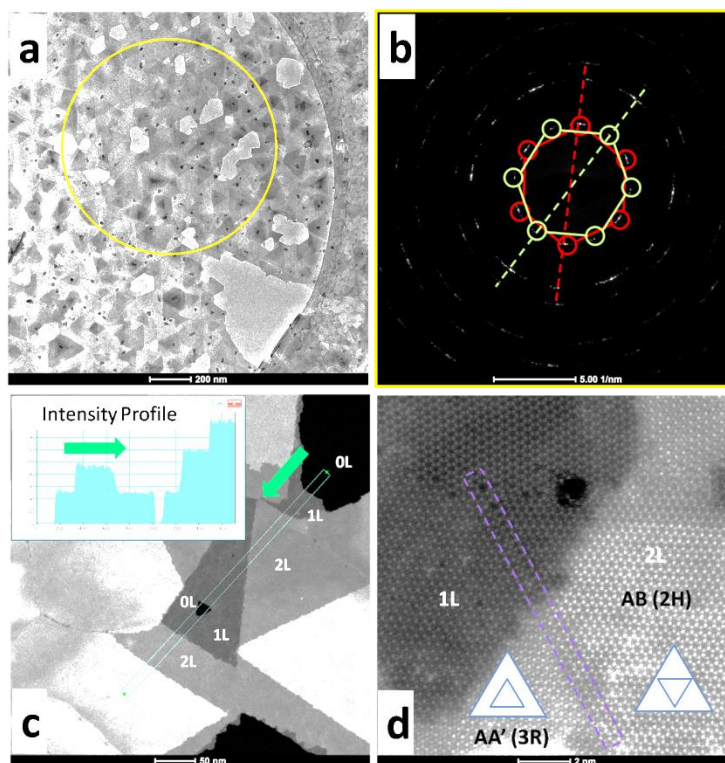


Figure 5-3. (a) Conventional TEM image of MOCVD-grown WSe₂ coalesce films. (b) SAED pattern of the yellow circled part in (a), it mainly contains two sets of hexagonal diffraction patterns which is 30° misoriented, to illustrate the epitaxy of WSe₂ growth on sapphire; (c) Sequent layers (0 layer to 3 layers) of WSe₂ are identified by the intensity profile in STEM imaging, inset is the intensity profile; (d) Atomic resolution ADF/STEM image of grain and grain boundaries in WSe₂ films, a 60° grain boundary is purple-circled, direct connection of AA' stacking and AB stacking in bilayer WSe₂ is also being observed.

In this study we transferred the as-grown WSe₂ films from sapphire onto the Quantifoil Au grid using the etchant-free PMMA-assisted transfer method for atomic scale investigation of the structure using Aberration-corrected S/TEM. This understanding is crucial for designing and engineering electronic and optoelectronic devices based on WSe₂. Low-magnitude TEM image in Fig. 5-3a shows the morphology of the as-grown WSe₂ with small triangular domains emerged with each other to form a film with some uncovered areas in between. Dissimilar diffraction contrasts for various grains in Fig. 5-3a indicate that the film thickness varies from single layer to few layers. The SAED pattern (Fig. 5-3b) from the circled area in Fig. 5-3a shows a clearly discernible hexagonal symmetry of the WSe₂ film. Two main WSe₂ domain orientations can be observed from the SAED pattern with 30° misorientation. Similar domain orientations have also been reported²⁶ for MoS₂ grown on C-plane sapphire. Density functional theory (DFT) simulations show the most stable stacking between TMDs and sapphire to occur at either 0° and 30° misorientation. The as-grown WSe₂ film is composed of separated triangular domains epitaxial grown on the substrate with little to no misorientation. At the initial stage, the small nuclei of WSe₂ can be formed on the sapphire substrate and stabilize.²⁶ Due to vdW forces between TMD and (0001)-sapphire however, the nuclei could rotate on the surface of sapphire with low energy barrier and eventually get pinned down at the most stable orientation with respect to the substrate. The nuclei spreads laterally as the growth proceeds to form a coalesced film. Layer numbers of the WSe₂ across the film can be identified via scanning the intensity of the film profile in STEM mode. Single to few layer regions (0L to 3L in Fig. 5-3c) can be distinguished via a linear relationship between the layer number and

image intensity in STEM mode. The atomic resolution STEM image in Fig. 5-3d shows a region with one to two layers 1L to 2L with a 60° grain boundary (mirror boundary) indicated by the purple dashed line. Mirror boundaries in monolayer MoS_2 has been predicted to have a metallic nature that can act as a bridge between two semiconducting domains.¹⁶ The subsequent layer spreads as one domain across the grain boundary underneath thus leaves a distinct stacking feature in this region, which displays a connection between AA' stacking (2H) and AB stacking (3R). Recent studies have shown the distinct spectroscopy response (resonance Raman and photoluminescence) between these two phases due to the different interlayer interactions with the photons.^{27 28} The electronic coupling at the interface will provide novel properties with promising applications on the next generation optoelectronics and valleytronics.^{27 29}

5.4.2 Dark field imaging (Strain induced contrast difference in +g vector and -g vector)

Dark field imaging is performed to shed light on the WSe_2 domains oriented in certain directions. Annular Dark Field (ADF)-STEM image in Fig. 5-4a displays the thickness variation in the WSe_2 coalesce films. In ADF-STEM, the layer number is can be determined from the intensity. Here, we from the intensity of the ADF-STEM image, the neighboring WSe_2 domains epitaxially grow on top of the initial layers, with 0° or 60° misorientation, with the additional triangular layers nucleating in the middle of the basal plane of WSe_2 triangle.

We perform diffraction contrast imaging in the TEM mode, to further determine the registry and coalescence of the domains in this sample. We use the smallest objective aperture ($10\ \mu\text{m}$ in diameter) to select a part of diffraction pattern in Fig. 5-4b, as "+g" vector (circled by yellow color, the objective aperture selects a series of neighboring diffraction spots), the corresponding DF-TEM image is shown in Fig. 5-4d, which have intensity variations between different domains. Similarly, we form a DF-TEM image using the "-g" vector (Fig. 5-4c.) by selecting the opposite part of

diffraction pattern with exact reverse symmetry with respect to the $+g$ vector in Fig. 5-4b (circled by blue color). A clear intensity difference can be indentified in the two DF-TEM images although according to the discernible hexagonal symmetry of the WSe_2 crystal structure, $+g$ and $-g$ vectors should result in the same dark field image display.

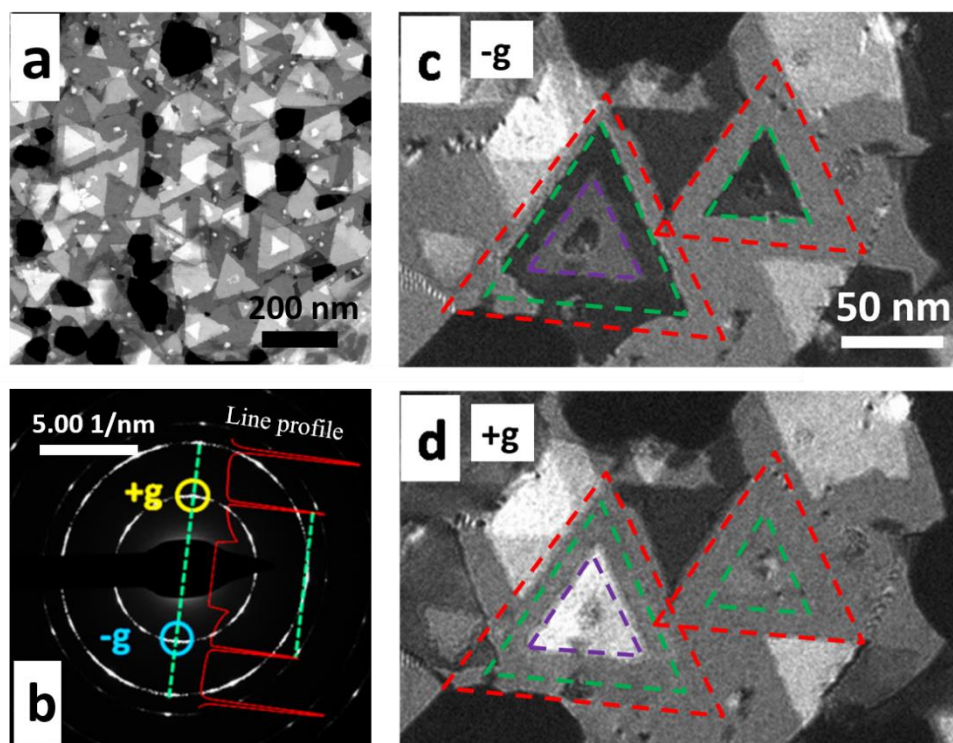


Figure 5-4. Dark field imaging of the WSe_2 film (a) ADF-STEM image of the WSe_2 film; (b) SAED pattern of the region shows the dispersive domain orientations, a part of the diffraction spots region is selected by objective aperture denoted as " $+g$ " vector (yellow circle) to achieve the corresponding dark field image (c); and the dark field image (d) which is get from the reversed symmetric part of the diffraction spots as " $-g$ " vector (yellow circle); the intensity profile (redline) in (b) indicates a slight sample tilt exists during the imaging.

The striking feature in these two DF-TEM images can be explained via the Ewald's Sphere construction³⁰ in reciprocal space. For two dimensional materials, the sample is already atomically thin with the c -axis already on the zone axis (0001). In reciprocal space, the Fourier Transfer (FT) of a finite size of 2D disk (WSe_2 domain in this case) is a rel-rod according to the Friedel's law.

The schematic of reciprocal space is illustrated in Fig. 5-5a, for single layer case, the rel-rod is long and when they cut through the Ewald's Sphere (ES), the diffraction will occur and form a spot in the SAED pattern. In the case when the sample is perfectly on the zone axis (0001), the intensity of the diffracted spots $+g$ and $-g$ are the same. While in practical TEM imaging process, slight sample tilt can exist. Also presence of point defects and grain boundaries in the film will inevitably cause the local plane bending.³³ Thus the cut-through between the ES and rel-rods will deviate from the perfect symmetry case. This will lead to an intensity difference between the diffracted spots $+g$ and $-g$ (Fig. 5-5b). From the intensity profile of the diffraction pattern (the inset red plot in the SAED pattern in Fig. 5-5b) there is a clear difference in the intensity of the diffracted spots $+g$ and $-g$, therefore a slight sample tilt is existing.

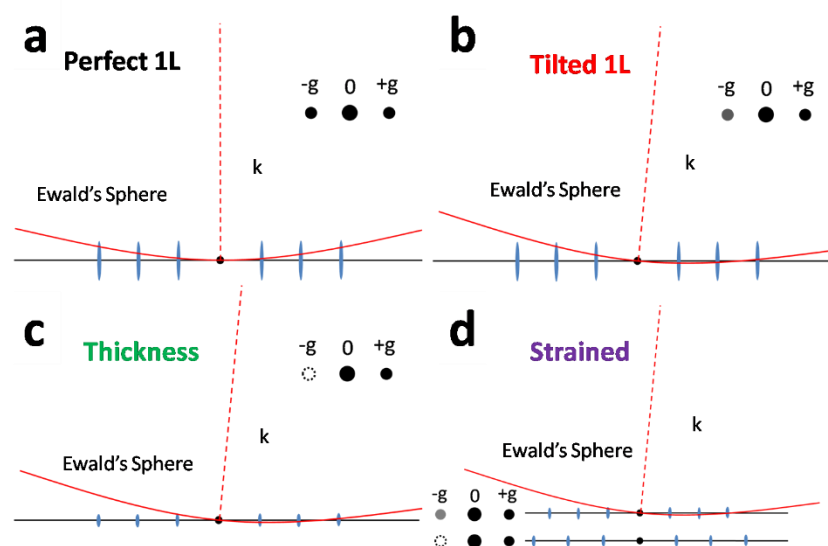


Figure 5-5. Two dimensional schematic illustration of the Ewald's Sphere construction in reciprocal space (a) Perfect-aligned for electron beam and single layer sample on the zone axis (0001) results in the equal intensity for $+g$ and $-g$ diffraction spots; (b) Slight sample tilt or bending induce the asymmetric cut-through between the ES and rel-rods; (c) Sample thickness affect the height of reciprocal rel-rods lead to a larger intensity difference between the diffracted spots $+g$ and $-g$ which may even form a two-beam condition (the $-g$ has no intensity); (d) The positions of rel-rods are modified by lattice strain and have an influence of the cut-through between the ES and rel-rods, which light up the non-diffracted region.

When the thickness increases, the corresponding rel-rod will be shorter due to the inverse relationship between the real and reciprocal space. This will affect the cut-through between the ES and rel-rods (Fig. 5-5c), which will lead to a significant intensity difference between the diffracted spots +g and -g. This results in the contrast between dashline-marked regions in the red triangle and in the green triangle (Fig. 5-5c). But a distinct feature can be obtained from the two DF-TEM images in Fig. 5-5c, which shows that when the layer number further increases, the sequent domains will show up as bright. This phenomenon cannot be explained just by the sample tilt and thickness effect. In fact, we assume that the as-grown WSe₂ film is expected to suffer from strain which will change the lattice parameter slightly. This will influence the position of rel-rods in the reciprocal space, which affects the cut-through between the ES and rel-rods (Fig. 5-5d) and possibly lights up the region where supposed to show dark contrast.

The strain is believed to form by two reasons : (1) From the growth process, although it is well understood that layered TMDs are grown on sapphire via vdW epitaxy on sapphire.²⁶ This means there is weak vdW bonding between the substrate and TMDs. Dangling bonds on the surface of sapphire will still play a role in the interlayer bonding. In comparison, the subsequent layer of TMDs may grow via vdW epitaxy on the initial surface. Consequently, the big lattice mismatch between WSe₂ (0001) plane and the underlying sapphire (0001) plane will inevitably introduce strain at the WSe₂ triangular domain/substrate in the CVD process. Several studies have shown Raman and PL shifts between freestanding TMDs compared with TMDs grown on sapphire.^{31 32} This effect will be magnified when we synthesize a continuous film with triangular domains expanding and emerging to form grain boundaries. The difference in the expansion coefficient between sapphire (XY-plane thermal coefficient is $8.1 \times 10^{-6} / ^\circ\text{C}$) and WSe₂ (in-plane thermal coefficient is $11.08 \times 10^{-6} / ^\circ\text{C}$) will contribute to the film strain during the fast cooling in MOCVD

process (0.23 % strain remaining from 800 °C). Sample transfer from sapphire to TEM grid will release the strain between the initial WSe₂ layer and the substrate. However, it may generate strain between the initial WSe₂ layer and the subsequent layer. (2) Defects in the films will also play a crucial role in the strain formation. Besides the significant strain associated with the grain boundaries in the film,³³ The inevitable in-plane point defects formed during the growth can also serve dangling bonds for the nucleation of the next layer and affect the sequent layer formation. Experimental observations and simulation calculations both consider strain to have a profound effect on the resulting electronic^{34 35}, optoelectronic³⁶ and catalysis³⁷ properties in the TMDs. This study is also a direct observation to show the formation of strain via the vdW growth of layered 2D material thin films. Raman and PL measurement can further uncover the intrinsic strain and its effect on the optoelectronic properties in TMDs grown by the MOCVD growth process and can further offer controlled synthesis techniques to achieve epitaxial, large area strain-free TMDs film.

5.4.3 Point defects in the MOCVD-grown WSe₂ film

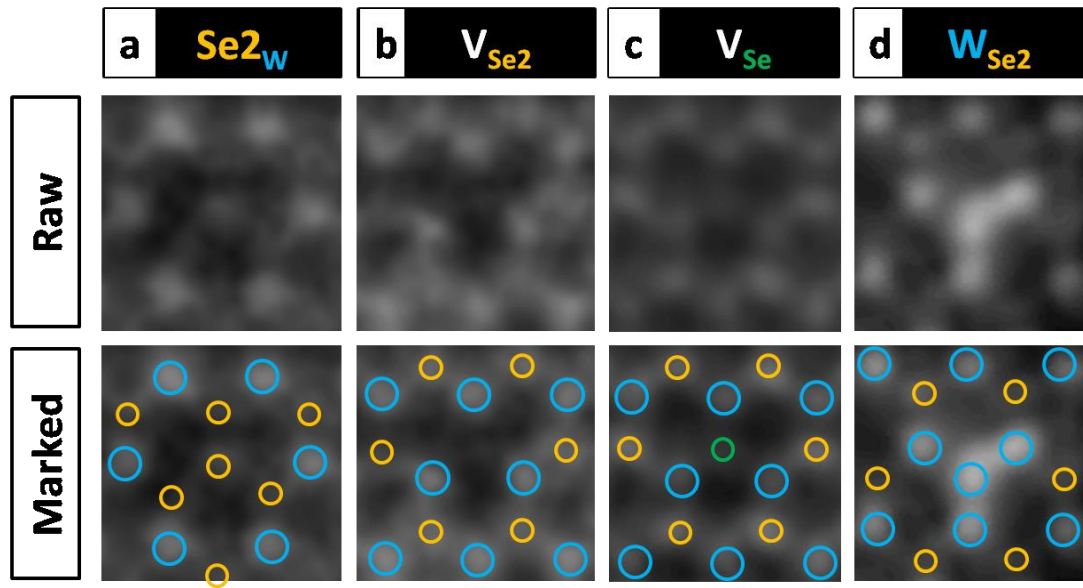


Figure 5-6. Visualization of various intrinsic point defects in monolayer MOCVD-grown WSe₂. Atomic resolution ADF-STEM image of vacancy and antisites including (a) Se_{2W}; (b) V_{Se2}; (c) V_{Se}; and (d) W_{Se2}. The marked version in the lower row display the atom identities of tungsten (blue) and selenium (yellow).

The performance of TMD-based electronics and optoelectronics are strong functions of the structural and defective morphology. Here we provide a comprehensive exploration on the intrinsic structural defects in MOCVD-grown WSe₂ film, including point defects, dislocation cores and grain boundaries, visualized by atomic resolution S/TEM imaging. Intrinsic point defects in WSe₂ are mostly formed by the nonequilibrium thermodynamic conditions during the MOCVD process. They have profound effects on the mechanical, electrical and catalytical performance of 2D materials.^{13 38 39} Various point defects can be classified into two categories : vacancies and antisite defects. Four typical species of point defects observed in the MOCVD grown monolayer WSe₂ are shown in the zoomed-in ADF-STEM images (Figure 5-6), which are antisite defect that a Se₂ column substitute W atom (Se_{2W}), diselenium vacancy (V_{Se2}), monoselenium vacancy (V_{Se}) and antisite defect that a W atom substitute Se₂ column (W_{Se2}). The atomic chemical analysis ability of ADF-STEM imaging enable us to unambiguously separate the antisites from unperturbed lattice sites and distinguish a monoselenium vacancy from diselenium vacancy. The concentration and stability of the point defects are determined by the formation energies and growth conditions (temperature, pressure and concentration of the precursors). The formation energies of common point defects are calculated for MoS₂ (another member of TMDs),^{15, 40 41} it is suggested that the formation energy of the point defects are a function of transition metal potential and chalcogen atom potential, which correlates to the experimental conditions range from transition metal-rich to chalcogen-rich.¹⁵ The monosulfur vacancy is calculated to have the lowest formation energy, this is similar to our case that V_{Se} are found to be the most abundant defects throughout the sample. In contrast, there is seldom V_W (monotungsten vacancy) is isolated observed which suggests a higher formation energy is needed for V_W formation at the pristine lattice. Further DFT calculations on

the detailed formation energy of defects are imperative to demonstrate the intrinsic defect structures in the as-grown WSe₂. The induced additional electronic states at local electronic structure of WSe₂ due to the observed defects is also need to be calculated in order to reveal the reason for the intrinsic p-type nature of WSe₂ compared to the n-type MoS₂.

5.4.4 Grain boundary structures in the MOCVD-grown WSe₂ film

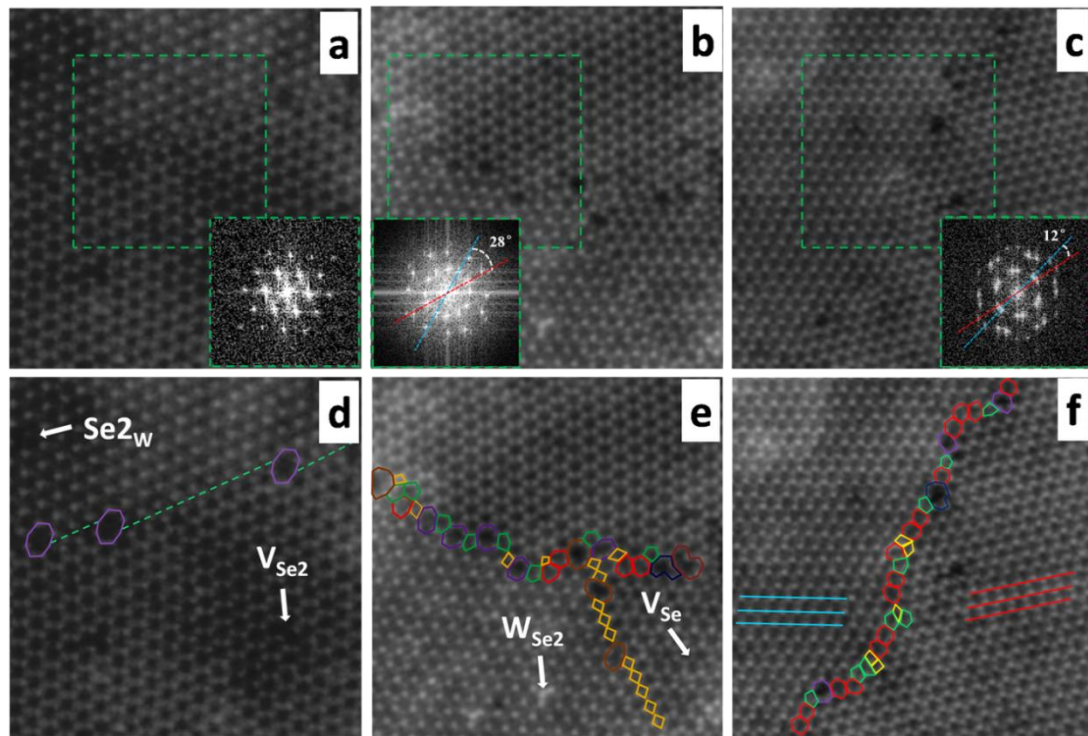


Figure 5-7. Atomic structures of dislocations and grain boundaries. ADF-STEM images of grain boundaries (a) and (d) 60° GB; (b) and (e) large angle GB (28°); (c) and (f) small angle GB (12°). The inset FFTs of the green-squared region in (a) to (c) illustrate the relative misorientation of the two grains; various polygonal structures marked by different colors as schematically shown in (d) to (f) reveal the detailed atomic structure along the grain boundaries.

The peculiar in-plane bonding characteristics between W and Se can generate different dislocation core configurations, including experimentally and theoretically observed dislocations including 5-

and 7-fold (5|7) as well as 4|4, 4|6, 4|8 and 6|8 fold rings.¹⁶ Figure 5-7a and d show a 60° GB (mirror twin boundary) in WSe₂, stitched by 4|4 rings at common Se₂ sites (4|4 structure) via point sharing parallel to the zigzag geometry of the WSe₂ lattice. The inset FFT of the green-squared region in Fig. 5-7a shows one set of hexagonal patterns resulting from two emerging grains with 0° and 60° rotations as indicated in the FFT pattern. The W atoms along the mirror plane keep the 6-fold coordination, while Se atom coordination is changed from 3-fold to 4-fold symmetry leading to Se-deficiency with WSe_{1.5}. As can be seen from Fig. 5-7d, the GB indeed continues by a series of 4|4 rings interrupted by two octagonal kinks along the glide directions. Such mirror twin GB structures have been recently predicted to behave as 1D metallic channels glued between two intrinsic semiconducting WSe₂ grains,^{15 16} which can generate novel electronic properties and devices in monolayer WSe₂.

Besides the mirror-symmetric 4|4 structural GBs, other possible GB configurations with large and small angles are also observed. Fig. 5-7b and e show a monolayer region with three grains at a junction with each other. A mirror twin boundary is observed at the lower side of the junction with 4-fold dislocation rings arrayed in a line. This Figure also shows another nearly horizontal grain boundary which connects the top and bottom grains via a 28° GB angle. This grain boundary is composed of various tightly packed 5-7 dislocations serving as the building blocks to construct the GB as schematically shown in Fig. 5-7e (marked by different colors). Similarly we observe 5|7 dislocations along smaller angle (12°) grain boundaries with larger spacings as shown in Fig. 5-7c and f. Such grain boundary structures are not only controlled by the original orientation of the grain, but also through the local variation of reactant species, such as W and Se, during the growth process. The observed grain boundary structures also point to the critical role, the adjustment of the synthesis process can play to obtain a large-area pristine and coalesced film.

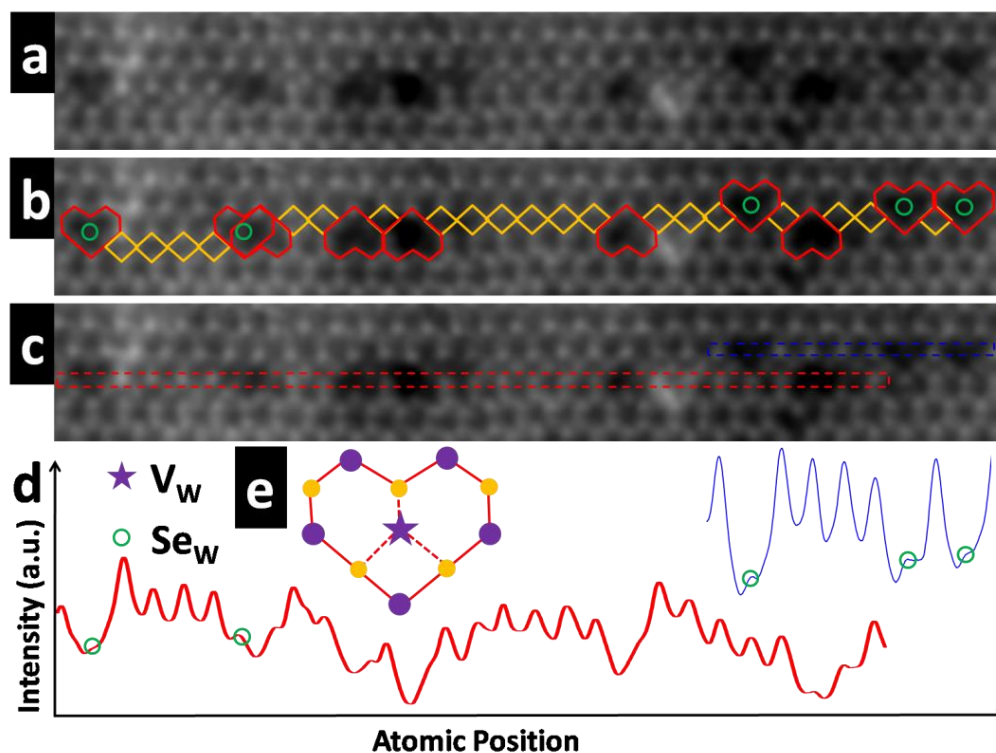


Figure 5-8. Atomic structure of heart-shaped defects along the reconstructed mirror boundaries (a) Raw and (b) marked data with polygonal structures including yellow rhombuses and red heart-shaped defects; (c) and (d) image intensity profile along the grain boundaries to show the W vacancy and antisite defects that Se substitute on W site. (e) Schematic of heart-shaped defect indicate that a V_W interact with the mirror boundary.

Another commonly observed defects along the GB in the MOCVD-grown WSe_2 film is shown in Fig. 5-8, which has not been observed or predicted before. A heart-shaped dislocation core will form along the mirror boundaries when a V_W is associated with a 4-fold dislocation array (Fig. 5-8e). It has been demonstrated that the formation energy of transition metal vacancy is very high and is seldom observed to be alone by itself.¹⁵ While metal vacancies are considered rare in TMD alloys, the interaction between the Se-deficient mirror boundaries and a V_W can vary the local W:Se ratio and further accommodate incorporation of heart-shaped dislocation core metal vacancies locally at the mirror GB. Calculations are needed to further determine the energetics of the formation of such defects at the mirror boundary and their resulting electronic structure. We also

observed Se atoms to be trapped at the V_W site (green circles in the schematic figure) which can further modify the electronic structure of these defects. In addition, this large vacancy defect can act as a preferential site for adatoms or dopants with applications in chemical sensing⁴² and hydrogen generation⁴³. Furthermore, DFT simulations is imperative to investigate the coupling effect of the tungsten vacancies on the electronic structure of such metallic mirror boundary.

Dislocation cores and grain boundaries are at the heart of the condensed matter phenomena and will not only act as scattering centers leading to carrier mobility decrease, but also act as potential reactive sites for catalysis applications. Through a controlled synthesis process, the quality and structure of WSe_2 film can further be modified and further enable investigation of fundamental phenomena, such as electronic and optoelectronic behavior in this fascinating material.⁵

5.5 Chapter summary and future work

We have developed a universal and etchant-free transfer technique which enables transfer of the WSe_2 film onto arbitrary substrates with high reliability. More importantly, we demonstrate investigation of the atomic structure, morphology and the intrinsic defects in the MOCVD-grown WSe_2 film, including point defects, dislocations and grain boundaries using aberration-corrected S/TEM imaging. The orientation and stacking of as-grown WSe_2 film is explored and the presence of interlayer strain is also revealed via dark field imaging. We report the atom-by-atom visualization of various intrinsic defects including vacancies and anti-sites, possible grain boundary configurations (with 60° mirror boundary, large angle and small angle). A new type of heart-shaped defects is also observed along the reconstructed mirror boundary. We believe such an investigation will be a guidance for future growth approaches aiming to obtain high quality TMD films which can greatly facilitate the exploration of condensed matter phenomena in these

fascinating 2D systems. In addition, DFT calculations of the possible structures and their electronic properties are necessary for the future work in the MOCVD-grown WSe₂ film.

5.6 Reference

1. Terrones, H.; López-Urías, F.; Terrones, M., Novel hetero-layered materials with tunable direct band gaps by sandwiching different metal disulfides and diselenides. *Scientific reports* 2013,
2. Chuang, H.-J.; Tan, X.; Ghimire, N. J.; Perera, M. M.; Chamlagain, B.; Cheng, M. M.-C.; Yan, J.; Mandrus, D.; Tománek, D.; Zhou, Z., High mobility WSe₂ p-and n-type field-effect transistors contacted by highly doped graphene for low-resistance contacts. *Nano letters* 2014, 14 (6), 3594-3601.
3. Movva, H. C.; Rai, A.; Kang, S.; Kim, K.; Fallahazad, B.; Taniguchi, T.; Watanabe, K.; Tutuc, E.; Banerjee, S. K., High-Mobility Holes in Dual-Gated WSe₂ Field-Effect Transistors. *ACS nano* 2015, 9 (10), 10402-10410.
4. Zhou, H.; Wang, C.; Shaw, J. C.; Cheng, R.; Chen, Y.; Huang, X.; Liu, Y.; Weiss, N. O.; Lin, Z.; Huang, Y., Large area growth and electrical properties of p-type WSe₂ atomic layers. *Nano letters* 2014, 15 (1), 709-713.
5. Wang, J.; Rhodes, D.; Feng, S.; Nguyen, M. A. T.; Watanabe, K.; Taniguchi, T.; Mallouk, T. E.; Terrones, M.; Balicas, L.; Zhu, J., Gate-modulated conductance of few-layer WSe₂ field-effect transistors in the subgap regime: Schottky barrier transistor and subgap impurity states. *Applied Physics Letters* 2015, 106 (15), 152104.
6. Fang, H.; Chuang, S.; Chang, T. C.; Takei, K.; Takahashi, T.; Javey, A., High-performance single layered WSe₂ p-FETs with chemically doped contacts. *Nano letters* 2012, 12 (7), 3788-3792.

7. Liu, B.; Fathi, M.; Chen, L.; Abbas, A.; Ma, Y.; Zhou, C., Chemical vapor deposition growth of monolayer WSe₂ with tunable device characteristics and growth mechanism study. *ACS nano* 2015, 9 (6), 6119-6127.
8. Browning, P.; Eichfeld, S.; Zhang, K.; Hossain, L.; Lin, Y.-C.; Wang, K.; Lu, N.; Waite, A.; Voevodin, A.; Kim, M., Large-area synthesis of WSe₂ from WO₃ by selenium–oxygen ion exchange. *2D Materials* 2015, 2 (1), 014003.
9. Eichfeld, S. M.; Hossain, L.; Lin, Y.-C.; Piasecki, A. F.; Kupp, B.; Birdwell, A. G.; Burke, R. A.; Lu, N.; Peng, X.; Li, J., Highly scalable, atomically thin WSe₂ grown via metal–organic chemical vapor deposition. *ACS nano* 2015, 9 (2), 2080-2087.
10. Huang, J.-K.; Pu, J.; Hsu, C.-L.; Chiu, M.-H.; Juang, Z.-Y.; Chang, Y.-H.; Chang, W.-H.; Iwasa, Y.; Takenobu, T.; Li, L.-J., Large-area synthesis of highly crystalline WSe₂ monolayers and device applications. *ACS nano* 2013, 8 (1), 923-930.
11. Cheng, R.; Li, D.; Zhou, H.; Wang, C.; Yin, A.; Jiang, S.; Liu, Y.; Chen, Y.; Huang, Y.; Duan, X., Electroluminescence and photocurrent generation from atomically sharp WSe₂/MoS₂ heterojunction p–n diodes. *Nano letters* 2014, 14 (10), 5590-5597.
12. Chen, J.; Liu, B.; Liu, Y.; Tang, W.; Nai, C. T.; Li, L.; Zheng, J.; Gao, L.; Zheng, Y.; Shin, H. S., Chemical Vapor Deposition of Large - Sized Hexagonal WSe₂ Crystals on Dielectric Substrates. *Advanced Materials* 2015, 27 (42), 6722-6727.
13. Wei, Y.; Wu, J.; Yin, H.; Shi, X.; Yang, R.; Dresselhaus, M., The nature of strength enhancement and weakening by pentagon–heptagon defects in graphene. *Nature materials* 2012, 11 (9), 759-763.
14. Yazyev, O. V.; Louie, S. G., Electronic transport in polycrystalline graphene. *Nature materials* 2010, 9 (10), 806-809.

15. Zhou, W.; Zou, X.; Najmaei, S.; Liu, Z.; Shi, Y.; Kong, J.; Lou, J.; Ajayan, P. M.; Yakobson, B. I.; Idrobo, J.-C., Intrinsic structural defects in monolayer molybdenum disulfide. *Nano letters* 2013, 13 (6), 2615-2622.
16. Zou, X.; Liu, Y.; Yakobson, B. I., Predicting dislocations and grain boundaries in two-dimensional metal-disulfides from the first principles. *Nano letters* 2012, 13 (1), 253-258.
17. Zhang, X.; Al Balushi, Z. Y.; Zhang, F.; Choudhury, T. H.; Eichfeld, S. M.; Alem, N.; Jackson, T. N.; Robinson, J. A.; Redwing, J. M., Influence of Carbon in Metalorganic Chemical Vapor Deposition of Few-Layer WSe₂ Thin Films. *Journal of Electronic Materials* 2016, 45 (12), 6273-6279.
18. Lin, Y.-C.; Zhang, W.; Huang, J.-K.; Liu, K.-K.; Lee, Y.-H.; Liang, C.-T.; Chu, C.-W.; Li, L.-J., Wafer-scale MoS₂ thin layers prepared by MoO₃ sulfurization. *Nanoscale* 2012, 4 (20), 6637-6641.
19. Elias, A. L.; Perea-López, N.; Castro-Beltrán, A.; Berkdemir, A.; Lv, R.; Feng, S.; Long, A. D.; Hayashi, T.; Kim, Y. A.; Endo, M., Controlled synthesis and transfer of large-area WS₂ sheets: from single layer to few layers. *Acs Nano* 2013, 7 (6), 5235-5242.
20. Zhang, Y.; Zhang, Y.; Ji, Q.; Ju, J.; Yuan, H.; Shi, J.; Gao, T.; Ma, D.; Liu, M.; Chen, Y., Controlled growth of high-quality monolayer WS₂ layers on sapphire and imaging its grain boundary. *ACS nano* 2013, 7 (10), 8963-8971.
21. Ma, D.; Shi, J.; Ji, Q.; Chen, K.; Yin, J.; Lin, Y.; Zhang, Y.; Liu, M.; Feng, Q.; Song, X., A universal etching-free transfer of MoS₂ films for applications in photodetectors. *Nano Research* 2015, 8 (11), 3662-3672.
22. Xu, Z.-Q.; Zhang, Y.; Lin, S.; Zheng, C.; Zhong, Y. L.; Xia, X.; Li, Z.; Sophia, P. J.; Fuhrer, M. S.; Cheng, Y.-B., Synthesis and transfer of large-area monolayer WS₂ crystals: moving toward the recyclable use of sapphire substrates. *ACS nano* 2015, 9 (6), 6178-6187.

23. Chow, P. K.; Singh, E.; Viana, B. C.; Gao, J.; Luo, J.; Li, J.; Lin, Z.; Elías, A. L.; Shi, Y.; Wang, Z., Wetting of mono and few-layered WS₂ and MoS₂ films supported on Si/SiO₂ substrates. *ACS nano* 2015, 9 (3), 3023-3031.
24. Azimi, G.; Dhiman, R.; Kwon, H.-M.; Paxson, A. T.; Varanasi, K. K., Hydrophobicity of rare-earth oxide ceramics. *Nature materials* 2013, 12 (4), 315-320.
25. Gurarlan, A.; Yu, Y.; Su, L.; Yu, Y.; Suarez, F.; Yao, S.; Zhu, Y.; Ozturk, M.; Zhang, Y.; Cao, L., Surface-energy-assisted perfect transfer of centimeter-scale monolayer and few-layer MoS₂ films onto arbitrary substrates. *ACS nano* 2014, 8 (11), 11522-11528.
26. Dumcenco, D.; Ovchinnikov, D.; Marinov, K.; Lazic, P.; Gibertini, M.; Marzari, N.; Sanchez, O. L.; Kung, Y.-C.; Krasnozhon, D.; Chen, M.-W., Large-area epitaxial monolayer MoS₂. *ACS nano* 2015, 9 (4), 4611-4620.
27. Xia, M.; Li, B.; Yin, K.; Capellini, G.; Niu, G.; Gong, Y.; Zhou, W.; Ajayan, P. M.; Xie, Y.-H., Spectroscopic Signatures of AA' and AB Stacking of Chemical Vapor Deposited Bilayer MoS₂. *ACS nano* 2015, 9 (12), 12246-12254.
28. Yan, J.; Xia, J.; Wang, X.; Liu, L.; Kuo, J.-L.; Tay, B. K.; Chen, S.; Zhou, W.; Liu, Z.; Shen, Z. X., Stacking-dependent interlayer coupling in trilayer MoS₂ with broken inversion symmetry. *Nano letters* 2015, 15 (12), 8155-8161.
29. Suzuki, R.; Sakano, M.; Zhang, Y.; Akashi, R.; Morikawa, D.; Harasawa, A.; Yaji, K.; Kuroda, K.; Miyamoto, K.; Okuda, T., Valley-dependent spin polarization in bulk MoS₂ with broken inversion symmetry. *Nature nanotechnology* 2014, 9 (8), 611-617.
30. Williams, D. B.; Carter, C. B., *Transmission electron microscopy: a textbook for materials science*. Springer, New York London: 2009.
31. Buscema, M.; Steele, G. A.; van der Zant, H. S.; Castellanos-Gomez, A., The effect of the substrate on the Raman and photoluminescence emission of single-layer MoS₂. *Nano Research* 2014, 7 (4), 561-571.

32. Lippert, S.; Schneider, L. M.; Renaud, D.; Kang, K. N.; Ajayi, O.; Halbach, M.-U.; Abdulmunem, O. M.; Lin, X.; Kuhnert, J.; Hassoon, K., Influence of the Substrate Material on the Optical Properties of Tungsten Diselenide Monolayers. arXiv preprint arXiv:1610.00062 2016.
33. Azizi, A.; Zou, X.; Ercius, P.; Zhang, Z.; Elías, A. L.; Perea-López, N.; Stone, G.; Terrones, M.; Yakobson, B. I.; Alem, N., Dislocation motion and grain boundary migration in two-dimensional tungsten disulphide. *Nature communications* 2014, 5.
34. Desai, S. B.; Seol, G.; Kang, J. S.; Fang, H.; Battaglia, C.; Kapadia, R.; Ager, J. W.; Guo, J.; Javey, A., Strain-induced indirect to direct bandgap transition in multilayer WSe₂. *Nano letters* 2014, 14 (8), 4592-4597.
35. McCreary, A.; Ghosh, R.; Amani, M.; Wang, J.; Duerloo, K.-A. N.; Sharma, A.; Jarvis, K.; Reed, E. J.; Dongare, A. M.; Banerjee, S. K., Effects of Uniaxial and Biaxial Strain on Few-Layered Terrace Structures of MoS₂ Grown by Vapor Transport. *ACS nano* 2016, 10 (3), 3186-3197.
36. Kumar, S.; Kaczmarczyk, A.; Gerardot, B. D., Strain-induced spatial and spectral isolation of quantum emitters in Mono-and Bilayer WSe₂. *Nano letters* 2015, 15 (11), 7567-7573.
37. Voiry, D.; Yamaguchi, H.; Li, J.; Silva, R.; Alves, D. C.; Fujita, T.; Chen, M.; Asefa, T.; Shenoy, V. B.; Eda, G., Enhanced catalytic activity in strained chemically exfoliated WS₂ nanosheets for hydrogen evolution. *Nature materials* 2013, 12 (9), 850-855.
38. Ghorbani-Asl, M.; Enyashin, A. N.; Kuc, A.; Seifert, G.; Heine, T., Defect-induced conductivity anisotropy in MoS₂ monolayers. *Physical Review B* 2013, 88 (24), 245440.
39. Ye, G.; Gong, Y.; Lin, J.; Li, B.; He, Y.; Pantelides, S. T.; Zhou, W.; Vajtai, R.; Ajayan, P. M., Defects Engineered Monolayer MoS₂ for Improved Hydrogen Evolution Reaction. *Nano letters* 2016, 16 (2), 1097-1103.
40. Komsa, H.-P.; Krashennnikov, A. V., Native defects in bulk and monolayer MoS₂ from first principles. *Physical Review B* 2015, 91 (12), 125304.

41. Noh, J.-Y.; Kim, H.; Kim, Y.-S., Stability and electronic structures of native defects in single-layer MoS₂. *Physical Review B* 2014, 89 (20), 205417.
42. Li, H.; Yin, Z.; He, Q.; Li, H.; Huang, X.; Lu, G.; Fam, D. W. H.; Tok, A. I. Y.; Zhang, Q.; Zhang, H., Fabrication of single - and multilayer MoS₂ film - based field - effect transistors for sensing NO at room temperature. *small* 2012, 8 (1), 63-67.
43. Ataca, C.; Ciraci, S., Dissociation of H₂O at the vacancies of single-layer MoS₂. *Physical Review B* 2012, 85 (19), 195410.

Chapter 6

Conclusions

In this thesis, we have done a systematic study on the synthesis, transfer and TEM characterization of 2D TMDs, the detailed summary of the thesis are shown below:

(1) Using a combined experimental and numerical approach, we studied the key parameters for the planar and vertical growth of 2D materials and demonstrated the possibility for engineering their morphology by controlling the concentration and flow profiles. The results presented in chapter 3 revealed a new factor, concentration gradient, which can shift the growth of 2D TMDs from the planar to the vertical direction. It is further demonstrated that the density of as-grown nanostructures can also be controlled by the precursor flow rate during synthesis. This provides a new mechanism for controllable growth of 2D MoS₂ with different orientations and morphologies for applications in energy, catalysis, electronic devices and ultrathin integrated circuits.

(2) Epitaxial MoS₂/hBN vdW heterostructures are synthesized via PVT process with a well-defined and clean interface. S/TEM imaging and spectroscopy are used to study the atomic structure and chemical composition of the as-grown heterostructure, we also experimentally verify the crucial role of substrate defects (through reactive ion etching) on the nucleation and growth of MoS₂/hBN heterostructure. As the hBN substrate defect density increases, the epitaxy is lost and the MoS₂ domain size and thickness decreases.

(3) We have developed a universal and etching-free transfer technique which enables transfer of the TMDs films and flakes onto arbitrary substrates with high reliability. In addition, we have

determined the morphology and atomic structure of the film and its intrinsic defects including point defects, dislocations and grain boundaries in the MOCVD-grown WSe₂ film, using aberration-corrected S/TEM imaging. The orientation and stacking of as-grown WSe₂ film is explored and the presence of interlayer strain is also revealed via dark field imaging. We report the atom-by-atom visualization of various intrinsic defects including vacancies and anti-sites, possible grain boundary configurations (with 60° mirror boundaries as well as large and small angle GBs). A new type of heart-shaped defects is also observed along the reconstructed mirror boundary as a result of missing the metallic species. Corresponding DFT calculations and structural simulations are necessary to demonstrate the electronic structure of the specific defects in the MOCVD-grown WSe₂ film.

We believe such an investigation will be a guidance for future growth approaches aiming to obtain high quality TMDs film, which can greatly facilitate the exploration of condensed matter phenomena in 2D TMDs systems.